



McGill

The Role of Hemodynamics in Angiogenesis

by:

Siavash Ghaffari

A thesis submitted to McGill University in partial fulfillment of the requirements of the
degree of Doctor of Philosophy

Department of Chemical Engineering
McGill University
Montréal, Canada
June 2016

©Siavash Ghaffari, 2016

“Somewhere, something incredible is waiting to be known.”

— Carl Sagan

Abstract

The cardiovascular system is the first functional organ to form during embryonic development. Blood flow provides mechanical and chemical signals that are required for proper vascular development. The vasculature adapts to the onset of blood flow in part by forming new blood vessels through a process called angiogenesis. Angiogenesis is not limited to embryonic development, but also occurs after ischemic injuries, during wound healing as well as during tumour growth in cancers. A basic understanding of angiogenesis and the physiological cues that regulate the process is therefore an important therapeutic target for diseases such as stroke, myocardial infarction, and cancer. Angiogenesis also has application in regenerative medicine, and tissue engineering to provide nutrient transport to tissue. Blood flow provides biomechanical stimuli by exerting forces on the surrounding tissue including a tangential force on the luminal surface of the endothelium, called shear stress. Additionally, interstitial flow exiting or entering the vessel walls produces physical forces normal to the endothelium.

Angiogenesis is known to be controlled by a range of signals, but the role of blood flow and biomechanical signals are not well understood. One of the greatest difficulties in studying the interplay of flow dynamics and vascular remodelling is that few tools are available to analyse flow dynamics in real time *in vivo*. Therefore, the initial objective of this thesis was to develop a method to concurrently visualise vascular remodelling and blood flow dynamics. We used an avian embryonic model and injected an endothelial-specific dye, to image the vasculature, and fluorescent microspheres, to track fluid motion. Microsphere motion was analysed via an optical technique called micro-particle image velocimetry (μ PIV). μ PIV measurements are associated with large errors in complex geometry such as vessel branch points. As a result, we limited μ PIV measurements to straight segments and applied computational fluid dynamics (CFD) to obtain

the blood velocity in all other locations in the region of interest. The CFD analysis also allowed us to calculate other hemodynamic parameters such as the pressure, the vorticity and the shear stress.

We then used our technique to investigate the role that hemodynamic signalling plays in angiogenic sprouting. We found that flow dynamics mediates the location of sprout initiation, direction of sprout elongation, and the rate of sprout elongation during vascular development. Using the developed method and obtained parameters, we demonstrated that sprout location can be predicted based on flow dynamics. Moreover, the rate of sprout elongation is proportional to the pressure difference across the interstitium. Our results suggested that cues from the flow dynamics are important mediators of vascular homeostasis and morphogenesis.

In the last part of this work, we extended our technique to model interstitial flow passing through the porous matrix of the mesenchymal tissue. We modelled how VEGF transport within the tissue is altered by the presence of interstitial flow. This allowed us to simultaneously study the real-time interaction of luminal and transmural shear stress, interstitial flow, and VEGF distribution in angiogenesis. Interstitial flow strongly regulates the distribution of vascular endothelial growth factor (VEGF) within the tissue. We found that interstitial flow created regions of high VEGF in the location of sprouting, but did not alone indicate the exact sprouting location. We also showed that the sprout elongated against the direction of interstitial flow, and that a strong relationship was present between the elongation rate and the interstitial flow rate. Our results underscore the interplay between hemodynamics and VEGF distribution that regulates the development of vascular network to meet its many functional demands.

Résumé

Le système cardiovasculaire est le premier organe fonctionnel qui se forme au cours du développement embryonnaire. Les flux sanguins sont importants pour ce processus, et fournissent non seulement des signaux chimiques mais aussi des signaux mécaniques qui sont nécessaire pour le développement normal des vaisseaux. Le système vasculaire s'adapte au début de l'écoulement sanguin, en partie, par la formation de nouveaux vaisseaux sanguins, un processus appelé l'angiogenèse. L'Angiogenèse n'ai pas limité au développement embryonnaire, mais survient également à la suite de lésions ischémiques, au cours de la guérison de blessure, ainsi que pendant la croissance de tumeur lors d'un cancer. Une compréhension fondamentale de l'angiogenèse et les indices physiologiques qui régulent ce processus est donc une cible thérapeutique importante. L'angiogenèse s'applique aussi à la médecine régénérative et à l'ingénierie tissulaire, puisque tous les tissus ont besoin des flux sanguins adéquates pour survivre. Le flux sanguin fournit des signaux biomécaniques en exerçant une force tangentielle sur la surface luminale de l'endothélium, nommé des contraintes de cisaillement. De plus, le flux sortant ou entrant dans l'interstitiel produit des flux dans les jonctions endothéliales et dans les tissus mésenchymateux qui peuvent influencer le développement vasculaire.

Les signaux chimiques qui contrôlent l'angiogenèse sont très bien étudié, mais les rôles du flux sanguin et des signaux biomécaniques n'est pas très bien compris. Une des plus grandes difficultés dans l'étude du rôle des flux sanguins lors du remodelage vasculaire est qu'il existe très peu d'outils pour analyser la dynamique des flux en temps réel et *in vivo*. Par conséquent, l'objectif initial de la recherche présentée dans cette thèse était de développer une méthode pour visualiser simultanément le remodelage vasculaire et la circulation sanguine d'une façon dynamique. Nous avons utilisé un modèle embryonnaire aviaire et avons injecté les embryons

avec un colorant spécifique pour l'endothélium et des microsphères fluorescentes qui nous permettent de suivre le flux. Le mouvement des microsphères a été enregistré avec une caméra à haute vitesse, ce qui nous a permis de quantifier la vitesse du flux sanguin à l'aide d'une technique appelée le micro-Particle Image Velocimetry (μ PIV). Les mesures produites par le μ PIV sont associées à de grandes erreurs dans des situations de géométrie complexe, tels que les points de branchement des vaisseaux sanguins. En conséquence, nous avons limité l'utilisation du μ PIV à des segments droits et nous avons appliqué la modélisation numérique de l'écoulement pour obtenir la vitesse du flux sanguin sur la totalité de la région d'intérêt. L'analyse numérique nous a également permis de calculer plusieurs paramètres hémodynamiques tels que la baisse en pression, la vorticit  et les contraintes de cisaillement.

Nous avons ensuite utilis  notre technique pour  tudier le r le de l'h modynamique dans le bourgeonnement angiog nique. Nous avons trouv  que les m caniques des fluides affectent l'emplacement du bourgeonnement, la direction de l'allongement et le taux d'allongement d'un bourgeon au cours du d veloppement vasculaire. Nous avons d montr  que l'emplacement du bourgeonnement lors de l'angiog nese peut  tre pr dite sur la base des m caniques des fluides pr sents. De plus, le taux d'allongement des bourgeonnements est proportionnel   la diff rence en pression   travers du tissu interstitiel. Nos r sultats sugg rent que les indices provenant des flux sanguins sont des m diateurs importants de l'hom ostasie vasculaire et de la morphog nese vasculaire.

Dans la derni re partie de ce travail, nous avons  largi notre technique pour inclure la mod lisation des  coulements interstitiels, en mod lant les tissus m senchymateux en tant que matrice poreuse. Nous avons aussi mod lis  le transport de facteurs de croissance vasculaire (i.e. le VEGF) dans le tissu en pr sence d'un d bit interstitiel. Cela nous a permis d' tudier

simultanément l'interaction des contraintes de cisaillement lumenales et transmurales, ainsi que le rôle des flux interstitiels et l'effet de ces flux sur la distribution du VEGF dans le tissu. Nous trouvons que l'écoulement interstitiel affecte fortement la distribution du VEGF dans les tissus. Nous avons constaté que l'écoulement interstitiel crée des régions de forte concentration de VEGF qui se retrouve à l'emplacement de bourgeonnement angiogénique. La localisation de bourgeonnement est associée à de fortes concentrations de VEGF mais les concentrations de VEGF ne peuvent pas uniquement prédire la localisation exacte du bourgeonnement. Nous avons également démontré que l'allongement du bourgeonnement se produisait toujours en contre-sens du flux interstitiel et qu'une relation forte était présente entre le taux d'allongement et le débit interstitiel. Nos résultats soulignent l'interaction entre l'hémodynamique et la distribution de VEGF dans le règlement du développement du réseau vasculaire.

Acknowledgements

The completion of this journey would not be possible without the support and encouragement of many individuals and organizations.

First and foremost, I would like to express my deepest appreciation to my supervisors, Prof. Elizabeth Jones and Prof. Richard Leask, for their invaluable guidance, supports, and encouragement, and editing the manuscripts. I was encouraged to pursue my own ideas but always had feedback and support when I needed it. I am grateful to Elizabeth for giving me the opportunity to join her lab, and experience an area of research which I love. Thanks also for showing me how to be a mature scientist, changing my academic life. She was always helpful to advance the projects and is one of most intelligent people I have ever met. I would like to thank Richard for many things that I learned from him along the way. When I hit a problem, I went to him, and his comments were always instructive. He is a very nice and understanding person.

I appreciate all the help and support from my lab colleagues. Nothing would be the same without this amazing group of people in my working environment. Also I should thank my family and friends.

I would also like to acknowledge all funding agencies that supported my research. This Ph.D. project was made possible with a McGill Engineering Doctorate Award (MEDA) from the McGill Faculty of Engineering, other funds from the Natural Sciences and Engineering Research Council of Canada (NSERC), Canadian Institute of Health Research (CIHR), and Sick Kids Foundation.

Table of Contents

Abstract.....	I
Résumé.....	III
Acknowledgements.....	VI
List of Figures.....	X
List of Tables.....	XI
Contribution of Authors.....	1
1 Introduction.....	3
2 Objectives.....	5
3 Literature Review.....	7
3.1 Vascular Development.....	7
3.2 Effect of Fluid Dynamics on Vascular Development.....	10
3.3 Oxygen Transport in Blood Vessels and Tissue.....	14
3.4 Angiogenic Factors.....	19
3.4.1 VEGF.....	19
3.4.2 TGF- β	22
3.5 Interstitial Flow.....	23
3.6 Particle Image Velocimetry (PIV).....	26
3.7 Computational Fluid Dynamics of Embryonic Blood Flow.....	29
4 Simultaneous Imaging of Blood Flow Dynamics and Vascular Remodelling During Development.....	33
4.1 Preface.....	33
4.2 Abstract.....	35
4.3 Introduction.....	36
4.4 Results.....	38
4.4.1 Imaging Blood Flow and Vascular Development by Time-lapse Microscopy.....	38
4.4.2 Viscosity Estimates in Embryonic Vessels.....	41
4.4.3 Calculating Hemodynamic Parameters.....	44
4.4.4 Validation of Calculated Flow Rates.....	49
4.4.5 Studying the Interaction of Molecular and Biomechanical Stimuli.....	51

4.5	Discussion	54
4.6	Materials and Methods	57
4.6.1	Simultaneous Imaging of Vascular Remodelling and Blood Flow Dynamics	57
4.6.2	Creation of an Image Mask.....	60
4.6.3	Identification of Walls, Centreline and Local Vessel Radius	60
4.6.4	Micro-Particle Image Velocimetry Analysis	61
4.6.5	Blood Rheology	61
4.6.6	Computational Fluid Dynamics	62
4.7	Sources of Funding.....	63
4.8	Acknowledgements	63
4.9	Supplementary Information.....	63
5	Flow Dynamics Control The Location of Sprouting and Direct Elongation During Developmental Angiogenesis	67
5.1	Preface.....	67
5.2	Abstract	69
5.3	Introduction	70
5.4	Results	71
5.4.1	Sprout Location Can Be Predicted Based on Flow Dynamics	71
5.4.2	Sprout Elongation Rate is Proportional to the Pressure Difference Between the Two Vessels.....	82
5.5	Discussion	86
5.6	Materials and Methods.....	89
5.6.1	Simultaneous Imaging of Vascular Remodelling and Blood Flow Dynamics	89
5.6.2	Image Processing and Micro-Particle Image Velocimetry Analysis	89
5.6.3	Computational Fluid Dynamics	90
5.6.4	Statistical Analysis.....	91
5.7	Sources of Funding.....	91
5.8	Supplementary Information.....	92
6	Hemodynamics Modulate Angiogenesis in Part by Inducing Interstitial Flow that Redistributes Growth Factors	95
6.1	Preface.....	95
6.2	Abstract	97

6.3	Introduction	98
6.4	Results	100
6.5	Discussion	118
6.6	Materials and Methods	121
6.6.1	Flow Field in Free and Porous Media.....	121
6.6.2	Calculation of Permeability and Tortuosity in the Mesenchyme.....	122
6.6.3	Calculation of Permeability of Endothelial Cell Layer.....	124
6.6.4	Validation of Laminar Flow Assumption in Junctions and Transmural Shear Stress.....	125
6.6.5	Oxygen Transport in Blood Vessels and Tissue	126
6.6.6	VEGF Transport in the Tissue	127
6.7	Supplementary information.....	133
7	Original Contributions to Knowledge	140
8	Conclusion and Future Work.....	142
8.1	Conclusion.....	142
8.2	Future Directions.....	145
8.2.1	Predicting When Sprouting Forms.....	145
8.2.2	Extending the Applicability of the Method	145
8.2.3	Shear-Induced Activation of MMPs	146
8.2.4	Perturbation from Normal Vascular Development.....	147

List of Figures

<i>Figure 3.1- Development of the vasculature in mouse embryos..</i>	8
<i>Figure 3.2- Timeline schematic of arterial-venous differentiation in the yolk sac</i>	12
<i>Figure 3.3- Anatomy of the primary circulation in the avian embryo.</i>	15
<i>Figure 3.4- Schematic of growing sprout showing both tip and stalk cells</i>	20
<i>Figure 3.5- Interstitial flow is the extremely slow movement of fluid exiting the blood vessel walls through the cell junctions of endothelial monolayer and the porous matrix of tissue</i>	24
<i>Figure 3.6- In μPIV tracer particles are injected in the fluid and imaged via high speed camera</i>	28
<i>Figure 4.1- Analysis of changes in cardiac cycle during the time-lapse experiment.....</i>	41
<i>Figure 4.2- Analysis of changes in hematocrit at different stages of development.....</i>	44
<i>Figure 4.3- Combination of time-lapse images and flow measurements using computational fluid dynamics</i>	46
<i>Figure 4.4- Fluid dynamic analysis over a six-hour time-lapse period.</i>	48
<i>Figure 4.5- Analysis of measurement error during time-lapse experiments.....</i>	50
<i>Figure 4.6- Vessels enlarge and regress proportional to the logarithm of the shear stress.....</i>	53
<i>Figure 4.7- Summary of embryo culture technique.....</i>	59
<i>Figure 5.1- Fluid dynamic analysis over a ten-hour time-lapse period.....</i>	73
<i>Figure 5.2- Sprouts form from vessels at lower pressure towards vessels at higher pressure</i>	75
<i>Figure 5.3- Sprouts form in a local minimum of shear stress.....</i>	77
<i>Figure 5.4- Sprouting never occurred at locations where two blood flow streams merge</i>	79
<i>Figure 5.5- Application of these three hemodynamic parameters can predict sprouting location in perfused networks..</i>	81

<i>Figure 5.6- The rate of elongation is proportional to the magnitude of the pressure differential</i>	.83
<i>Figure 5.7- Sprouts will change direction to follow a positive pressure differential</i>	85
<i>Figure 6.1- Description of data acquisition and computer modelling</i>	102
<i>Figure 6.2- Time-lapse analysis of fluid dynamic parameters in the presence of interstitial flow</i>	104
<i>Figure 6.3- The presence of interstitial flow significantly affects the VEGF distribution</i>	107
<i>Figure 6.4- In the presence of interstitial flow, all isoforms of VEGF redistribute with the same pattern</i>	109
<i>Figure 6.5- Sprouts form at the shear stress minimum with the highest VEGF concentration</i>	111
<i>Figure 6.6- Sprouts form in regions with positive transmural shear stress, but not necessarily at maximums or minimums</i>	113
<i>Figure 6.7- Elongation rates do not correlate with VEGF concentration or gradient, but rather flow dynamics along the sprout</i>	116
<i>Figure 6.8- The direction of elongation follows the direction of flow after the VEGF maximum has been passed</i>	117

List of Tables

<i>Table 6.1- All Model Parameter values</i>	131
--	-----

Contribution of Authors

In accordance with the “*Guidelines for Thesis Preparation*”, this thesis is presented in a manuscript-based format, which contains three manuscripts. Introduction, objective and literature review sections precedes the manuscripts which cover chapters 4-6. In the final chapters, conclusions, future works and original contribution to knowledge are presented.

In all cases, I have researched and prepared the entire article in consultation with my supervisors. Moreover, all necessary experimental and modelling work, and analysis of the data was accomplished by me. My Ph.D. supervisors, Prof. Elizabeth Jones and Richard L. Leask supervised and helped in guiding the research, proofreading and editing the manuscripts. I was the first author of all publications, and other than my supervisors no one else contributed to the manuscripts. The roles each authors had in the preparation of three presented manuscripts are described below:

Manuscript 1 (chapter 4) - Siavash Ghaffari, Richard L. Leask, and Elizabeth AV Jones. "Simultaneous imaging of blood flow dynamics and vascular remodelling during development." *Development* 142.23 (2015): 4158-4167.

Author contributions:

Siavash Ghaffari - designed experiments, performed experiments, developed the computational algorithms, executed the computational modelling, analysed the results and wrote the manuscript.

Richard L. Leask - developed the computational algorithms, analysed results and edited the manuscript.

Elizabeth AV Jones - designed *in vivo* experiments, performed experiments, analysed the results and edited the manuscript.

Manuscript 2 (chapter 5) - Siavash Ghaffari, Richard L. Leask, and Elizabeth AV Jones. "Flow dynamics control the location of sprouting and direct elongation during developmental angiogenesis." *Development* 142.23 (2015): 4151-4157.

Author contributions:

Siavash Ghaffari - designed experiments, performed experiments, developed the computational algorithms, executed the computational modelling, analysed the results and wrote the manuscript.

Richard L. Leask - developed methodology, analysed data and edited the paper.

Elizabeth AV Jones - developed methodology, performed experiments, analysed data and edited the paper.

Manuscript 3 (chapter 6) - Siavash Ghaffari, Richard L. Leask, and Elizabeth AV Jones. "Hemodynamics Modulate Angiogenesis in Part by Inducing Interstitial Flow that Redistributes Growth Factors." To be submitted to *eLife* in June 2016.

Author contributions:

Siavash Ghaffari - designed experiments, performed experiments, developed the computational algorithms, executed the computational modelling, analysed the results and wrote the manuscript.

Richard L. Leask - developed methodology, analysed data and edited the paper.

Elizabeth AV Jones - developed methodology, performed experiments, analysed data and edited the paper.

1 Introduction

Heart disease, cancer and stroke are the leading causes of death in North America. Together, they accounted for 52% of all deaths in the United States in 2013 (Murphy et al., 2016). The ability to control angiogenesis, which is the formation of new blood vessels, has therapeutic potential for all three of these diseases. Most forms of heart disease are associated with capillary rarefaction that may be a cause rather than a symptom of the disease (Paulus and Tschöpe, 2013). In cancer, anti-angiogenic therapies have been approved to inhibit new blood vessel growth. The aim is to starve the tumor and thereby to inhibit its growth. Uncontrolled angiogenesis also occurs in diseases such as Age-Related Macular Degeneration (AMD). AMD is an important cause of blindness in the elderly and is the result of unusual blood vessel development in the retina. Lastly, in situations such as wound healing, stroke or myocardial infarction, we seek to induce angiogenesis to restore blood flow and promote tissue survival. As such, pro-angiogenic therapies are also being developed.

In these pathologies, the structure and hemodynamics of these newly formed vessels is closer to the embryonic vasculature than to mature vessels (Jones, 2010). Therefore, the embryo represents an excellent system in which to study angiogenesis. The cardiovascular system is the first functional organ in the embryo. Consequently, the vascular network of the embryo has to be functional as it develops in order to adjust to the changing requirements of the developing tissues. Once the embryo reaches about 2mm in size, diffusion alone is not enough to provide the cells with needed oxygen and nutrients. Therefore, a functional vascular network is required and as a result, physiological feedbacks play an important role in normal vascular development. Defects in vascular development tend to be fatal for the embryo. The patterning of the early

vessels is regulated by chemical signals (genetic signals and oxygen signals) and flow dynamics signals (Jones, 2010; le Noble et al., 2004; Patterson, 2005).

Human and chicken cardiovascular systems develop similarly. Thus, chick embryos are regularly used as model systems for investigations into early human vascular development. The chicken embryo is an accessible system that can be easily handled to study different stages of vascular development. Several studies have used qualitative flow visualization in chick embryos (Hogers et al., 1997; le Noble et al., 2004). There is also a wealth of studies that apply quantitative flow visualization techniques in early embryonic flow, such as optical coherence tomography (OCT), particle image velocimetry (PIV), Doppler velocity measurement, and confocal laser scanning microscopy (CLSM) (Hove et al., 2003; Ji et al., 2003; Jones et al., 2004; Liu et al., 2012; Poelma et al., 2008; Vennemann et al., 2006; Wang et al., 2009).

In this work, we advance current technology by combining time-lapse microscopy, flow visualization, and computational fluid dynamics to study flow dynamics and angiogenesis in a dynamic manner. Furthermore, we developed a numerical model of VEGF production and convection to study how interstitial flow, driven by pressure gradients between vessels, can redistribute growth factors in the tissue. Together, these techniques allow us to study both the role of mechanical forces created by blood flow, as well as indirect effects of blood flow that occur due to interstitial flow.

2 Objectives

The process of angiogenesis requires the integration of many different factors and thus gives rise to several fundamental biological questions. What is the role of hemodynamics in angiogenesis? What controls the initiation of angiogenesis and the regulation of structures within the vascular network? Which cues are the most crucial in this developmental process?

The underlying hypothesis of this thesis is that signals from flow dynamics play a significant role in the process of angiogenesis. In the chapter 5 we tested the hypothesis that **initiation and elongation of new sprouts require the presence of specific hemodynamic conditions**. In the chapter 6 we examined the hypothesis that **angiogenesis occurs both directly through mechanical forces and indirectly, due to changes in the distribution of growth factors**. To investigate this hypothesis, we used avian embryos as a model to study angiogenesis. We applied μ -PIV technique to obtain real-time flow measurements in the complicated geometry of vasculature that are present in early stages of development and then apply computational fluid dynamics to obtain hemodynamic parameters. Therefore, the following objectives were identified:

Develop a technique to simultaneously image blood flow dynamics and vascular morphology, by applying a combination of time-lapse imaging, flow visualisation and computational fluid dynamics (CFD).

1. Acquire real-time hemodynamic parameters such as pressure drops, vorticity and luminal shear stress in the entire region of interest using the developed technique.
2. Investigate the role of flow dynamic signals in the initiation and elongation of sprout during angiogenesis.

3. Determine whether certain flow dynamics patterns are predictive of the location of vessel sprouting during angiogenesis.
4. Study the role of interstitial flow, and transmural shear stress in the process of angiogenesis from sprout initiation to lumenization.
5. Examine the effect of interstitial flow on the distribution of growth factors within a tissue, using VEGF as model protein.
6. Differentiate mechanical and chemical changes that occur in the presence of blood flow, and their roles in sprout initiation and elongation.

The ultimate aim of this study is to investigate simultaneously the interplay of luminal shear stress, transmural shear stress, interstitial flow, and VEGF distribution in sprout formation in vascular development.

3 Literature Review

3.1 Vascular Development

The vascular system forms through a combination of vasculogenesis, which is the formation of new blood vessels when there are no pre-existing ones, and vascular remodelling. Vascular remodelling includes two main processes: angiogenesis and arteriogenesis. Angiogenesis is the formation of new blood vessels arising from pre-existing ones, and arteriogenesis is the enlargement in the diameter of an existing vessel. Blood vessels consist of two main cell types. Endothelial cells form a single layer around the entire vessels, and mural cells surround this structure and regulate vessel diameter and as a result can affect blood flow rates (Penn, 2008). Mural cells are not present initially in the embryo, so the first blood vessels are simple tubes of endothelial cells.

Vasculogenesis is the process of the initial differentiation of endothelial cell into a blood vessel network, by a de novo assembly of endothelial precursor cells (called “angioblasts” in embryos and “endothelial progenitor cells” in adults). Vasculogenesis initially occurs at two sites in the embryo: 1) the blood islands of the yolk sac, an extra-embryonic membrane; and 2) the major vessels of the embryo proper (Fig. 3.1A) (Flamme et al., 1997). During this process, the endothelial cells of blood islands migrate outwardly forming tubes which connect with each other randomly. As a result, the blood vessels make an immature honeycomb shaped network called the capillary plexus (Fig. 3.1B). Finally, the plexus connects to the aortas and to the heart to form a complete loop for blood flow. Before the onset of blood flow, all vessels have approximately the same diameters. Once the immature heart starts to beat and push fluid through the early vascular network (about 21 days of human embryogenesis, 8 days in mouse embryo and

2 days in chick embryo), the vessels remodel such that the characteristics of arteries and veins emerge and the network becomes more hierarchical (Fig. 3.1C) (Jones, 2010). This second process is called vascular remodelling.

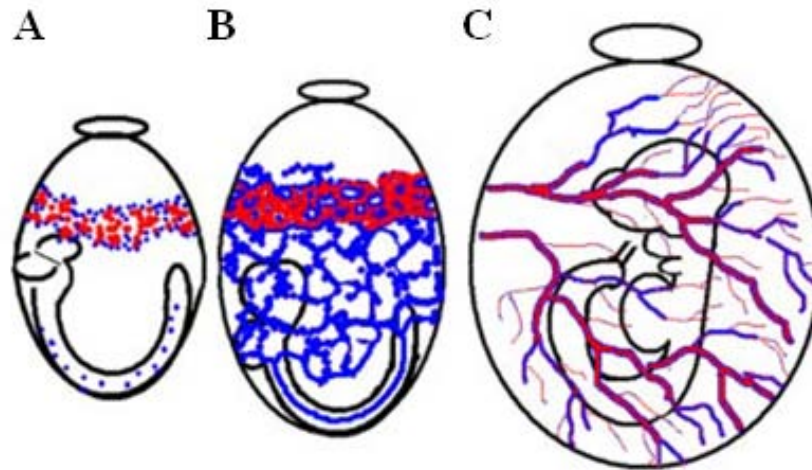


Figure 3.1- *Development of the vasculature in mouse embryos. (A) The endothelial cells of blood islands start to cover the entire yolk sac (B) The first vascular network of the embryo (capillary plexus) (C) With the blood flow, the vasculature is remodelled to form distinct arteries, capillaries and veins morphologically. Reproduced from (Jones, 2010) with permission.*

Blood flow is an essential cue for remodelling of the embryonic vasculature. When the heart begins to beat, blood flow creates mechanical cues such as wall shear stress and circumferential stress. These cues are essential for normal vascular development, and if the flow is stopped or becomes abnormal, vascular remodelling does not happen (Chapman, 1918).

Embryonic development can be staged by counting the number of somites. Somites are repetitive structures that form along the axis of the body. Therefore, number of the somites can

be used as a unit for developmental stage of the embryo. In the chick, the heart begins to beat at 12 somites. Red blood cells begin to circulate at 14 somites, and remodelling occurs between 14 and 25 somites.

Vasculogenesis occurs mostly in the embryonic period, but vascular remodelling occurs throughout one's entire life. For instance, in situation in which a blood vessel is blocked, new vessels develop to form a new vascular network in the vicinity of the blockage. Vessels also increase in diameter to increase perfusion to the tissue. In tumor growth, on the other hand, angiogenesis is active to create blood vessel that feed the growing tumor. As such, angiogenesis can have both constructive and destructive effects during pathologies.

Blood vessels are formed through vasculogenesis initially, but once the initial plexus is created, new vessels form by angiogenesis. Angiogenesis is a sophisticated process in which a new vessel sprouts from a monolayer of endothelial cells. These newly formed sprouting capillaries mature by recruiting mural cells. If they do not recruit these mural cells, the vessel is likely to fail and regress (Buschmann and Schaper, 1999).

Although it is likely that wall shear stress plays a significant role in angiogenesis, this role has been studied very little. Vascular density during remodelling was previously shown to decrease proportional to shear stress levels. Furthermore, increasing shear stress during remodelling was shown to cause a further decrease in vascular density (Chouinard-Pelletier et al., 2013). The authors found that in arteries, the vessels merge when the level of shear stress is low and that in veins, increasing shear stress resulted in a decrease in vascular sprouting.

Arteriogenesis is thought to be induced by both increased blood pressure and shear stress. Raising the pressure boosts the radial wall stress. Wall shear stress is also increased because of

increased blood flow for a given vessel diameter. The diameter of vessels enlarges rapidly in order to normalize the stresses (Prior et al., 2004). Arteriogenesis depends on many unknown parameters, so that the exact stimuli may be different in various situations. Therefore, increasing the flow alone may not induce this process. Smooth muscles contract to change the vessel diameter and thereby control the blood flow rate through a vessel. Moreover, arteriogenesis helps to deliver the blood flow, in situations such as blockage of vessels.

3.2 Effect of Fluid Dynamics on Vascular Development

Vascular development requires the onset of flowing blood, and as a result it strongly depends on hemodynamics (Djonov et al., 2000; Skalak, 2005). Blood flow induces physiological signals such as wall shear stress, circumferential wall stress (mechanical signals) and nutrients and oxygen requirements (chemical signals) which are crucial for normal vascular development (Jones, 2011a). Thoma was the first to show that in the vascular network of an embryo, vessels with greater amounts of blood flow increase in diameter whereas ones with less blood flow decrease (Thoma, 1893). Chapman surgically removed the heart of early chick embryos and found that vascular development is interrupted when blood flow in the vascular network is stopped, however other aspects of development occurred normally (Chapman, 1918). Wakimoto et al. observed the same fact using a genetic ablation in mice that prevented cardiac contraction. They also found that the lack of blood flow impeded vascular development (Wakimoto et al., 2000).

Since blood vessels are deformable, physical forces can modify the geometry of the vascular network during development. The physical forces caused by flowing blood include: 1)

wall shear stress which is the force per area component of tangential to the vessel wall and caused by fluid's velocity gradient and viscosity, and 2) cyclic stretch, caused by blood pressure which acts perpendicular to the vessel wall creating tissue stress. Since embryonic vessels lack elastin and do not distend (Ghaffari et al., 2015b; Risau and Lemmon, 1988), the effect of wall shear stress is thought to be more important than cyclic stretch in vascular development (Jones, 2011a). Endothelial cells can affect the level of wall shear stress by different methods, including changes in vessel diameter and/or changes in vessel branching (McCormick et al., 2001; Van der Heiden et al., 2006).

The work of Chapman and Thoma more than a century ago showed that blood flow was essential. However, it did not necessarily mean that shear stress and mechanical forces were required since blood flow also carries oxygen and nutrients. Using time-lapse confocal microscopy, Lucitti et al. investigated the role of fluid-derived signalling during embryonic development in the murine yolk sac (Lucitti et al., 2007). They prevented blood cells from entering circulation by immobilization the erythroblasts in the blood islands before the onset of circulation, and as a result lowered blood viscosity and shear stress. The results showed that erythroblast circulation was an important factor in inducing remodelling. In the next step, they showed that remodelling could be rescued in low-hematocrit embryos with the injection of additional of hetastarch solution that increased the viscosity of the blood. The authors suggested that the change in blood viscosity, and thereby shear stress, are the key factor to trigger vascular remodelling.

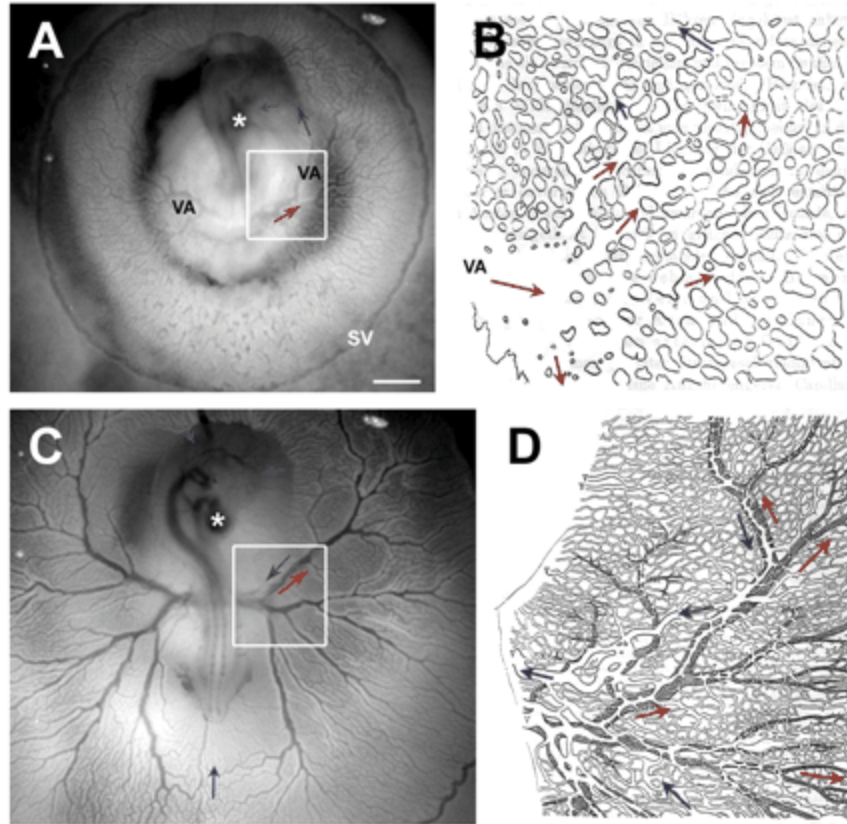


Figure 3.2- Timeline schematic of arterial-venous differentiation in the yolk sac. (A) Yolk sac just after perfusion starting. Directions of arterial and venous blood flow are shown by red and blue arrows respectively. (B) Schematic depiction of vascular system of the boxed area shown in A. (C) Embryo 26 hours later than in A. (D) Schematic depiction of the vascular system of the boxed area shown in C. Veins and arteries are shown in white and black respectively. Reproduced from (le Noble et al., 2004) with permission.

Shear stress not only induces vascular remodelling, but it is also necessary for proper arterial-venous differentiation of blood vessels (Fig. 3.2). Endothelial cells express genes that are specific either to arteries or veins and this arterial-venous differentiation is present even before the onset of blood flow. Though arterial-venous differentiation occurs before the onset of flow, it

remains plastic in the early embryo and can be altered by changing blood flow patterns. LeNoble et al. applied time-lapse video-microscopy to investigate the separation process of the arterial plexus from the venous plexus within the yolk sac of the chick embryo. They ligated vessels in arterial plexus, so that arterial flow would go through a vein. They found that this caused the artery to change into a vein, not just morphologically but also on a genetic level since the vessel downregulated arterial markers ephrinB2 and neuropilin 1. The authors presented that arterial-venous differentiation and patterning are predetermined, but display a high degree of endothelial cell plasticity that can be controlled by hemodynamics (Le Noble et al., 2004).

Shear stress levels are much lower in the embryo than in the adult, indicating that there may be differences in the way endothelial cells sense blood flow during development. Endothelial cells in the heart, called endocardial cells, have been shown to possess primary cilia, also called monocilia (Koefoed et al., 2014; Slough et al., 2008). Primary cilia are a single protrusion that is present in endothelial cells and these cilia have been shown to transduce shear stress (Nauli et al., 2008). Under high shear stress, primary cilia are disassembled (Iomini et al., 2004). Endothelial cells with primary cilia upregulate flow-induced genes, such as Klf2, at much lower levels of shear stress than non-ciliated endothelial cells (Schaper, 2009). During development, primary cilia have been shown to be present in low shear stress regions of the heart (Van der Heiden et al., 2006). The presence of primary cilia in embryonic blood vessels has never been verified. Mice that lack Pkd2, a gene essential for primary cilia function, have cardiac defects as well as edema, indicating possible vascular defects (Wu et al., 2000).

Shear stress does not only affect very early stages of vascular development, but has also been shown to be important for vascular development at later stages. Yashiro et al., found that flow mediated the development of the aortic arch. The aortic arch arises from 6 paired,

symmetric arteries. The arch forms by asymmetric regression of a subset of these arteries. To show the role of flow in this process, the authors ligated one of the vessels immediately before the onset of remodelling. This altered flow patterns without influencing the heartbeat. They cultured the ligated embryos *in vitro* for 36 h before examination of arterial morphology. They found the asymmetry of aortic arch is strongly dependent on blood flow pattern and that altering flow patterns could induce transposition of aortic arch (Yashiro et al., 2007).

Hemodynamic stimuli are needed not only for vascular and cardiac development, but also for proper hematopoietic development. A region of the embryo called the aorta-gonad-mesonephros, or AGM, produces hematopoietic stem cells that later colonize the liver (Cumano and Godin, 2007). Hematopoietic stem cell formation in the developing embryo relies on the induction of the heartbeat and the onset of circulation. Circulation, through nitric oxide stimulation, signals the endothelium of the AGM to produce definitive hematopoietic stem cells (North et al., 2009). Adamo et al. used mouse embryonic stem cells differentiated *in vitro*. They found that applying fluid shear stress to these cells increases the expression of the transcription factor Runx1, a gene important for hematopoietic differentiation. Their results demonstrated that shear stress increases haematopoietic colony-forming potential and the expression of haematopoietic markers in mice embryos. They highlighted the importance of biomechanical forces in hematopoietic development (Adamo et al., 2009).

3.3 Oxygen Transport in Blood Vessels and Tissue

Oxygen is crucial in cellular energetics, and supplying oxygen to the tissue is a crucial role of the circulatory system. Cells metabolism by oxidative phosphorylation relies strongly on

the consistent provision of oxygen to the cells. For avian embryos, gas exchange between developing avian embryos and the environment occurs directly through the shell and by gas diffusion. Oxygen diffuses through the shell, the inner and outer shell membranes, and through an albumen layer on the top of area of vasculosa, to finally reach to capillary plexus. During the first day of embryonic development, while the circulatory system is not functional yet, oxygen transport to the tissue occurs mostly by diffusion. The distance which oxygen can diffuse is low, and as a result presence of blood vessels network in the tissue area is crucial.

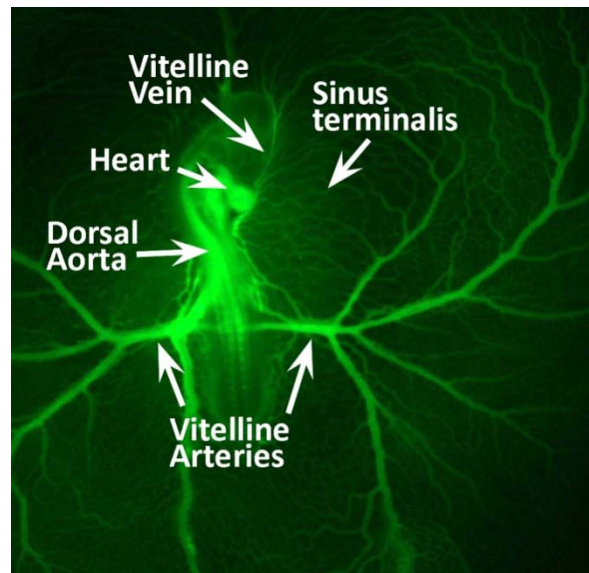


Figure 3.3- Anatomy of the primary circulation in the avian embryo.

Initiation of blood circulation in avian embryos occurs after 30 h of incubation (12 somites or HH11) (Jones, 2011b). It has been suggested that the heart starts to beat before convective oxygen transport by blood flow is needed, a concept referred to as prosynchronotrophy (Burggren, 2004). Within a few short hours after the heart begins to beat, strong blood flow is present, moving through the vascular network. This signals the start of

convective oxygen transport, although diffusion is still the main transport mechanism in the surrounding tissues (Burggren, 2004). In the initial type of blood circulation, called primary circulation, blood is pushed into the dorsal aorta and then to the vitelline arteries, gathers in the sinus terminalis and returns back to the vitelline veins and the heart (Fig. 3.3). As development continues, a closed circulatory system is established to facilitate the convective transport between the embryo and the yolk sac, and extra embryonic vessels and acts as the primary oxygen transport system (Meuer and Baumann, 1988). At this stage, all the extra embryonic vessels locate in the same plane, and sufficient blood vessels in the vascular area assure that it can be the principal respiratory organ of the very early embryo. At the 6th day of incubation, the chorioallantoic membrane is formed and allows exchange of gases between the environment and the developing embryo (Piiper et al., 1980). The chorioallantoic membrane performs a function for the egg similar to that of the placenta in mammals. Once the chorioallantoic oxygenation is functional, the chorioallantois becomes the main gas exchange organ.

During the early stages of development, before the chorioallantois has developed and is functional, the gas exchange system and the oxygen supply mechanism are not well understood. Available information for oxygen transport in the early embryonic development is insufficient due to measurement limitations. A needle oxygen microelectrode in the early embryo (24h to 6 days old) has been used to measure the oxygen partial pressure level (P_{O_2}) (Lomholt, 1984). They removed the eggshell and the outer shell membrane and inserted the electrode tip through the inner membrane and measured the oxygen level at different points. However, in their technique, the inner shell membrane limited visibility. As a result, they could not differentiate between measurements in the tissues and in the blood vessels. In a different set of experiments, Meuer and Baumann removed the eggshell and both inner and outer shell membrane to measure

the Oxygen partial pressure and pH values in vitelline and intraembryonic blood vessels of the early chick embryo using the recessed-tip oxygen microelectrodes (Meuer and Baumann, 1988).

To understand how hematic oxygen transport takes place in the early chick embryos, the amount of oxyhemoglobin has been determined in blood extracted from different locations of embryonic vessels using a spectrophotometrically method (Ciroto and Arangi, 1989). The level of oxyhemoglobin in the vitelline arterial and venous blood was measured and thus, the amount of oxygen transport by the hemoglobin was determined using the difference in levels of oxygenation between these two locations. In the chick embryo, red blood cells containing hemoglobin become visible after approximately 1 day of incubation in the blood islands (Bruns and Ingram, 1973). In very early embryonic development, just after the onset of circulation, only 20% of the total hemoglobin is oxygenated. By the end of the period of primary circulation, about 50% of the blood is oxygenated. However, the differences between the level of oxyhemoglobin in arteries and veins are very low. Therefore, up until the end of the primary circulation (third day of incubation), very little oxygen transport is actually carried by hemoglobin (Ciroto and Arangi, 1989). Nonetheless, blood facilitates transport of oxygen from the vascular area to tissue. The oxygen flux in capillaries has three terms: convective term of free oxygen dissolved in plasma, convective term of free oxygen inside erythrocytes, and oxygen bound to hemoglobin (Popel, 1988). Although the last term is very low in the period of interest, the first two terms are non-negligible. The dissolved oxygen terms are usually lower than the bound oxygen transport, however it can be significant if hematocrit is very low (Secomb et al., 2004). Furthermore, oxygen transport in hemoglobin and myoglobin solutions, and in suspensions of erythrocytes, is quicker than in water (Schmidt-Nielsen, 1997). Thus, even though

hemoglobin carries very little oxygen at this stage of development, whole blood still has an important contribution to oxygen transport in the embryo.

The experiments in this thesis have focused on embryos at the second day of incubation and, for the most part, analysis has been limited to the arterial plexus of yolk sac (i.e. vitelline arteries). Previous measurements, done with the eggshell and shell membranes removed, have found that the mean oxygen partial pressure (P_{O_2}) in the vitelline arteries for the 2 days old avian embryos is approximately 40 mmHg (Baumann and Meuer, 1992; Lomholt, 1984). As such, there is a significant difference between the ambient P_{O_2} (150 mmHg) and arterial P_{O_2} . This arises, in part, because the oxygen uptake is limited by diffusion resistance of the various layers of the area of vasculosa. A second reason for the low arterial P_{O_2} is that, in the embryo, oxygenated venous blood from the extraembryonic membranes is shunted with deoxygenated venous blood from embryo before entering the heart, causing a further drop in P_{O_2} (Baumann, 1992). The mean oxygen partial pressure (P_{O_2}) of the dorsal aorta and vitelline arteries are approximately equivalent. Therefore, oxygen tension at the vessel/tissue interface can be set at 40 mmHg and modelled by diffusion inside the tissue with vessels functioning as an oxygen source and tissue functioning as an oxygen sink.

The oxygen consumption rate in early chick embryos has been measured (Burggren et al., 2000). The authors compared embryos without cardiac output by ligation of the outflow tract with the embryos with an intact cardiovascular system, and observed negligible difference in the oxygen consumption rate. They speculated that vascular remodelling is the most important reason for the early development of a heart beat in chicken embryos. It should note that the removal of eggshell has negligible effect on the oxygen consumption (Høiby et al., 1983).

3.4 Angiogenic Factors

3.4.1 VEGF

Vascular endothelial growth factor (VEGF) is a protein synthesized by cells which is generally considered as the most important mediator of blood vessels formation during development. The VEGFs includes a family of structurally related proteins consist of five different members: VEGF-A, VEGF-B, VEGF-C, VEGF-D, and placental-derived growth factor. Each family member has its own function and is suitable for a specific situation, however, VEGF-A is the major mitogen in vascular development. VEGF-A is especially vital in the formation of angioblasts and the development of the early vasculature (Carmeliet et al., 1996). VEGF-A exists as five main isoforms, with different biological activities. In human, VEGF-A isoforms include VEGF₁₂₁, VEGF₁₄₅, VEGF₁₆₅, VEGF₁₈₉ and VEGF₂₀₆ (corresponding to the number of amino acids) and result from alternative RNA splicing. However, in mice, isoforms are one amino-acid residue shorter than the related human ones, and they are denoted VEGF₁₂₀ and so forth (Olsson et al., 2006). VEGF₁₂₁ and VEGF₁₆₅ are the most frequent and active isoforms (Ng et al., 2001). VEGF₁₂₁ is a 36-kDa acidic polypeptide lacking the residues encoded by exons 6 and 7, and therefore cannot bind to the heparans in the extracellular matrix (ECM) in rich concentration. VEGF₁₆₅ is a 45-kDa homodimeric glycoprotein, and contains the residues encoded by exons 7. Therefore, only VEGF₁₆₅ binds to the heparan sulfate proteoglycans (HSPG) present in the extracellular matrix (ECM) in rich concentration (Ferrara, 2004).

VEGF is required to regulate the functions of endothelial cells and controls several steps of angiogenesis, such as endothelial cell proliferation, survival, and migration (Gerhardt et al., 2003; Lamalice et al., 2007). Chemotaxis, which is migration of endothelial cells in response to

chemical stimuli, is largely driven by VEGF (Lamallice et al., 2007). During angiogenesis, the leading cell in the growing sprout is called a tip cell (Fig. 3.4). Tip cells respond to VEGF stimulation and extend filopodia. VEGF gradients direct these filopodia, prompting migration of the tip cell toward the VEGF source (Gerhardt et al., 2003; Ruhrberg et al., 2002). Filopodia are thin, filamentous membrane projections which are used for intercellular communication, cell migration, and cell adhesion in different of cell types (Wood and Martin, 2002). Endothelial cells use filopodia to sense the VEGF gradient, to probe the environment for guidance stimuli, to attach to the astrocytes, and to migrate (Gerhardt et al., 2003). Stalk cells, which are the trailing cells in a growth sprout, proliferate in response to the local concentration of VEGF (Gerhardt et al., 2003).

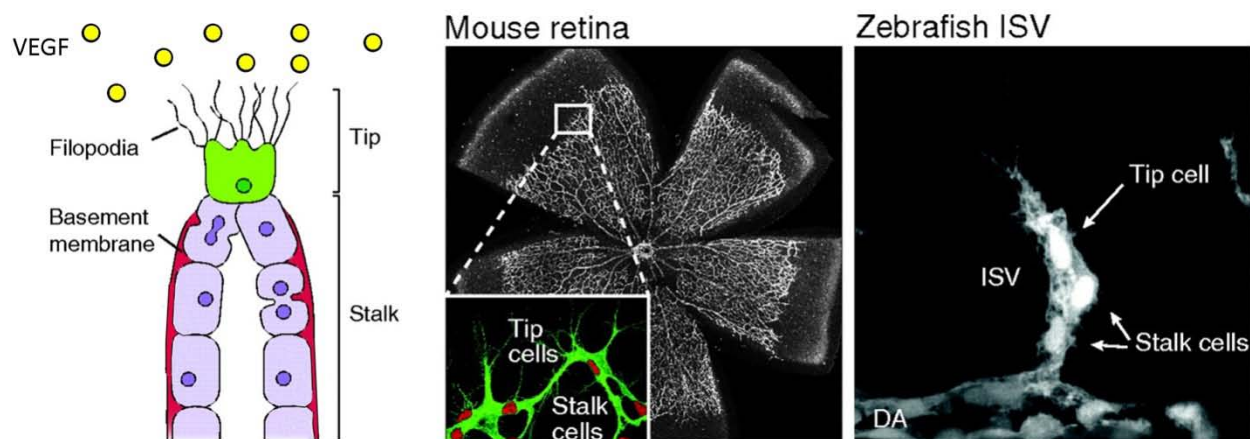


Figure 3.4 - Schematic of growing sprout showing both tip and stalk cells. In vivo images of the tip and stalk cell phenotype in the mouse retina model and the zebrafish intersomitic vessel (ISV) model. Modified from (Geudens and Gerhardt, 2011) with permission.

VEGF binds to homologous membrane tyrosine kinase receptors: VEGFR1, VEGFR2, and VEGFR3, which are expressed mostly by endothelial cells. Endothelial cells respond to

VEGF due to intracellular signalling started by the binding of VEGF family members to their cell surface receptor. Moreover, VEGFR1 and VEGFR2 after binding, exhaust VEGF from the interstitial space by internalizing the receptor-ligand complex (Olsson et al., 2006). VEGFRs are all of great importance in VEGF-induced angiogenesis, even if they have different biological activities (Fong et al., 1995). The signalling induced by VEGFR2 is the method by which VEGF regulates endothelial cell migration (Gerhardt et al., 2003).

VEGF is synthesized by several types of cells, including cancer cells, endothelial cells, vascular smooth muscle cells, and myocytes (Lamallice et al., 2007). Tissue growth produces regions of hypoxia, which is one of the strongest stimuli for angiogenesis and VEGF production. Hypoxia inducible factor (HIF-1 α), which is involved in oxygen sensing, controls VEGF expression in response to hypoxia. Therefore, hypoxia stimulates VEGF upregulation, as a result of change in the level HIF-1 α (Tang et al., 2004).

The VEGF distribution can be mediated by proteases such as the matrix metalloproteinases (MMPs), which can cleave VEGF from HSPG (Lee et al., 2005). Proteolytic release of VEGF can happen by cleavage of matrix-bound VEGF at its C-terminal domain or by cleavage of the ECM, resulting in free and diffusible VEGF (Bergers et al., 2000; Rodríguez-Manzaneque et al., 2001). VEGF cleavage can take place by means of the proteases plasmin, MMPs, and elastase (Lee et al., 2005). The nature of VEGF proteolysis, cell-mediated release, and the structural requirements for VEGF cleavage are still not well understood. Furthermore, the rate of VEGF cleavage *in vivo* is not known (Vempati et al., 2010). The higher molecular weight isoforms of VEGF such as VEGF₁₆₅, VEGF₁₈₉ can be cleaved by MMPs to release an unbound VEGF (Keyt et al., 1996). The secreted generic MMP is capable of proteolysis both free and ECM-bound VEGF₁₆₅ into VEGF₁₁₄ (Vempati et al., 2010).

3.4.2 TGF- β

Transforming growth factor (TGF)- β family members are multifunctional structurally related pleiotropic-secreted cytokines that includes three different isoforms (TGF- β 1, TGF- β 2, TGF- β 3) and other signalling proteins. Members of TGF- β family trigger their effects on cells, including endothelial and mural cells, through binding to a specific complex of type I and type II serine/threonine kinase receptors and intracellular Smad transcription factors (Goumans et al., 2009). Once the active TGF- β member is released from the ECM, it signals via TGF- β type II receptor (TGF- β R2) and TGF- β R1 (also known as ALK5; a type I receptor). Each particular family members have essential roles in multiple processes during development and in the preservation of tissue homeostasis in adult life (ten Dijke and Arthur, 2007). TGF- β 1 is the prototypic member of the TGF- β family that plays crucial role in many cellular functions, including the control of cell growth, cell proliferation and differentiation, apoptosis, and activation of many different cell types including immune cells. TGF- β regulates vascular development (Goumans et al., 2009; ten Dijke and Arthur, 2007).

As described in the section 3.1 vascular network developed through a combination of vasculogenesis and vascular remodelling. During embryogenesis, both processes are controlled strongly by cytokines and growth factors. TGF- β was suggested to control the activation state of endothelial cells by differentially activating two type I receptors, ALK5 and ALK1 (Goumans et al., 2002; Oh et al., 2000). These two different type I receptors have opposite effects in endothelial cells. Endothelial cells migration and proliferation is inhibited by Activation of ALK5 by TGF- β . However, cells migration and proliferation is increased by TGF- β -induced ALK1 activation. Therefore, the activation state of the endothelium depends on the balance of ALK1 versus ALK5 activation which is induced by TGF- β (Goumans et al., 2002). Besides,

studies have indicated that in the absence of key TGF- β receptors, angiogenesis stops in the yolk sac at an early stage of mice models resulting in deadly consequences (Goumans and Mummery, 2002). TGF- β 1 is the most likely of the three TGF- β isoforms to be involved in angiogenesis. Mice lack either TGF- β 2 and TGF- β 3 seem to have fairly normal angiogenesis (Akhurst et al., 1990; ten Dijke and Arthur, 2007). Other than angiogenesis, TGF- β may play roles in arteriogenesis. We injected embryos with TGF- β , and measured the average diameter of vessels of each embryonic stages. We compared the average diameter of vessels in normal development versus perturbed with injected TGF- β , and observed that TGF- β injection during vascular remodelling in the embryo resulted in an increase in vessel diameters. Therefore, we studied the effect of shear stress on vessel enlargement and the effect of perturbing this process with TGF- β signalling in chapter 4.

3.5 Interstitial Flow

The interstitium consists of mesenchymal cells that are embedded in ECM. Interstitial flow is the extremely slow movement of fluid exiting the wall of the blood vessel through a three-dimensional matrix of a tissue (Fig. 3.5). The role of interstitial flow is not only cell nourishment and convective transport of large proteins and other solutes, but also tissue maintenance and morphogenesis. The importance of interstitial flow in physiology has been known for a long time. Interstitial flow plays important roles in the morphogenesis, function, and pathogenesis of tissues. Moreover, interstitial flow induces blood and lymphatic capillary morphogenesis (Helm et al., 2007; Ng et al., 2004). Early embryonic differentiation and organ development can be patterned by small scale flows driven by cilia (Nonaka et al., 1998).

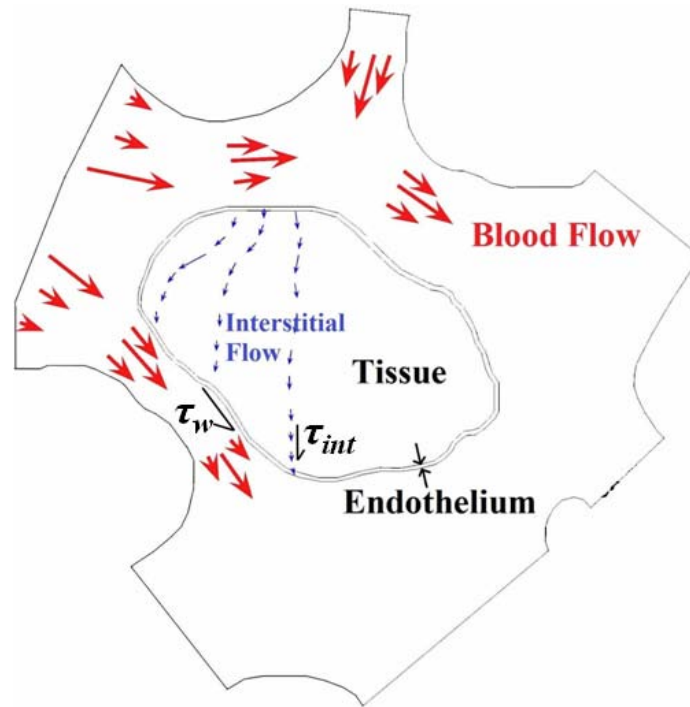


Figure 3.5- Interstitial flow is the extremely slow movement of fluid exiting the blood vessel walls through the cell junctions of endothelial monolayer and the porous matrix of tissue. τ_w is the luminal shear stress on the endothelial monolayer created by blood flow, and τ_{int} is the shear stress produced by interstitial flow.

Interstitial fluid motion plays significant roles in tissue morphogenesis and function, cell migration and differentiation and matrix remodelling, even though it flows very slowly. The mechanisms whereby interstitial flow stimulate cell response can be entirely mechanical; for instance the shear stress on the cell surface, the pressure force pushing on cells or the tethering forces between cells and the matrix (Rutkowski and Swartz, 2007). However, interstitial flow can also potentiate chemical signals. Using a blood vessels morphogenesis model, endothelial

cells scattered in a 3D matrix could be induced to form a network of tubes, if interstitial flow was present (Helm et al., 2005). In this study, small convective interstitial flow patterns created very small shear stresses on the cell surface. They showed small shear stress (≤ 0.01 Pa) levels were able to cause large changes in morphogen distribution, even in regimes in which convection did not dominate over diffusion. Interestingly, interstitial flow affects embryonic development and maintains tissue function in muscle, cartilage, and bone. Interstitial flow exiting or entering the vessel walls exerts physical forces across the endothelium (Tada and Tarbell, 2000). This physical force, called transmural shear stress, is one order of magnitude less than luminal shear stress. Interstitial flow transverse to the endothelial monolayer, in combination with vascular endothelial growth factor, has previously been shown to induce endothelial cell sprouting (Hernández Vera et al., 2008).

The mechanotransduction pathways involved in sensing slow interstitial flow have not been well established, however transmural flow has been shown to trigger a stimulus that result in increased strength of cell-cell junctions in the endothelial monolayer (Tarbell et al., 1999). It has been proposed that interstitial flow can direct mechanotransduction using the endothelial glycocalyx (Rutkowski and Swartz, 2007). The glycocalyx is a layer of glycosaminoglycans that cover the luminal surface of the endothelium. The glycocalyx plays a role in moderating or intensifying fluid stress signalling to the cell surface, rather than having the fluid shear stress act directly on the cell membrane (Tarbell and Pahakis, 2006). Other well-known mechanotransduction mechanisms such as stretch-activated ion channels, activation of adhesion complexes by tensile strain, and membrane shear, may also plays a role in flow sensing. Another possibility, however, is that the interstitial fluid flow induces change in the extracellular distribution of signaling proteins and consequently change the cell responses, because cells

receive directional signals from local concentration gradients of growth factors. The experimental difficulties in studying how transmural flows are sensed have limited progress, since shear stress and extracellular protein distributions are inherently coupled (Swartz and Fleury, 2007).

Two groups recently developed microfluidic devices to study the interaction of luminal shear stress, transmural shear stress and protein signals. Though the two devices differed, both consisted of endothelial cells seeded on collagen hydrogels that were exposed to flow, such that endothelial cells could sprout into the collagen gel in the presence of transmural and luminal shear stress (Galie et al., 2014; Song and Munn, 2011). Both groups found that interstitial flow enhanced angiogenesis, in the sprout initiation and the regulation of structures within a vasculature bed. One showed the number of filopodia produced during sprout are greater when sprout moves against the direction of interstitial flow than those moves with the flow, and the presence or absence of VEGF gradient did not change the number of filopodia (Song and Munn, 2011). Their results show that tip cells extend filopodia to probe the interstitial flow environment, in addition to responding to VEGF gradients. The application of filopodia to probe flow environment was previously corroborated (Gerhardt et al., 2003).

3.6 Particle Image Velocimetry (PIV)

Particle image velocimetry (PIV) is an excellent optical technique for flow visualization which has been developed to make quantitative measurement of the velocity of fluids. An advantage of this method over other methods to measure fluid dynamics, such as laser Doppler velocimetry and hot-wire anemometry, is that PIV generates results as two dimensional or three

dimensional velocity vectors. These other methods measure only the magnitude of velocity at a desirable point (Adrian and Westerweel, 2011). Micro-scale Particle Image Velocimetry (μ -PIV) was first developed to quantify flow in microfluidic devices (Santiago et al., 1998), but has since been extensively applied in the life sciences. It is a modified PIV system that is able to measure slow flows. The order of the velocities in slow flows is hundreds of micrometers per second making it low Reynolds flow (<1).

In μ PIV, tracer particles are injected in the fluid and then imaged using high speed camera. The velocity field can be measured by comparing consecutive pair images (Fig. 3.6). A pair of images is divided into smaller areas called interrogation windows. The interrogation windows in the first image are compared with the one in the consecutive image to seek the most similar windows. The mean velocity of the particles can be obtained by calculating the distance between the centers of these two interrogation windows divided by the time step between two frames. The most important components of a standard μ PIV setup are: a pulse flash light source (or laser), a digital high-speed camera, a microscope and associated optics, a synchronizer to coordinates the light pulse with the camera recording and the tracer particles. PIV software is also required for post-processing of the acquired images. The size of the particles is very important and can affect the results significantly (Lindken et al., 2009). The chosen particles must be significantly smaller than the length scale of the channel to assure that the flow field is not affected by the external particles, to avoid blockage of the channel, to reduce drag effects, and to prevent the unclear images. The particles must also be chosen large enough to scatter sufficient light for imaging, and also to minimize the effect of Brownian motion (Santiago et al., 1998).

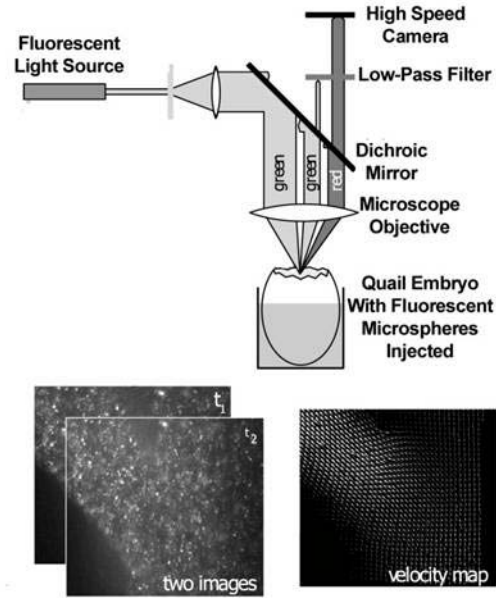


Figure 3.6- In μ PIV tracer particles are injected in the fluid and imaged via high speed camera. The velocity field can be obtained by comparison of consecutive pair images. Modified from (Vennemann et al., 2006) with permission.

Micro PIV has been used by many groups to analyse blood flow in microcirculation or embryonic vascular networks. Poelma et al. applied μ PIV to quantify the velocity field *in vivo* and calculate level of wall shear stress from the obtained velocity field of blood flow in the vitelline network of a chicken embryo (Poelma et al., 2008). Hove et al. modified the technique to use small groups of erythrocytes, and thereby followed flow through the heart of a zebrafish embryo, using the erythrocytes themselves as the tracer particles (Hove et al., 2003). Vennemann et al. applied μ PIV to quantify the blood-plasma velocity in the beating heart of a chicken embryo (Vennemann et al., 2006). Lee et al. employed a μ PIV technique to measure blood flow in extraembryonic venous and arterial blood vessels of chicken embryos. They used red blood

cells as tracers and captured flow images of red blood cells using a high-speed camera (Lee et al., 2007).

μ PIV technique has met some limitations in measurement. The original PIV technique was developed using a laser sheet to illuminate a two-dimensional cross section within a field of flow. Micro-PIV, on the other hand, uses volume illumination with post-processing to attempt to reject out of focus particles. Using flow channels with simple geometries where a theoretical solution was available to the blood flow profile, Pitts et al. investigated the efficacy of μ PIV (Pitts et al., 2012). They found that most common post-processing techniques for μ PIV resulted in shear rate measurements that had as much as a four-fold error. Furthermore, they showed that the velocity field obtained by μ PIV measurement on blood micro vessels near the walls are different from the theoretical solution by at least a factor of 2. Previous results from our research groups showed that the shear stress measurements at branch points using μ PIV are not accurate enough (Poelma et al., 2008). As such, the application of μ PIV should be limited to simpler geometries and to velocity measurements in the center of the vessels.

3.7 Computational Fluid Dynamics of Embryonic Blood Flow

Finite Element Methods (FEM) is the computational method used for our numerical simulation. The finite element method is an integral-based numerical technique that gives approximate solutions to partial differential equations (PDE). This method has many advantages to other computational methods such as the finite difference method and the finite volume method. It allows us to model more complex geometries and any arbitrary domains using unstructured meshing techniques, i.e. triangular meshes. This method discretizes the entire

domain into a number of sub domain called elements to solve the governing equations. The final solution is obtained by considering the relation of these elements to each other.

The governing equations to be solved using the finite element method are the continuity and momentum equations. The unsteady form of the momentum equations is applied to flow inside the vessels, due to the effects of blood flow pulsatility. The non-Newtonian behavior of embryonic avian blood using a microviscometer were demonstrated (Al-Roubaie et al., 2011). They published values for the rheological parameters of avian embryonic blood flow, and showed the apparent viscosity is different at different hematocrits, different shear rates, and at different stages during development. In the case of non-Newtonian fluid behavior and incompressible flow, the non-dimensional form of continuity and Navier-Stokes momentum equations are as follows:

$$\frac{\partial u^*}{\partial x^*} + \frac{\partial v^*}{\partial y^*} = 0 \quad (3.1)$$

x-momentum:

$$\frac{\partial u^*}{\partial t^*} + u^* \frac{\partial u^*}{\partial x^*} + v^* \frac{\partial u^*}{\partial y^*} = -\frac{\partial P^*}{\partial x^*} + \frac{1}{Re} \left(\frac{\partial \sigma^*_{xx}}{\partial x^*} + \frac{\partial \sigma^*_{xy}}{\partial y^*} \right) \quad (3.2)$$

y-momentum:

$$\frac{\partial v^*}{\partial t^*} + u^* \frac{\partial v^*}{\partial x^*} + v^* \frac{\partial v^*}{\partial y^*} = -\frac{\partial P^*}{\partial y^*} + \frac{1}{Re} \left(\frac{\partial \sigma^*_{xy}}{\partial x^*} + \frac{\partial \sigma^*_{yy}}{\partial y^*} \right) \quad (3.3)$$

The non-dimensional variables are defined as:

$$x^* = \frac{x}{D_0}, y^* = \frac{y}{D_0}, u^* = \frac{u}{U_0}, v^* = \frac{v}{U_0}, t^* = \frac{tU_0}{D_0}, \sigma^*_{xy} = \frac{\sigma_{xy}}{K \left(\frac{U_0}{D_0} \right)^n}, P^* = \frac{P}{\rho U_0^2}$$

where, D_0 and U_0 are vessel diameter and mean velocity at the inlet respectively. K and n are the rheology constants depending on the stage of development and the hematocrit. Reynolds number (Re) which appears in these relations has the following definition:

$$Re = \frac{\rho D_0^n}{K U_0^{n-2}} \quad (3.4)$$

In most published work, wall shear stress is measured in older developmental stages and in straight and large vessels. Because of the aforementioned limitations in performing flow quantification experiments in younger embryos, the embryonic vascular network can be modelled mathematically as an alternative method. This model can be solved numerically using various computational techniques. By using computational fluid dynamics (CFD), we have the opportunity to acquire more accurate estimates for the hemodynamics of the embryo at locations of complex geometries such as the branch points. However, verification of acquired results by this method is difficult. DeGroff et al. were the first to use numerically modelled flow in the human heart at early embryonic stages to obtain fluid dynamics parameters (DeGroff et al., 2003). Groenendijk et al. modelled flow in chicken embryo hearts in the early embryonic stages computationally using finite element analysis (Groenendijk et al., 2005). They simplified the 3-D geometries in order to derive wall shear stress even for higher velocities. Liu et al. did the same for embryonic chicken heart and considered the effect of the moving wall during a heartbeat (Liu et al., 2007). They later developed a method that combined imaging and finite element analysis to obtain the level of wall shear stress and *in vivo* blood flow dynamics in the cardiac outflow tract of early chicken embryos (Liu et al., 2011). Bharadwaj et al. developed a coupled method using a combination of imaging (Doppler ultrasound) and computational fluid dynamics to quantify hemodynamic parameters in the developing outflow tract, which eventually form the aortic and pulmonary valves (Bharadwaj et al., 2012). Wang et al. developed a 3-D finite

element based model which was combined with experimental techniques in order to quantify changes in geometry, blood flow and wall shear stress during normal aortic arch morphogenesis (Wang et al., 2009).

4 Simultaneous Imaging of Blood Flow Dynamics and Vascular Remodelling During Development

4.1 Preface

The following manuscript was published in 2015 in the journal *Development*, 142.23 (2015): 4158-4167. As described in the section 3.2 flow dynamics plays a significant role in vascular development. However, quantification of hemodynamics parameters in real-time *in vivo* has been difficult to measure. Therefore, developing a method for blood flow measurement is of great importance. The main goal of this paper was to create a technique which can be used in the further steps in investigation of the importance of flow dynamics in vascular remodelling. In this paper, a method to image and quantify simultaneously blood flow dynamics and vessel remodelling was presented. The approach provides a dynamic view of the whole vascular networks architecture concomitant with flow measurements at discrete time points and locations within the network. The methodology constitutes a combination of μ PIV analysis with mathematical modelling in order to estimate blood flow forces within the vascular network throughout its development.

We have included an application of the method that highlights the strength of the technique. We analysed the effect of shear stress on changes in vessels diameter. We then injected embryos with TGF- β , and showed that these embryos display increased vessel enlargement in response to shear stress even though the level of shear stress present is unchanged.

Simultaneous Imaging of Blood Flow Dynamics and Vascular Remodelling During Development

Siavash Ghaffari^{1,2}, Richard L. Leask², Elizabeth A.V. Jones^{1,2,3 *}

¹ *Lady Davis Institute for Medical Research, McGill University, 3755 Ch. Côte-Ste-Catherine, Montréal, QC, H3T 1E2, Canada.*

² *Department of Chemical Engineering, McGill University, 3610 University St., Montréal, QC, H3A 0C5, Canada*

³ *Department of Cardiovascular Science, KU Leuven, UZ Herestraat 49 - box 911, 3000 Leuven, Belgium*

To whom correspondences should be addressed: Elizabeth A.V. Jones, Centre for Molecular and Vascular Biology, KU Leuven, UZ Herestraat 49 - box 911, 3000 Leuven, Belgium, Tel. +32 16 34 75 58; Fax. +32 16 34 60 01; Email: liz.jones@med.kuleuven.be

Short Title: Time-lapse imaging of blood flow

4.2 Abstract

Normal vascular development requires blood flow. Time-lapse imaging techniques have revolutionized our understanding of developmental biology, but measuring changes in blood flow dynamics has met with limited success. Ultrasound Biomicroscopy and Optical Coherence Tomography can concurrently image vascular structure and blood flow velocity, but these techniques lack the resolution to accurately calculate fluid forces such as shear stress. This is important because hemodynamic forces are biologically active and induce changes in expression of genes important for vascular development. Regional variations in shear stress, rather than the overall level, control processes such as vessel enlargement and regression during vascular remodelling. We present a technique to concurrently visualize vascular remodelling and blood flow dynamics. We use an avian embryonic model and inject an endothelial-specific dye and fluorescent microspheres. The motion of the microspheres is captured with a high-speed camera and the velocity of the blood flow in and out of the region of interest is quantified by micro-particle image velocimetry (μ PIV). The vessel geometry and flow are used to numerically solve the flow physics with computational fluid dynamics (CFD). Using this technique, we can analyse changes in shear stress, pressure drops and blood flow velocities over a period of 10 to 16 hours. We apply this to study the relationship between shear stress and chronic changes in vessel diameter during embryonic development, both in normal development and after TGF- β stimulation. This technique allows us to study the interaction of biomolecular and biomechanical signals during vascular remodelling using an *in vivo* developmental model.

Keywords: Angiogenesis, Arteriogenesis, Hemodynamics, Time-lapse microscopy, micro-Particle image velocimetry, Computational fluid dynamics

4.3 Introduction

Vascular remodelling is an essential component of vascular development. The first vessels that form during development arise before the onset of blood flow and form a honeycomb shaped network called the capillary plexus. With the onset of flow, this early vascular network is remodelled into morphologically distinct arteries and veins. Blood flow is essential for vascular remodelling during development. If normal blood flow is not present, then remodelling does not occur (Chapman, 1918; Lucitti et al., 2007; Wakimoto et al., 2000). Remodelling involves angiogenesis, the formation of new vessels, and arteriogenesis, the enlargement of existing vessels. Blood flow creates mechanical forces on the endothelium, and endothelial cells are able to sense these forces and alter their gene expression (Abe and Berk, 2014; Bryan et al., 2014; Jones, 2011b). The dependence of remodelling on blood flow is well established yet there is a lack of understanding of the basic mechanisms by which remodelling occurs.

One of the greatest difficulties in understanding the interplay of flow dynamics and vascular development is that few tools exist to study flow dynamics in real time *in vivo*. During development, the geometry of the vascular network and flow rate change significantly. Clinical imaging and numerical simulations have been used to study the flow dynamics in developed vessels (Gijssen et al., 2007; Mantha et al., 2006; Robles et al., 2015; Steinman et al., 2003). These techniques are unsuitable to study microscopic processes during remodelling, which requires a resolution of at least 1 μm . As such, no method currently offers the ability to study both the movement of endothelial cells concurrently with an analysis of the evolving flow dynamics during remodelling.

Blood flow in the early embryo is characterized as Stokes flow. Stokes flow occurs when the viscous forces are much larger than the inertial forces (i.e., the forces due to the momentum of the fluid). Average embryonic blood velocity is relatively slow (often less than 1 mm/s, even during systole) providing little momentum and the viscous forces in blood therefore dominate the flow physics (Jones et al., 2004). Stokes flow allows the partial differential equations that describe fluid momentum to be linearized. As such, the embryonic vasculature is an ideal one in which to study the interaction of flow dynamics and the endothelium, as compared to the adult where flow separation, turbulence and other complex fluid phenomena are present.

Though the calculation of flow patterns within embryonic vessels is relatively simple, the geometry of the vascular network is complex and constantly changing during development. Many studies on shear stress have relied on the assumption that increased flow rates result in increased shear stress (Milkiewicz et al., 2001; Ziada et al., 1989). Though this is a valid assumption for straight, unbranched blood vessels, shear stress levels cannot be calculated purely based on the flow rate for more complex geometries (Manbachi et al., 2011). In these more complicated situations, calculation of shear stress levels requires solving a set of partial differential equations, called the Navier Stoke's equation, for each specific geometry.

In this work, we report a technique to simultaneously image blood flow dynamics and vascular development. We use a combination of time-lapse imaging, flow visualization and computational fluid dynamics (CFD). The flow visualization allows us to make localized measurements of the blood velocity at set time points and locations in the embryonic vasculature. The computational technique allows us to extend these measurements to acquire the blood velocity in the entire region of interest, as well as allowing us to calculate other hemodynamic

parameters such as the pressure drop, the vorticity and the shear stress. This allows us to follow the evolution of flow dynamics in real time as the vasculature remodels.

4.4 Results

4.4.1 Imaging Blood Flow and Vascular Development by Time-lapse Microscopy

Evaluation of blood flow dynamics during vascular development requires a method to track both the changes in vascular network morphology and the blood flow velocity repeatedly over an extended period of time. Avian embryos were the model of choice because of the relatively low photo-sensitivity and flat geometry of the avian capillary plexus during development. We previously established a technique to time-lapse vascular development in avian embryos (Al-Roubaie et al., 2012). We cultured the embryos ex ovo and labelled the endothelial cells by intra-vascular injection of fluorescently labelled acetylated low-density lipoprotein (AF488-AcLDL). A detailed description of the culture method is available in the Materials and Methods. We used micro-particle image velocimetry (μ PIV) to image the flow dynamics. This is done by intra-vascularly injecting fluorescent microspheres that act as tracers of the fluid motion and imaging the region of interest with a high-speed camera. To extract the velocity measurements from this data, the images of microsphere motion are divided into interrogation windows and the cluster of particles within each interrogation window is identified from frame-to-frame using a statistical cross correlation (for review, see (Adrian, 1991)).

We analysed embryos at the stage where blood flow initiates (Hamburger Hamilton HH11 or 30 hours of incubation), since this allowed us to study the process of vascular remodelling. We imaged the vascular network every 15 minutes using a high-resolution camera

(Zeiss Axiocam, green images). We followed the motion of the tracer particles using a high-speed camera that had high light sensitivity and could therefore capture fluorescence (FASTCAM Ultima APX-RS, red images). The motion of the tracer particles was imaged once every 2 hours for two entire cardiac cycles at 250 frames per second. The vasculature was imaged less frequently than the blood vessels to reduce phototoxic effects.

The original PIV technique was developing using laser-sheet illumination of the fluid motion to obtain a two-dimensional image of the tracer particle motion. Micro-PIV, however, is performed using a fluorescence microscope and results in the illumination of a three-dimensional space rather than a two-dimensional sheet. When blood flows within a vessel, the slowest motion is present next to the walls and the fastest motion is present in the centre of the vessel. Because of this, flow above and below the centreline is much slower than the flow in the centre of the vessel. Various post-processing techniques have been developed for μ PIV to minimize the error associated with imaging a three-dimensional volume. Out of focus objects are larger in size and lower in fluorescence. Thus, either selection based on particle size or thresholding based on fluorescent intensity can be used to reject out of focus particles (Meinhart et al., 2000). Using flow channels with simple geometries where a theoretical solution to the blood flow profile was possible, Pitts et al. investigated the efficacy of these post-processing techniques (Pitts et al., 2012). They found that most common post-processing techniques for μ PIV resulted in shear rate measurements that had as much as a four-fold error. We attempted to use μ PIV for the entire region of interest. We found that the technique could accurately measure velocities within straight vessel segments, but that, even with post-processing, shear rate measurements were inaccurate. For this reason, we limited our μ PIV measurements to assess the velocity in straight vessel segments and then used this as an input to our computational solver to obtain the flow

within the network. Micro-PIV can be performed using open source software (i.e. OpenPIV, PIVLab, JPIV) or by developing one's own code, as we did.

The selection of an appropriate tracer particle is of paramount importance in μ PIV. Particles must be neutrally buoyant, must not disturb the flow, and must be large enough to be unaffected by Brownian motion (Santiago et al., 1998). We investigated the use of several different types of fluorescent particles (polystyrene microspheres, liposomes, etc.). Though all the particle types tested met the criteria for μ PIV, they all suffered from one important limitation: in all cases, the particles adhered to the luminal side of the vessel wall within 2-3 hours of injection. Polyethylene glycol (PEG) is often used to make “stealth” micro-particles in biological application (Immordino et al., 2006). PEG is highly hydrophobic and creates a shell of water around PEGylated surfaces. To covalently link PEG to the microsphere surface, we used carboxy-modified polystyrene microspheres and amino 5K PEG. We followed the manufacturer's protocol for covalent coupling of proteins to the carboxy-modified polystyrene microsphere. After PEGylation, we found that the microspheres circulated for approximately 16 hours. Particles did gradually adhere to the vessel wall, but a large number of particles were still circulating at the end of the time-lapse.

Because blood velocity measurements were less frequent than images of the vascular network, we needed a method to interpolate between velocity measurement time points. Flow was imaged for two cardiac cycles at each time point, and the velocity of the blood flow during the cardiac cycle was extracted (Fig. 4.1A). To obtain flow information between flow measurement time-points, an interpolation was made based on the trend of the velocity data at different points in the cardiac cycle for the entire time-lapse experiment (Fig. 4.1B). Only five points in the cardiac cycle are displayed in Figure 4.1B for the sake of simplicity, however,

additional points in the cardiac cycle were analysed depending on the specific experimental needs.

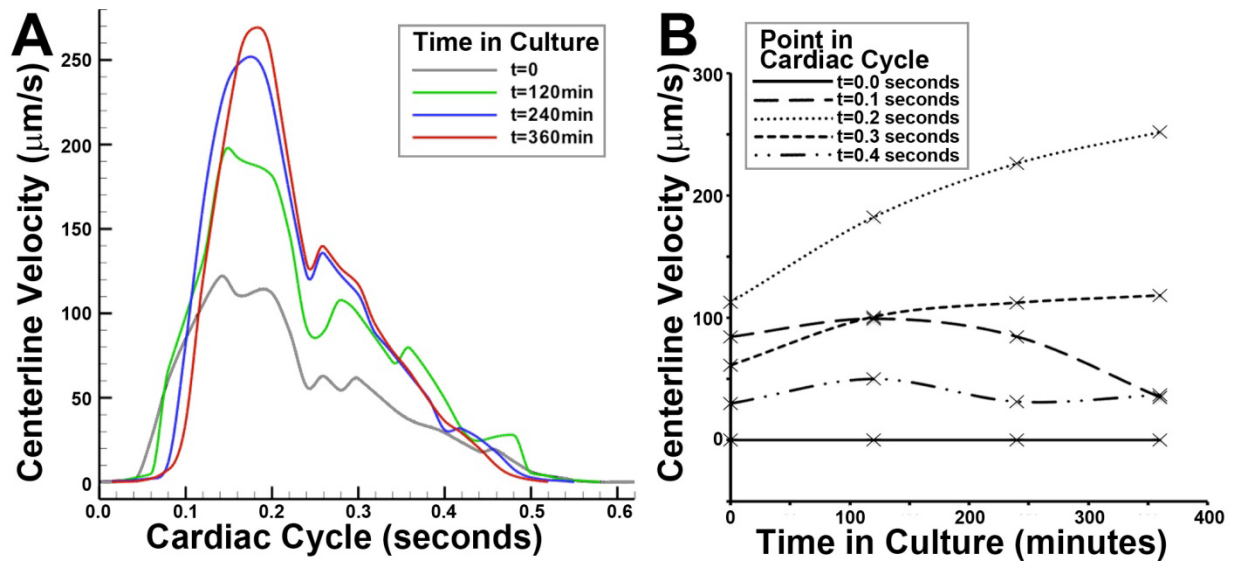


Figure 4.1 – Analysis of changes in cardiac cycle during the time-lapse experiment. The blood flow velocity in the centre of the vessel was analysed for all inlet and outlet vessels to the region of interest using μPIV . A typical cardiac cycle for one vessel segment is shown taken at 4 time points within the time-lapse experiment (A). Since the velocity was measured less frequently than the vascular morphology, it was necessary to interpolate between the velocity measurement time points. Interpolation was performed cross-plotting the data from the cardiac cycle and fitting a line to the velocity over the entire time-lapse at multiple points in the cardiac cycle (B).

4.4.2 Viscosity Estimates in Embryonic Vessels

Calculation of hemodynamic properties, such as the shear stress, requires an estimate of the viscosity of the fluid. Blood viscosity changes with hematocrit and with shear rate (i.e., the

velocity gradient of the blood). Red blood cells form in the blood islands and enter circulation gradually with the onset of blood flow (Lucitti et al., 2007). Thus, the hematocrit is not constant during early vascular development. To measure changes in hematocrit with respect to embryonic stage, we injected embryos with fluorescent dextran and then isolated the whole embryo and placed it in culture on a heated confocal microscope. We used the line-scanning function of the confocal microscope to scan across one vessel repeatedly such that we obtained an X versus time image (Fig. 4.2A). In these images, the blood plasma is fluorescent from the dextran injection and the red blood cells appear as black streaks within the vessel. By evaluating the percentage of black pixels within the vessels, we could estimate the hematocrit of the blood.

In vessels smaller than 300 μm , the hematocrit is dependent on the vessel diameter due to a phenomenon called the Fahraeus effect (Fahraeus, 1929). We therefore measured the hematocrit with respect to diameter at different stages (Fig. 4.2B). We found that the data fit to a previously published equation for the Fahraeus effect in smaller vessels (Pries et al., 1990), such that:

$$\frac{H_T}{H_D} = H_D + (1 - H_D). (1 + 1.7e^{-0.35D} - 0.6e^{-0.01D}) \quad (4.1)$$

Where H_T is the tube hematocrit (i.e., the effective hematocrit in a small vessel), H_D is the discharge hematocrit (i.e., the constant hematocrit present in larger vessels and in the heart) and D is the diameter. As such, we used the hematocrit and the diameter from each measurement to calculate a discharge hematocrit for each stage. We then plotted the average discharge hematocrit with respect to somite stage (Fig. 4.2C). The data was fit to a cubic equation as a means to easily calculate the hematocrit in our computational analysis.

We previously published values for the viscosity of avian blood at different shear rates and hematocrits for embryos between 4 days and 6 days of incubation, or HH22 to HH34 (Al-Roubaie et al., 2011). Embryos used in this current work were much younger, starting at 30 hours of incubation (13 somites or HH11). Ideally, we would have extended our previous work to younger stages; however, we were unable to collect enough blood to make viscosity measurements from embryos younger than HH22. We were therefore obliged to work with the data available. Most work on embryonic blood flow assumes that embryonic blood has the same properties as adult blood (Jones, 2011a; Poelma et al., 2008). Thus, the use of data from embryonic blood, even from slightly older stages, represents an advance over previous estimates. Our previously published work indicated that the viscosity of embryonic blood fit a Carreau model, such that:

$$\mu = \mu_{\infty} + (\mu_0 - \mu_{\infty})[1 + (\lambda\gamma)^2]^{\frac{N-1}{2}} \quad (4.2)$$

Where the constants (μ_{∞} , μ_0 , λ and N) are dependent on the stage of development and the hematocrit. γ is the shear rate. For each time point, we used the stage of development to establish H_D (based on Fig. 4.2C). We then used Equation (4.1) to establish H_T for each vessel segment based on the average diameter of that segment. We evaluated the Carreau constants based on H_T and the stage of development by interpolating and extrapolating, respectively, from our previously published values for embryonic blood viscosity (Al-Roubaie et al., 2011). Because different vessel diameters are present within a region of interest, a different Carreau equation was applied to each vessel segment. This allows us to include shear rate-dependent effects on the viscosity in our computational analysis.

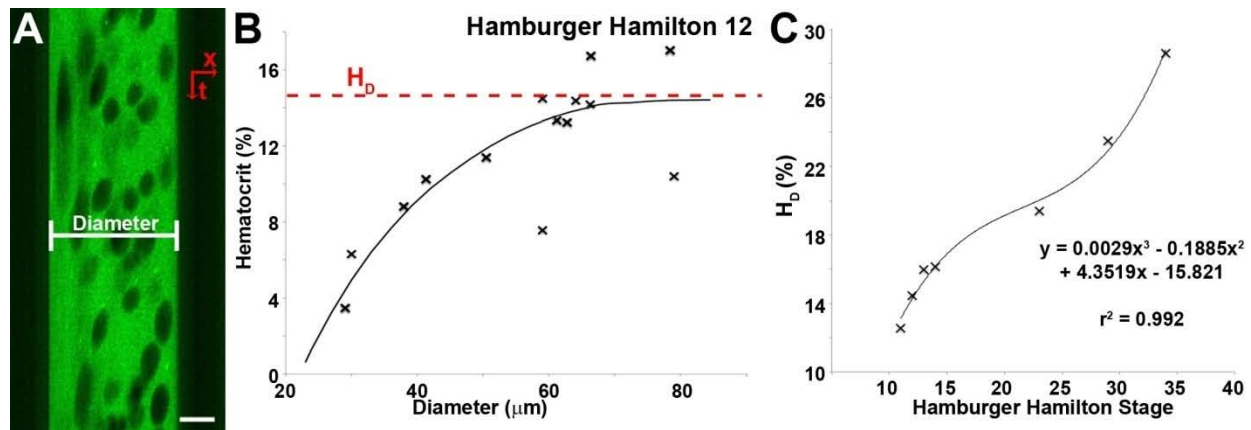


Figure 4.2– Analysis of changes in hematocrit at different stages of development. The hematocrit was analysed using a line scanning technique (A). Embryos were injected with fluorescent dextran, which labels the blood plasma, but is excluded from the red blood cells. The laser line was scanned at one location, perpendicular to the direction of blood flow, yielding an x versus time (t) image. The percentage of black pixels was used to estimate the hematocrit and the thickness of the green band to measure diameter. The hematocrit was plotted with respect to the vessel diameter (B), and agreed with the equation for the Fahraeus effect (black line). Hematocrit measurements were normalized using the vessel diameter to calculate the effective discharge hematocrit (H_D , red dotted line). The discharge hematocrit was measured at different stages ($n=3$ to 5 per stage, C). A cubic equation was fit to the data to allow it to be used in the computational analysis. Scale bars; $20 \mu\text{m}$

4.4.3 Calculating Hemodynamic Parameters

A stack of images comprising the image of the wall and the 500 high-speed images of the microsphere motion was flattened into a single image. The resultant image was filtered and thresholded to create a black and white image mask (Fig. 4.3, see Materials and Methods for additional details). A Canny algorithm was applied to the image mask using the Matlab edge function to identify the inner wall boundaries of perfused vessels. The Canny method can

produce equally thin edges with smooth continuous pixels even under noisy condition (Canny, 1986). The edge detection resulted in a matrix of black and white pixels that defined the location of the vessel walls. The mask was skeletonized to provide an image of only the centreline of the vessels. The distance between the centreline and the vessel wall was averaged for each segment, in order to define the vessel diameter for the viscosity estimates.

The vessel geometry, inlet and outlet flow rates to the region of interest and the viscosity estimates were then combined using a computational fluid dynamic (CFD) solver (Fig. 4.3). In the CFD solver (COMSOL Multiphysics), a 2D simulation was chosen. The solver was set to solve the flow for laminar, time-dependent, incompressible flow. Since the vessel network has curved geometries, the numerical algorithm was applied on a non-orthogonal curvilinear coordinate framework. The solver uses a finite element model to solve the Navier Stoke's equation. Mesh generation for the finite element model was done using the CFD solver and different mesh sizes were tested ("fine", "extra-fine" and "extremely fine"). The inlet and outlet boundary conditions were set using the measured flow rates for the cardiac cycle (Fig. 4.1). Inlet and outlet blood velocity measurements were made far from branch points, so fully developed flow was assumed at these points. Based on the Reynold's number of blood flow in embryonic vessels, the flow should become fully developed within a few microns of the branch points. For a network with N inlet and outlets, the velocities of $N-1$ segments were used as boundary conditions. For the last vessel segment, the pressure at the outlet was set to zero. Two convergence criteria were set in the solver: first, a mass flux residual of less than 10^{-8} for each control volume; second, $(|\varphi_{i+1} - \varphi_i|)/|\varphi_{i+1}| \leq 10^{-10}$ for all time steps where φ represents v_x or v_y (flow velocities in x and y directions), and i is the number of iterations. This procedure was repeated for each time point in the time-lapse experiment.

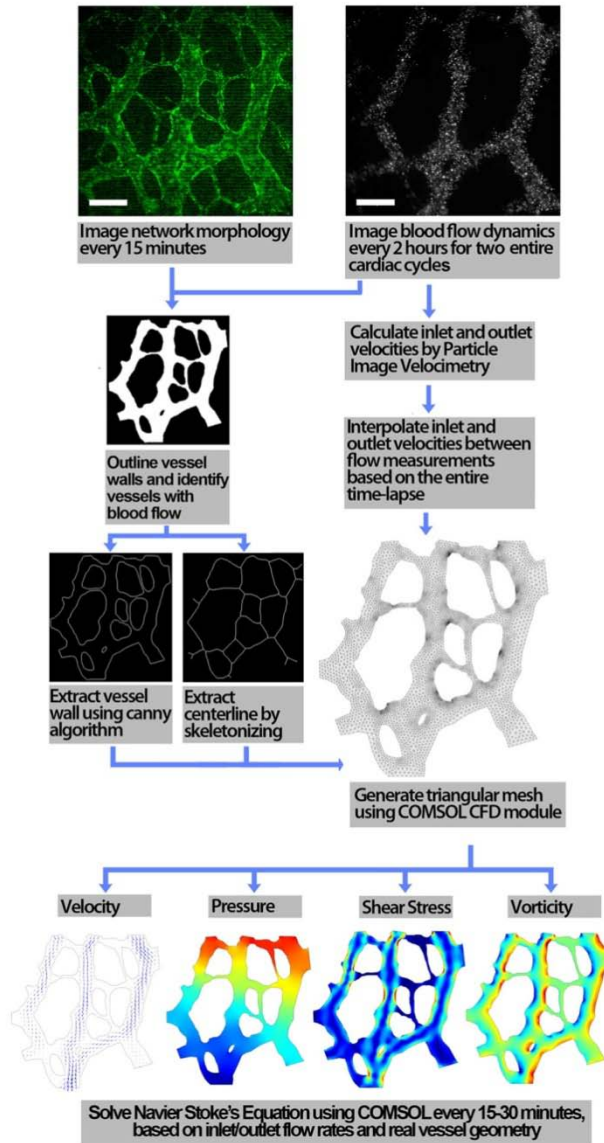


Figure 4.3– Combination of time-lapse images and flow measurements using computational fluid dynamics. Images of endothelial cells labelled with AlexaFluor488-acetylated low-density lipoprotein (AF488-AcLDL) were taken every 15 minutes for a period of 12-16 hours. Fluorescent circulating microspheres were imaged every 2 hours at 250 frames per second for 2 seconds. The set of 500 images of the microspheres and the image of the vessel wall were flattened and thresholded to produce an image mask. From the mask, the vessel outline and centreline were identified. Micro-particle image velocimetry (μ PIV) was used on the microsphere images to quantify the inlet and outlet velocities. A CFD solver was used to generate a triangular mesh for the finite element analysis and from this fluid dynamic parameters were calculated for the entire cardiac cycle at each time point. Scale bars: 200 μ m (top two images).

The CFD solver outputs the velocity, shear stress, relative pressure and vorticity of the flow. The left panel of the supplemental movies shows the endothelial cell behaviour (Fig. 4.4A, Supplemental Movies 1-3). The region outlined by the yellow box represents the region where flow was analysed. In this time-lapse, we observed both intussusceptive angiogenesis (cyan arrowhead, Supplemental Movie 1) and sprouting angiogenesis (yellow arrow, Supplemental Movie 1). Systolic velocities in the centre of the vessel were on the order of 500 $\mu\text{m}/\text{second}$ at the beginning of the time-lapse (13 somites) and increased to approximately 1500 $\mu\text{m}/\text{second}$ nine hours later, when embryos had reached 20 somites (Fig. 4.4B, Supplemental Movie 1). These velocities are similar to those observed in vessels of the same diameter in the mouse embryo (Jones et al., 2004). We were also able to capture the first flow through newly lumenized blood vessels after angiogenesis ($t=510$ minutes for Supplemental Movies 1). We calculated the relative pressure in the vessels (Fig. 4.4C, Supplemental Movie 2). The pressure drop was approximately 1 Pa at early time points, but increased to 6 Pa by the end of the experiment. Wall shear stress at the start of the time-lapse was on average 0.064 Pa ($n=3$ embryos, SEM = 0.015) but increased to an average of 0.18 Pa (SEM = 0.02) by the end of the time-lapses (Fig. 4.4D, Supplemental Movie 3). These shear stress measurements are of the same order of magnitude as previous shear stress estimates during early vascular development in mouse and avian embryos (Chouinard-Pelletier et al., 2013; Jones et al., 2004). Our computational model also allowed us to make the first estimates of vorticity in the remodelling embryonic vascular network (Fig. 4.4E, Supplemental Movie 3). Vorticity is a measure of the angular velocity of the fluid. Despite the name, vorticity does not necessarily indicate the presence of a vortex. When an obstruction in the path of the flow is present, the fluid moves around the obstruction creating an angular component

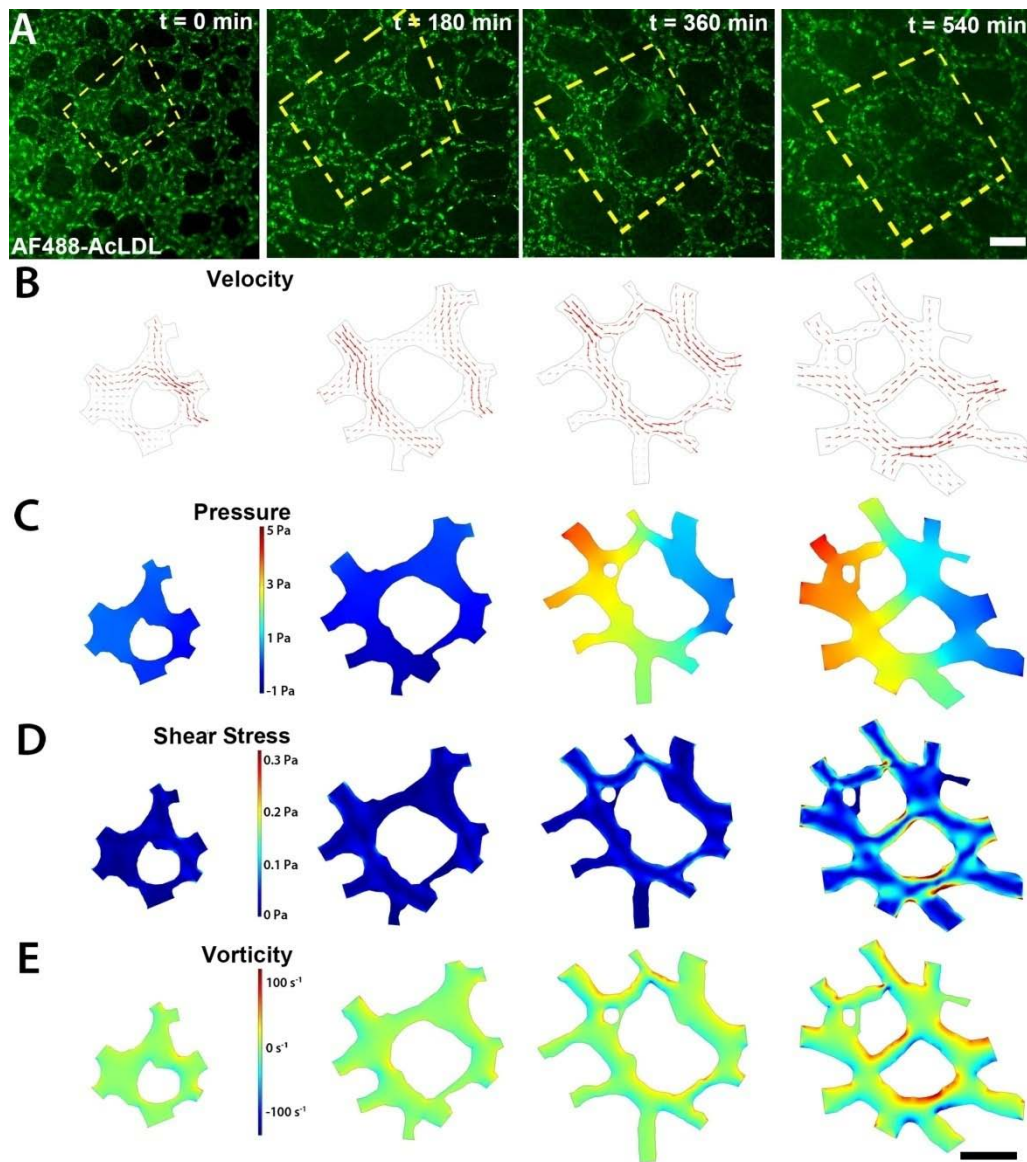


Figure 4.4– Fluid dynamic analysis over a six-hour time-lapse period. Full results from the time-lapse are available as Supplemental Movies 1, 2 and 3. The embryo was at 13 somites or Hamburger Hamilton Stage 11 at the start of the time-lapse experiment. The yellow box identifies the specific region that was analysed in this time-lapse (A). Flow was determined for the entire cardiac cycle, however only values for peak systole are presented. Blood flow velocities were analysed (B). The magnitude of the velocities is available in Supplemental Movie 1. By combining viscosity estimates with the velocity profiles in the vessels, the pressure (C), shear stress (D) and vorticity (E) were calculated. Scale bars: 100 μm .

to the velocity vector. As such, vorticity can be used to identify bifurcations in the flow, which are biologically active regions in the vessel wall.

4.4.4 Validation of Calculated Flow Rates

To validate our calculated hemodynamic profiles, we first investigated whether the method accurately predicted the pattern of blood flow at one single time point. We used images of flow from an older embryo (HH15), where we had observed flow reversal (Supplemental Movie 4). This movie was taken with microspheres that had not been PEGylated, and therefore some clumps of microspheres were present. The clumps resulted in differences in the size of the particles that also allowed us to follow streamlines within the flow to ensure our CFD analysis was accurate. In this movie, the blood flow velocities from the inlet and the outlet on the left hand side of the image were entered into the CFD solver, and the outlet on the right hand side was set to a pressure value of zero. We found that our computational analysis accurately predicted the flow patterns observed, including the flow reversal, even though the input flow rates (i.e., the two left hand blood vessels) only exhibited forward flow without any reversal in the direction of flow. Furthermore, the streamlines predicted by the CFD analysis agreed with the experimental results.

A

	Method	Embryo1		Embryo2		Embryo3	
		No. elements	Velocity ($\mu\text{m/s}$)	No. elements	Velocity ($\mu\text{m/s}$)	No. elements	Velocity ($\mu\text{m/s}$)
t = 0 minutes	$\mu\text{-PIV}$	-	29.12	-	427.87	-	237.45
	Fine mesh (% Error)	2106	28.04 (3.7)	3025	441.21 (3.1)	3381	227.45 (4.2)
	Extra fine mesh (% Error)	2550	28.08 (3.6)	4763	440.87 (3.0)	5558	227.87 (4.0)
	Extremely fine mesh (% Error)	4660	28.19 (3.2)	13186	440.49 (2.9)	17016	228.54 (3.8)
t = 360 minutes	$\mu\text{-PIV}$	-	325.13	-	2324.73	-	601.23
	Fine mesh (% Error)	3608	300.34 (7.6)	9702	2479.67 (6.2)	3563	555.34 (7.6)
	Extra fine mesh (% Error)	5477	301.21 (7.4)	17725	2477.97 (6.2)	6133	556.21 (7.5)
	Extremely fine mesh (% Error)	13339	303.73 (6.6)	43355	2473.12 (6)	14940	559.12 (7)

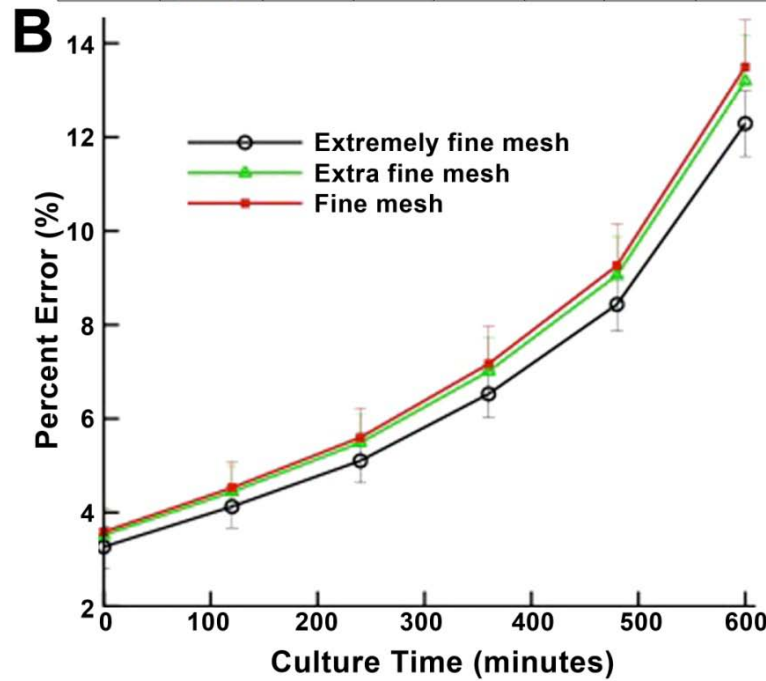


Figure 4.5- Analysis of measurement error during time-lapse experiments. For a region of interest with N vessels entering or leaving the region, the blood velocities in $N-1$ vessels were used in the computational analysis. For the last vessel, the outlet pressure was set to zero as a boundary condition. Error was calculated by comparing the calculated velocity for this last vessel with the measured value using μPIV . The precise values for the measured and calculated velocity for three example embryos at two time points are shown (A). The error associated with the mesh size in the finite element analysis was investigated by using different setting for the mesh size in the CFD solver (“fine”, “extra fine” and “extremely fine”). The percent error was very similar from one embryo to another, regardless of the magnitude of the velocity. A trend of increasing error in the measurement was present as the time-lapse experiment progressed (B, $n=9$ embryos at each time point). Error bars represent standard deviation.

To quantify the error associated with our method, we used the fact that one of our measured velocities was not used in the CFD analysis. We compared the measured value with the computed value at this last vessel segment (Fig. 4.5). We also verified that the solution was not dependent on the mesh size chosen for the finite element grid by comparing the results for “fine” (red), “extra fine” (green) and “extremely fine” (black) mesh sizes. For all embryos, we analysed the error present during peak systolic flow. Decreasing the mesh size did not significantly change the computed velocities indicating mesh-independence of the solution (Fig. 4.5A). We performed error analysis on a total of 9 embryos that were followed by time-lapse microscopy. Interestingly, the error in the measurements changed very little from one embryo to another, even when a ten-fold difference in the velocity of the blood flow was present (compare Embryo 1 at 360 minutes to Embryo 2 at the same time point, Fig. 4.5A). The error increased significantly as the time-lapse experiment proceeded, regardless of the mesh size used in the finite element model (Fig. 4.5B). PEGylation reduces but does not abolish the adhesion of microspheres to the vessel wall. As the time-lapse progresses, the μ PIV became less accurate as the number of particles in circulation decreased, resulting in an increased uncertainty in the measurements.

4.4.5 Studying the Interaction of Molecular and Biomechanical Stimuli

One of the strengths of this current technique is that we are able to study the interaction of protein signals and biomechanical signals. Therefore, as a first application of the technique, we studied the effect of shear stress on vessel enlargement and the effect of perturbing this process with a gain-of-function in TGF- β signalling. During vascular development, vessels that

carry the most blood flow enlarge and those with the least flow regress (Thoma, 1893). Though this is a widely accepted concept, the relationship between the level of shear stress and changes in vessel diameter has never been investigated. We followed vessel diameter and shear stress in both enlarging (Fig. 4.6A) and regressing vessels (Fig. 4.6B). We analysed a total of 3 embryos (at 16-19 time points), with 1-2 locations per embryo, for a total of 5 vessels. We plotted the percent change in vessel diameter between consecutive frames with respect to shear stress levels present. We find that the natural logarithm of the shear stress correlates to the percent change in vessel diameter (Fig. 4.6C). From previous studies, we had observed that TGF- β injection during vascular remodelling in the embryo resulted in an increase in vessel diameters (unpublished observation). We therefore investigated whether TGF- β injection affected heart function and therefore altered shear stress levels, or whether the flow was unaltered but the response to shear stress was different. We injected embryos with TGF- β and analysed both changes in vessel diameter and shear stress levels (n=3 embryos, 7-9 time-points per embryo, 1-2 locations per embryo, total of 5 vessels). The range of shear stress present in TGF- β injected embryos did not differ from control embryos (p=0.726). When plotted on a semi-ln plot, however, a clear increase the rate at which vessels expanded for the same level of shear stress was present (Fig. 4.6D, p<0.0001). Though the intercept of the line was higher, the slope of the line was unchanged (p=0.926).

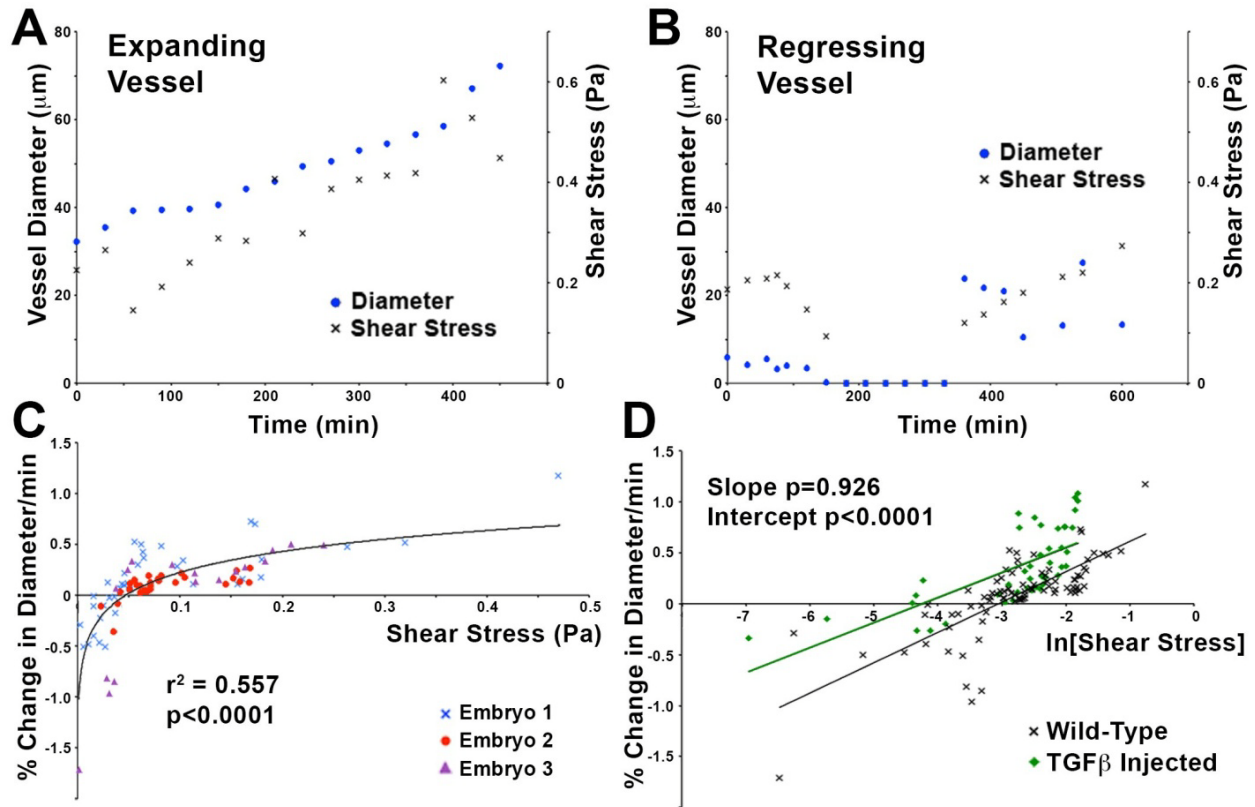


Figure 4.6- Vessels enlarge and regress proportional to the logarithm of the shear stress. The effect of shear stress on vessel diameter was studied by following both diameter (blue dots) and shear stress levels (black crosses) in enlarging (A) and regressing vessels (B). In the second example (B), the vessel regressed completely (150-330 minutes) before resprouting from the same location. The percent change in vessel diameter per minute was proportional to the natural logarithm of the shear stress (C, $p < 0.0001$). TGF- β injected embryos were then analysed to investigate perturbed vessel enlargement (D). Injection of TGF- β did not affect the level of shear stress present ($p = 0.726$) but did cause an increase in the rate of vessel enlargement (D). Data are plotted on a semi-ln plot. P-values were calculated using a two-tailed t-test in Prism.

4.5 Discussion

Hemodynamic signals are necessary for proper vascular development; however, the complexity of measuring shear stress levels in real time has hindered the study of the role of fluid forces in development. We previously showed that in unbranched vessels of the embryo, the velocity profile in the vessel is parabolic throughout the cardiac cycle (Jones et al., 2004). This occurs because two fluid dynamics parameters, the Reynold's number and the Womersley's number, are both very small for embryonic blood flow (i.e., less than one). It is because of these relatively simple flow dynamics that velocity, pressure drop and shear stress can accurately be calculated from the measured blood flow velocities. Though our results use embryos at the onset of blood flow, this technique can also be applied to embryos at older stages. Certain assumptions, however, such as the application of the Fahraeus relationship to calculate hematocrit, should be verified for older embryos before extending the technique to later stages.

One of the most significant limitations to the μ PIV method is the adhesion of the tracer particles. Though PEGylation of the particles increased their time in circulation to approximately 16 hours, the errors associated with the velocity measurements increased as the time-lapse progressed. We chose to restrict our analysis to data from the first 10 hours due to this limitation. Avian embryos can survive for 2-3 days in ex ovo culture, and we have found that the loss in AcLDL signal in the vessel wall over this period of time is not prohibitive. If the circulation time of the tracer particles could be further increased, it should be possible to extend this technique to follow vascular development and hemodynamics over a period of several days. We have tested particles with different surface charges, hydrophobicity and blocking reagents. None of these factors reduced the adhesion of particles to the vessel walls. PEGylation is currently the

state-of-the-art for creating “stealth” particles. We did not test different chain lengths, and small improvements on the time in circulation may be possible by optimizing these factors.

The alternative to the use of tracer particles is to make flow measurements using techniques that do not require the use of tracers, such as Doppler OCT. Doppler OCT cannot produce images of the vascular network geometry at high enough resolution to accurately predict shear stress and pressure, but this could be resolved by combining Doppler OCT with confocal microscopy. The computational aspects of our current method could then be directly applied to such data sets. Combined OCT/confocal microscopy systems have previously been developed (Brinkmann et al., 2008; Podoleanu et al., 2004). The main disadvantage, however, is that such specialized and expensive equipment would limit the applicability of the method to labs that are specialized in this technique. Our μ PIV-based method is therefore much more accessible to most groups. It requires only: 1) a micro-injector, 2) a fluorescent microscope, 3) a high-speed camera, and 4) a software license for a CFD solver. The cost of high-speed cameras has fallen drastically over the last decade. For any avian embryology lab, the cost of implementing this technique is reasonable.

Most fluid dynamic calculations do not include non-Newtonian properties of blood. Instead, a constant value of the viscosity based on the hematocrit is used. In large vessels, this approximation is justified, however, it is not appropriate for embryonic blood vessels. Embryonic blood flow is slow and shear-rate dependent effects are most pronounced at low shear rates. We were obliged, however, to extrapolate our previous viscosity data with respect to embryonic stage. Our previous results had shown that there was no change in apparent viscosity of blood with respect to stage when the hematocrit is below 50% (Al-Roubaie et al., 2011). Therefore, extrapolation results in similar values for the viscosity as using the data directly for

the older embryos. Given that the embryonic vessels have hematocrits well below 20%, the assumption that stage has little effect on the viscosity is relatively safe. The inclusion of variation of the viscosity for hematocrit and shear rate in the flow calculation is a significant improvement on previous calculations of embryonic shear stress levels.

Our application of μ PIV with CFD to investigate vessel enlargement found that vessels enlarge and regress proportional to the natural logarithm of the shear stress. This makes physiological sense, since there must be a maximum rate at which vessel can expand. We also found that injection of TGF- β injected embryos causes an increase in the rate of vessel enlargement even though shear stress levels are unchanged. Interestingly, the injection affected the intercept but not the slope of the regression on a semi-ln plot. We are investigating agent-based simulations of cell movements to explain how a logarithmic relationship can arise between shear stress levels and vessel expansion/regression, as well as to examine which factors could be affected after TGF- β injection that would lead to the observed changes in behaviour. These results highlight the fact that neither molecular nor biomechanical stimuli should be studied in isolation. These signals interact, such that molecular signals affect how endothelial cells respond to blood flow, and vice versa.

This work represents the first technique to follow changes in flow dynamics as the vasculature remodels. It will allow for quantitative analysis of the relationships between hemodynamic parameters, such as shear stress and pressure drop, and biological processes in vascular remodelling. The resolution is high enough to investigate cellular mechanisms of remodelling in relationship to the flow. As such, this technique will allow investigators to begin to explore the interplay of flow dynamics and cellular events in vascular development.

4.6 Materials and Methods

4.6.1 Simultaneous Imaging of Vascular Remodelling and Blood Flow Dynamics

Fertilized quail eggs (*Coturnix japonica*) were incubated at 37°C until they reached a stage of 12-14 somites or HH11. About 1 mL of albumin was removed from the egg by puncturing the shell with a syringe. A small window was cut into the top of the eggshell and the entire egg was poured into a 6 cm petri dish, ensuring that the embryo remained on the top of the yolk (Fig. 4.7A). The embryos were injected intravascularly using a Picospritzer III microinjector (Parker Hannifin) and a fine capillary glass needles with a tip diameter of approximately 5 to 10 μm (Fig. 4.7A, Sutter Instruments, BF100-50-10). AlexaFluor 488 acetylated low-density lipoprotein (AF488-AcLDL, Invitrogen, L-23380) was injected to label endothelial cells and FluoSphere carboxylate-modified polystyrene microspheres (0.5 μm diameter red, Invitrogen, F-8812) were injected as tracer particles to image the flow dynamics. Before injection, amino-PEG (Laysan Bio, MPEG-NH₂-5000-1g) was covalently attached to the surface of the microspheres using a reduction reaction according to the manufacturer's instructions. Some minor modifications were made to the protocol. When washing the microspheres after the reduction reaction, an ultracentrifuge at 170,000g was used instead of the recommended 25,000g. PEGylation made the particles much more neutrally buoyant such that the recommended centrifugation was ineffective. Furthermore, sodium azide was not added. A small amount of blue food dye (30 v/v%) was added to all solutions to visualize the injection and ensure delivery specifically into the circulatory system. The volume of injection was titrated based on the volume of dye expunged (approximately 0.1 μl injected per embryo). Before and after injection, embryos were rehydrated with Ringer's solution. Only embryos where the injection was specific

to the vasculature on the first attempt were kept for time-lapse imaging. In general, a dozen embryos were injected and the most successful injection, assessed on the fluorescent microscope, was used for each experiment. Embryo culture for time-lapse microscopy was done as previously described (Al-Roubaie et al., 2012). A large square hole was made in the lid of the petri dish (approximately 2 cm by 2 cm), as well as two smaller “ports” about the size of a syringe needle (Fig. 4.7B). The square hole was covered with a Teflon membrane, which is permeable to air and not to moisture (YSI, 066156). The Teflon membrane was affixed using silicon vacuum grease (Dow Corning, 1597418). The lid was sealed onto the petri dish using parafilm. The petri dish was then filled with additional warmed albumin through the “ports” until the embryo was in direct contact with the Teflon membrane. The ports were plugged with silicon vacuum grease (Fig. 4.7B). Embryos were imaged on an upright fluorescence microscope equipped with an AxioCam MRC for images of the vascular morphology and a high-speed camera (Photron FASTCAM Ultima APX-RS) for images of the microsphere motion (Fig. 4.7C). A homemade heater box was built around the microscope stage to keep the microscope stage at 37°C, using a small room heater and a temperature controller (VWR, 10171-512). Endothelial cells were imaged every 15 minutes. Blood flow dynamics were imaged at 250 fps for 2 full cardiac cycles (equivalent to 2 seconds of imaging time), once every 2 hours.

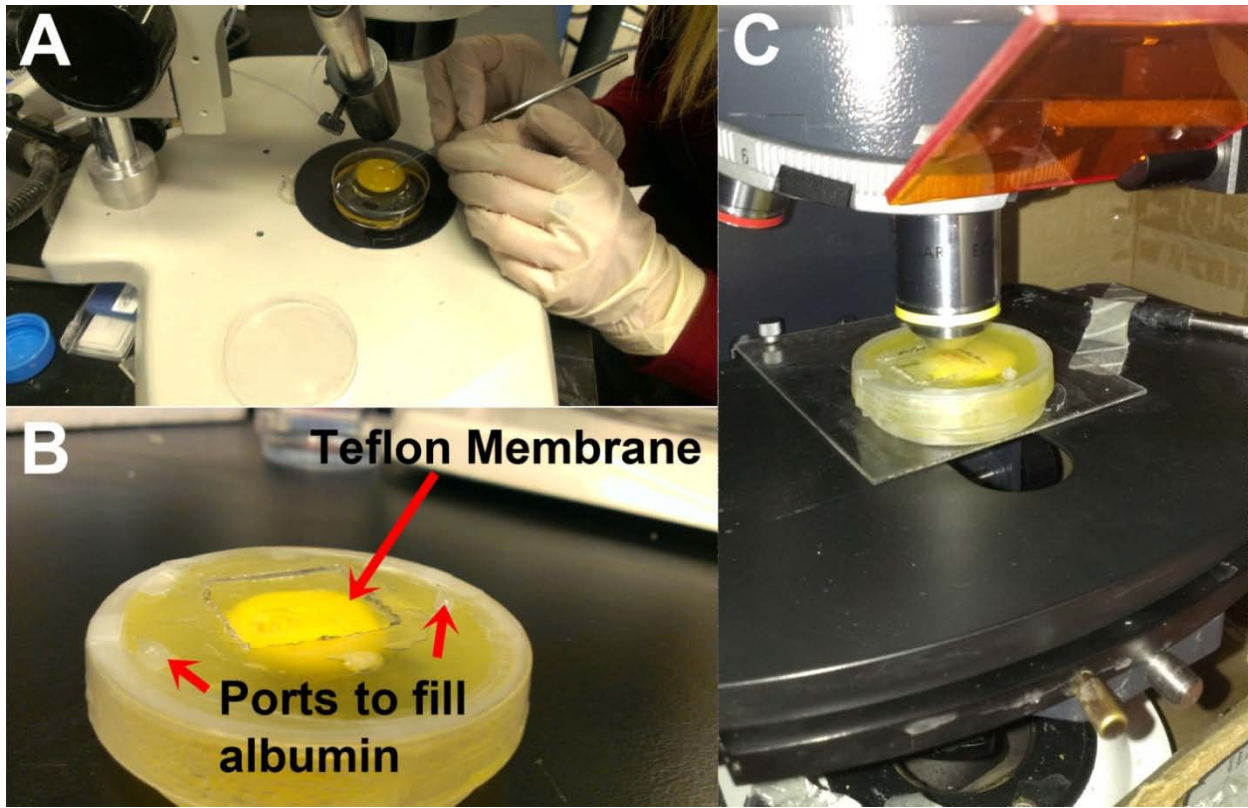


Figure 4.7– Summary of embryo culture technique. Quail eggs were incubated until the appropriate stage and then transferred to a 6 cm petri dish. The embryos were injected with AlexaFluor 488-acetylated low-density lipoprotein and red microspheres using a micro-injector (A). The lid of the petri dish was modified to create a Teflon window that is permeable to air but not to moisture (B). The lid was then sealed on the petri dish using parafilm. Additional warmed albumin was added to the dish, using small “ports” located either side of the Teflon window. These were then sealed with vacuum grease. The petri dishes were transferred to a heated microscope stage (C). The vasculature was imaged every 15 minutes and the motion of the microspheres was imaged every 2 hours.

4.6.2 Creation of an Image Mask

A MATLAB program was developed in Simulink for the post processing of acquired images. At each time point, the green image (endothelial cells) and the stack of 500 red images (microsphere motion) were flattened into a single image. The flattened image was converted to a grey-scale image. A gamma correction was applied to control the overall brightness of the image and the contrast was adjusted by linearly scaling the pixel values (see Supplemental Fig. 1 for the Simulink block diagram). The gamma parameter and the break point of the straight line segment were altered manually to obtain the best possible contrast. The illumination was equalized using Histogram Equalization. To reduce noise, a median filter was applied to the image, and then the image was thresholded to obtain a binary image used as a “mask”. The image mask was used to subtract all background noise and make non-flow regions into pure black. It was applied to each individual frame of the microsphere motion before μ PIV analysis.

4.6.3 Identification of Walls, Centreline and Local Vessel Radius

To identify the inner wall boundaries of perfused vessels, Matlab’s “edge” function was applied to the image mask, specifying a Canny algorithm. The Canny edge detector creates a rough estimate of every possible edge contour within the image; the edge information was saved to a binary edge detected map. Since there were still some discontinuous edges in the image, edge points were linked to nearby edges using an edge connection algorithm based on a least squares method to create a closed, continuous boundary (Hoover and Goldbaum, 2003). The centreline of each vessel was found by skeletonizing the image mask. Using a search based

method within MATLAB, the distance between the centreline and the closest black pixel of the edge map was measured to define the local radius of vessel.

4.6.4 Micro-Particle Image Velocimetry Analysis

Micro-PIV was used to measure velocity waveforms during the cardiac cycle at inlets and outlets. A pair of images was divided into smaller areas called interrogation windows. These interrogation windows were compared in two consecutive images using a MATLAB code to seek the most likely position of these windows from one frame to other one. The velocity of the particles can be obtained by calculating the distance between the centres of these two interrogation windows. Therefore the local velocity vector is:

$$\vec{v}(x, y, t) = \frac{\Delta x(x, y, t)}{\Delta t} \quad (4.3)$$

In this equation, Δx denotes the displacement the cluster after a time interval Δt of between two consecutive frames. An interrogation window size of 16×16 pixels was used. Flow inlets and outlets were chosen far from branch points. Since the Reynolds number for the flow is very close to one and the Womersley number is less than one (Jones et al., 2004), entrance length effects are on the order of one micron, hence a fully developed parabolic velocity profile was assumed for the μ PIV analysis.

4.6.5 Blood Rheology

A relationship between hematocrit and embryonic stage was obtained by injecting FITC-dextran (Sigma-Aldrich, FD40S) into quail embryos. Line scans on live embryos were performed

on a heated confocal microscope stage as previously described (Jones et al., 2004). Several images were obtained at different embryonic stages and vessel diameters. Images were thresholded to obtain the tube hematocrit and the vessel diameter was measured. For smaller vessels (tube diameter less than $300\mu\text{m}$), the hematocrit was adjusted for tube diameter based on the Fahraeus equation (Pries et al., 1990). A relationship between the discharge hematocrit and embryonic stage was developed (Fig. 4.2). A cubic fit was used as method to interpolate between stages in the computational model. Blood viscosity was calculated based on embryonic stage and vessel diameter, using a Carreau relationship that we previously developed to describe the non-Newtonian behaviour of embryonic blood flow (Al-Roubaie et al., 2011). The constants were re-evaluated from the paper to include a larger number of hematocrit values. We interpolated (for hematocrit) and extrapolated (for embryonic stage) to establish the value of the constants (μ_∞ , μ_0 , λ and N) for the time-lapse experiments.

4.6.6 Computational Fluid Dynamics

The vascular geometry obtained by image processing and the inlet and outlet velocities acquired by μPIV were imported into a CFD solver (COMSOL Multiphysics). The governing equations inside the vessels (i.e., continuity and momentum equations for laminar, unsteady, non-Newtonian, incompressible flow) were solved using a finite elements method. From N inlets and outlets, the flow rates at $N-1$ points were set as boundary conditions. For the last outlet, a straight section of vessel was added to allow the flow to reach fully developed conditions and help the convergence of the numerical solution inside the domain. The fully developed boundary condition was applied at the extended outlet of the domain (depends on Reynolds number), i.e.,

$\frac{\partial}{\partial x} = 0$. Vessel walls were assumed to be rigid and impermeable with no slip boundary conditions. The rigid wall assumption was confirmed using high-speed images of the vessel wall (Supplemental Movie 5). Since the domain has curved geometries, the numerical algorithm was applied on a non-orthogonal curvilinear coordinate framework. Mesh generation and solution was performed with COMSOL. The domain was meshed with extremely fine free triangular meshes. Numerical simulations were conducted using a computer equipped with two Quad Core Intel(R) Processors (8 nodes each 3.40 GHz).

4.7 Sources of Funding

EAVJ was supported by grants from the Sick Kids Foundation of Canada (NI12-029) and a grant from Life Science Research Partners. RLL was supported by grants from Canadian Institute of Health Research (MOP-119292). A McGill Engineering Doctoral Award supported SG.

4.8 Acknowledgements

We thank Espen Jahnsen for insightful discussion and assistance in the production of time-lapse recordings.

4.9 Supplementary Information

Supplementary information available online at

<http://dev.biologists.org/lookup/suppl/doi:10.1242/dev.127019/-/DC1>

Supplemental Movie 1 – Blood velocity analysis during vascular remodelling. Results of the analysis of blood velocity changes during remodelling are presented. The left panel shows the endothelial cell behaviour during the time period of analysis. Endothelial cells were labelled with AlexaFluor488 acetylated low-density lipoprotein. Both intussusceptive angiogenesis (cyan arrowhead) and sprouting angiogenesis (yellow arrow) are visible in this example. The centre panel shows the velocity vectors for the blood flow during peak systole in the network. Velocity vectors in the middle panel are sized based on the maximum velocity at that specific time point (i.e., scale is relative). The right panel shows the absolute velocity magnitude during peak systole in these vessels. All scale bars represent 100 μm .

Supplemental Movie 2 – Pressure changes over the time-lapse experiment. Results of the pressure calculations are presented. The left panel shows the endothelial cell behaviour during the time period of analysis. Endothelial cells were labelled with AlexaFluor488 acetylated low-density lipoprotein. The centre panel shows the relative pressure, where red represents the highest pressure at that specific time point. The right panel shows the same data, but the colour scale remains constant throughout all time points. All presented values are for peak systole, however, blood flow dynamics were analysed for the entire cardiac cycle at each time point. All scale bars represent 100 μm .

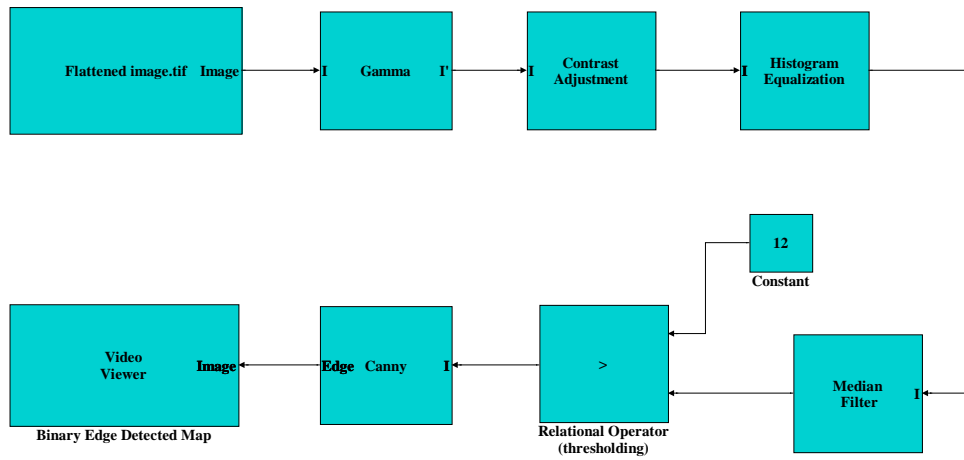
Supplemental Movie 3 – Shear stress and vorticity analysis during vascular remodelling. Results of the shear stress and vorticity calculations at peak systole are presented. The left panel shows the endothelial cell behaviour during the period of analysis. Endothelial cells were labelled with AlexaFluor488 acetylated low-density lipoprotein. The centre panel shows the

results for the shear stress calculations, with a constant colour scale for all time points. The right panel shows the results for the vorticity calculations, with a constant colour scale for all time points. All scale bars represent 100 μm .

Supplemental Movie 4 – Computational analysis can accurately predict flow pattern in embryonic yolk sac blood vessels. To test the ability of the computational technique to accurately model flow, we investigated blood flow in an older embryo (HH15) where a region of flow reversal was observed. The flow was visualized by injection of fluorescent microsphere and high-speed imaging (250 fps, A). The velocity of the blood flow for the two vessels on the left was used as the input to the CFD analysis (A). The resulting velocity vectors (B) show that the solver accurately determined the pattern of flow including the flow reversal in the vessel on the right. Movie played back at 1/8 speed.

Supplemental Movie 5 – Verification of the rigid wall assumption. Our computational analysis assumed rigid vessel walls. To verify this assumption, we imaged the movement of the vessel wall with a high-speed camera. The green labelling shows the endothelium and the red images show the fluorescent particle tracer motion. No motion of the walls is apparent over the entire cardiac cycle, thereby validating the rigid wall assumption. Movie played back at 1/3 speed.

Supplementary Figures



Supplemental Figure 1 – Block diagram of the Simulink MATLAB program for image processing. After conversion of image stacks into a flattened image, a series of actions was applied to the image to acquire a binary edge detected map using MATLAB image processing toolbox. The detailed schematic view of used toolboxes and their order is depicted here for more information.

5 Flow Dynamics Control The Location of Sprouting and Direct Elongation During Developmental Angiogenesis

5.1 Preface

The following manuscript was published in 2015 in the journal *Development*, 142.23 (2015): 4151-4157. In this paper, we applied our previously developed technique (chapter 4) to study the role hemodynamic present during angiogenic sprouting. We examined how flow dynamics influence vascular morphogenesis, namely sprouting behavior during angiogenesis. Both arterial and venous vascular patterns were monitored. Time-lapse recordings were subjected to analysis of flow dynamics based on particle image velocimetry. Quail embryo capillary plexus *in vivo* behavior during normal remodelling was investigated.

We found that sprouts only form from a vessel at low pressure towards a vessel at higher pressure, such that there is a positive pressure difference at the sprouting location. Within the lower pressure region, sprouts localised at the lowest minimum in shear stress once locations where streams merge were excluded. The results underlined that flow dynamics are predictive of the site of sprout initiation. These parameters enabled us to successfully predict sprout location. We presented a logarithmic relationship between the elongation rate and the pressure difference between the vessels. Therefore, hemodynamics are suggested to regulate the direction and rate sprout elongation.

Flow Dynamics Control The Location of Sprouting and Direct Elongation During Developmental Angiogenesis

Siavash Ghaffari^{1,2}, Richard L. Leask², Elizabeth A.V. Jones^{1,2,3*}

¹ *Lady Davis Institute for Medical Research, McGill University, 3755 Ch. Côte-Ste-Catherine, Montréal, QC, H3T 1E2, Canada.*

² *Department of Chemical Engineering, McGill University, 3610 University St., Montréal, QC, H3A 0C5, Canada*

³ *Department of Cardiovascular Science, KU Leuven, UZ Herestraat 49 - box 911, 3000 Leuven, Belgium*

To whom correspondences should be addressed: Elizabeth A.V. Jones, Centre for Molecular and Vascular Biology, KU Leuven, UZ Herestraat 49 - box 911, 3000 Leuven, Belgium, Tel. +32 16 34 75 58; Fax. +32 16 34 60 01; Email: liz.jones@med.kuleuven.be

Short Title: Hemodynamic during angiogenesis

5.2 Abstract

Angiogenesis is tightly controlled by a number of signalling pathways. Though our understanding of the molecular mechanisms involved in angiogenesis has rapidly increased, the role that biomechanical signals play in this process is understudied. We recently developed a technique to simultaneously analyse flow dynamics and vascular remodelling by time-lapse microscopy in the capillary plexus of avian embryos and used this to study the hemodynamic environment present during angiogenic sprouting. We found that sprouts always form from a vessel at lower pressure towards a vessel at higher pressure. We found that sprouts form at the location of a shear stress minimum, but avoid locations where two blood streams merge even if this point is at a lower level of shear stress than the sprouting location. Using these parameters, we were able to successfully predict sprout location in embryos. We also find that the pressure difference between two vessels is permissive to elongation, and that sprouts will either change direction or regress if the pressure difference becomes negative. Furthermore, the sprout elongation rate is proportional to the pressure difference between the two vessels. Our results show that flow dynamics are predictive of the location of sprout formation in perfused vascular networks and that pressure differences across the interstitium can guide sprout elongation.

Keywords: Angiogenesis, Hemodynamics, Time-lapse microscopy, micro-Particle image velocimetry, Computational fluid dynamics

5.3 Introduction

The vasculature is the first organ to form during development and it adapts to the onset of blood flow in part by forming new blood vessels through angiogenesis. The ability to control angiogenesis has important therapeutic applications for many diseases. Anti-angiogenic treatments used to treat tumours lead to transient vessel normalization, which causes a reduction in tumour invasiveness and better delivery of chemotherapeutic drugs (Carmeliet and Jain, 2011). In wet macular degeneration, defective angiogenesis leads to the formation of leaky vessels that damage the eye and lead to vision loss. Anti-angiogenic therapies can effectively stop and sometimes reverse the progression of macular degeneration (Tah et al., 2015). As such, there is significant interest in understanding the signals that induce or inhibit angiogenesis.

In the adult vasculature, endothelial cells exist in a quiescent state whereby little proliferation is present (Hanahan and Folkman, 1996; Hobson and Denekamp, 1984). Normal physiological levels of shear stress maintains endothelial cells in a quiescent state by inducing cell cycle arrest (Lin et al., 2000) and strengthening tight junctions (Lin et al., 2000). For sprouting to occur, however, endothelial cells must re-enter the cell cycle (Bai et al., 2014), loosen their attachment to neighbouring cells (Lampugnani and Dejana, 2007), degrade the local basement membrane (Siefert and Sarkar, 2012) and then invade the tissue to form a new vessel. Though shear stress is known to affect many of these pathways, very little is known about the effects of shear stress on angiogenesis. Two groups recently developed micro-machined flow cells that enabled them to alter shear stress and interstitial flow as endothelial cells sprout (Galie et al., 2014; Song and Munn, 2011). Both groups found that interstitial flow enhanced angiogenesis, however one found that shear stress inhibited sprouting whereas the other found that it induced sprouting (Galie et al., 2014; Song and Munn, 2011). Using an embryonic model,

our group has demonstrated that increasing blood viscosity, which increases shear stress, results in a decrease in vascular density (Chouinard-Pelletier et al., 2013). We showed by time-lapse microscopy that this occurs because of a decrease in sprouting angiogenesis. Changing viscosity, however, also altered other hemodynamic parameters such as the pressure drop through the network. These studies establish a role for flow dynamics in angiogenesis but a better understanding of the hemodynamic environment present *in vivo* during sprouting is needed to identify the causal stimuli.

The vascular network must not only deliver oxygen and nutrients to tissues, but it must also be hemodynamically efficient. If a new vessel forms in hemodynamically inefficient location, then a high resistance to flow will be present and limited flow will pass through that vessel. The production of a hemodynamically efficient vascular network can occur either by excessive production of blood vessels followed by the pruning of inefficient vessel, or by sprouting of new vessels in hemodynamically efficient locations in the first place. Though vascular networks do overproduce vessels and prune inefficient ones (Pries et al., 1990), this does not negate the possibility of a bias in the site of sprout initiation in perfused vascular networks. It therefore makes physiological sense that the forces created by blood flow could influence the angiogenic process.

5.4 Results

5.4.1 Sprout Location Can Be Predicted Based on Flow Dynamics

To study the role that flow dynamics play in the process of angiogenesis, we used a technique to simultaneously image vessel morphology and flow dynamics by time-lapse

microscopy in the capillary plexus of avian embryos undergoing vascular remodelling (Ghaffari et al., 2015b). We injected AlexaFluor 488-labeled acetylated low-density lipoprotein (AF488-acLDL), which specifically labels endothelial cells and macrophages (Brown et al., 1980; Hallmann et al., 1987). AF488-AcLDL labels not only perfused vessels, but also sprouting endothelial cells. We then injected red fluorescent microspheres to follow blood flow dynamics and imaged the microspheres with a high-speed camera. We analysed the pattern of blood flow present during sprouting in the arterial plexus of three quail embryos as well as the venous plexus of three additional quail embryos, for a total of 6 time-lapse recordings (Fig. 5.1A). Early in vascular development, a spatial separation exists such that the rostral capillary plexus is venous and the caudal plexus is arterial. The motion of the microspheres was analysed using a technique called micro-particle image velocimetry (μ PIV) to calculate the velocity of the blood. Micro-PIV was only used to make velocity measurements in straight vessel segments that led in and out of a region of interest. These measurements were then used as the input for a computational fluid dynamic solver to calculate flow in the entire region of interest, around the growing sprout. Flow dynamics were analysed starting 30 minutes before the sprout was visible (yellow arrowheads) and continued until the new vessel lumenized and carried flow (Fig. 5.1B). The computational solver calculates blood velocity in the entire region of interest from the micro-PIV inputs (Fig. 5.1C-D), as well as calculating shear stress, pressure drop and vorticity (Supplemental Movie 1-3).

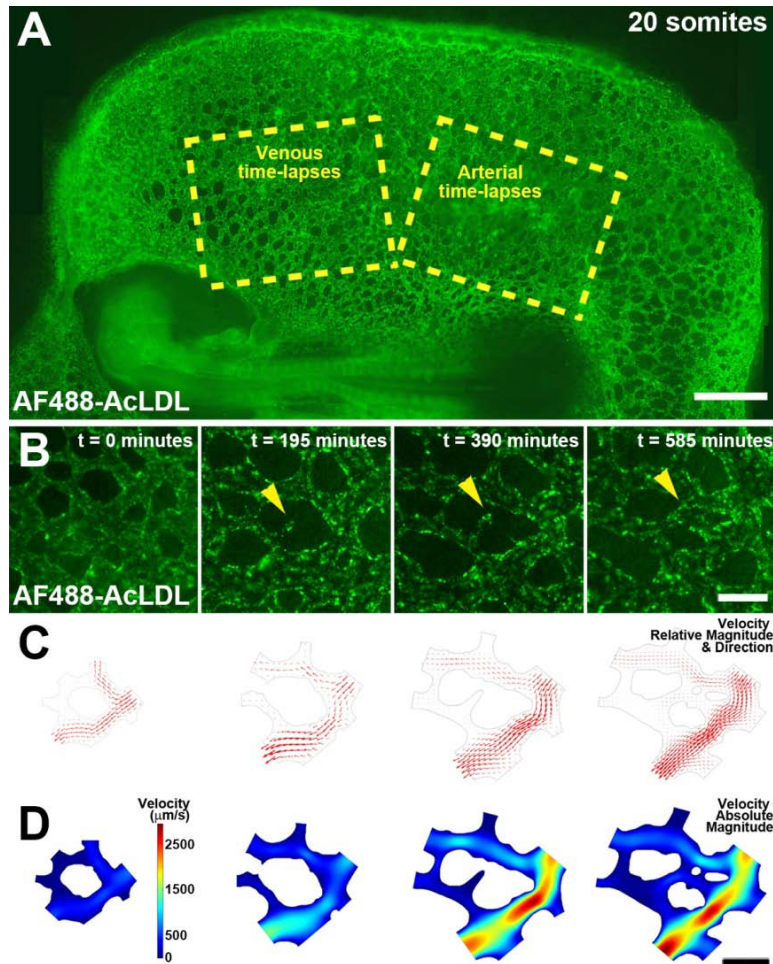


Figure 5.1– Fluid dynamic analysis over a ten-hour time-lapse period. All time-lapse movies started with embryos at 12-14 somites (or Hamburger Hamilton Stage 11) and embryos were imaged for a total of 12-16 hours. The flow dynamics during sprouting angiogenesis were analysed for a total of 6 embryos, 3 in the arterial region of the capillary plexus and 3 in the venous region (A). Analysis of the time-lapse recordings was performed on data from 30 minutes before the sprout was first observed until the new vessel lumenized and flow was present in the new vessel (B, yellow arrowheads indicate sprout). Blood flow velocity and pattern was determined for the entire cardiac cycle however only values for peak systole are presented (C, D, Supplemental Movie 1). By combining viscosity estimates with the velocity profiles in the vessels, the relative pressure (Supplemental Movie 2), shear stress (Supplemental Movie 3) and vorticity (Supplemental Movie 3) were calculated. Scale bars; 1000 μm (A), 100 μm (B-D).

We first investigated the relationship between flow parameters and the location of sprout initiation. We found that sprouts consistently formed from vessels at lower pressure towards vessel at higher pressure (n=6 of 6 embryos, $p= 0.014$, Fig. 5.2). The contour plots of relative pressure 30 minutes before sprout formation are presented, both for the arterial regions of the plexus (Fig. 5.2A) and the venous regions (Fig. 5.2C). The location and direction of sprouting are identified by the black arrows (Fig. 5.2A, C) as observed in the green images of vascular morphology after the sprout has formed (Fig. 5.2B, D, yellow arrowheads). The average pressure difference between the initiation site and the opposite vessel (i.e. the one towards which the sprout is extended) was of the same order of magnitude in all embryos. Pressure differences were normalized by the distance between the two vessels. The average value was +2.1 Pa/mm (standard error = 0.09, n=3) for arteries and +1.7 Pa/mm (standard error = 0.09, n=3) for veins. Though sprouts formed from lower towards higher pressure vessels, the location and direction of sprouting was not at the maximum pressure difference in any of the time-lapse experiments.

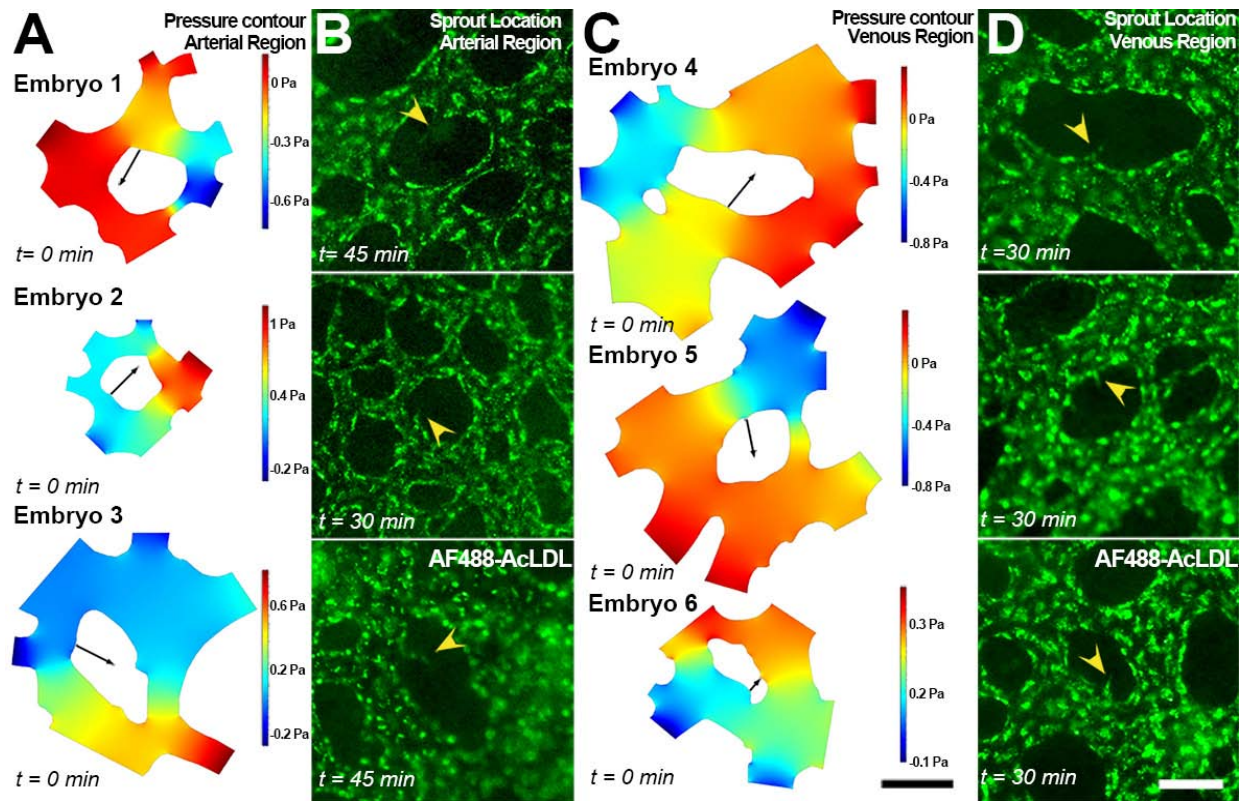


Figure 5.2– Sprouts form from vessels at lower pressure towards vessels at higher pressure. Contour plots for the relative pressure in all 6 embryos followed by time-lapse microscopy are presented (3 arterial, A-B, and 3 venous, C-D). Plots represent calculated relative pressure just prior to the onset of sprouting (30 minutes before the sprout is visible, A, C). Sprout location is shown in the green image of the vascular network (B, D) and indicated on contour plots by the black arrows (A, C). A positive pressure differential between the two vessels was always present, both for arteries (A) and veins (C). Scale bar: 100 μm .

Shear stress has been shown to play a significant role in controlling angiogenesis. We therefore investigated the level of shear stress on the endothelium when sprouting initiated (i.e. 30 minutes prior to sprout appearance, Fig. 5.3). Shear stress contour plots just prior to sprouting for the three arterial embryos are shown in Figure 5.3A. We plotted the level of shear stress with respect to distance along the endothelium (Fig. 5.3B). The black lines and arrows in Figure 5.3A indicate the arc length represented in the x-axis of Figure 5.3B ($x=0$ at the bottom of the arrow). Shear stress levels were plotted for a subsection of the lower pressure region, however plots of the entire region are available in Supplemental Figure 1. We found that for all arterial time-lapse recordings, the location of sprouting can be identified by a local minimum in shear stress (sprouting location indicated by black arrows, $n=3$ of 3 embryos, Fig. 5.3B). Our previous results had indicated that shear stress inhibited sprouting angiogenesis in the venous but not the arterial plexus (Chouinard-Pelletier et al., 2013). In our venous time-lapse experiments, the sprout location was not associated with any specific pattern or level of shear stress (data not shown). One occurred at a minimum; the second at a midpoint; and the third was very close to the point with highest level of shear stress in the region. Therefore, in veins, our current results do not support a correlation between the level of shear stress and the sprouting location.

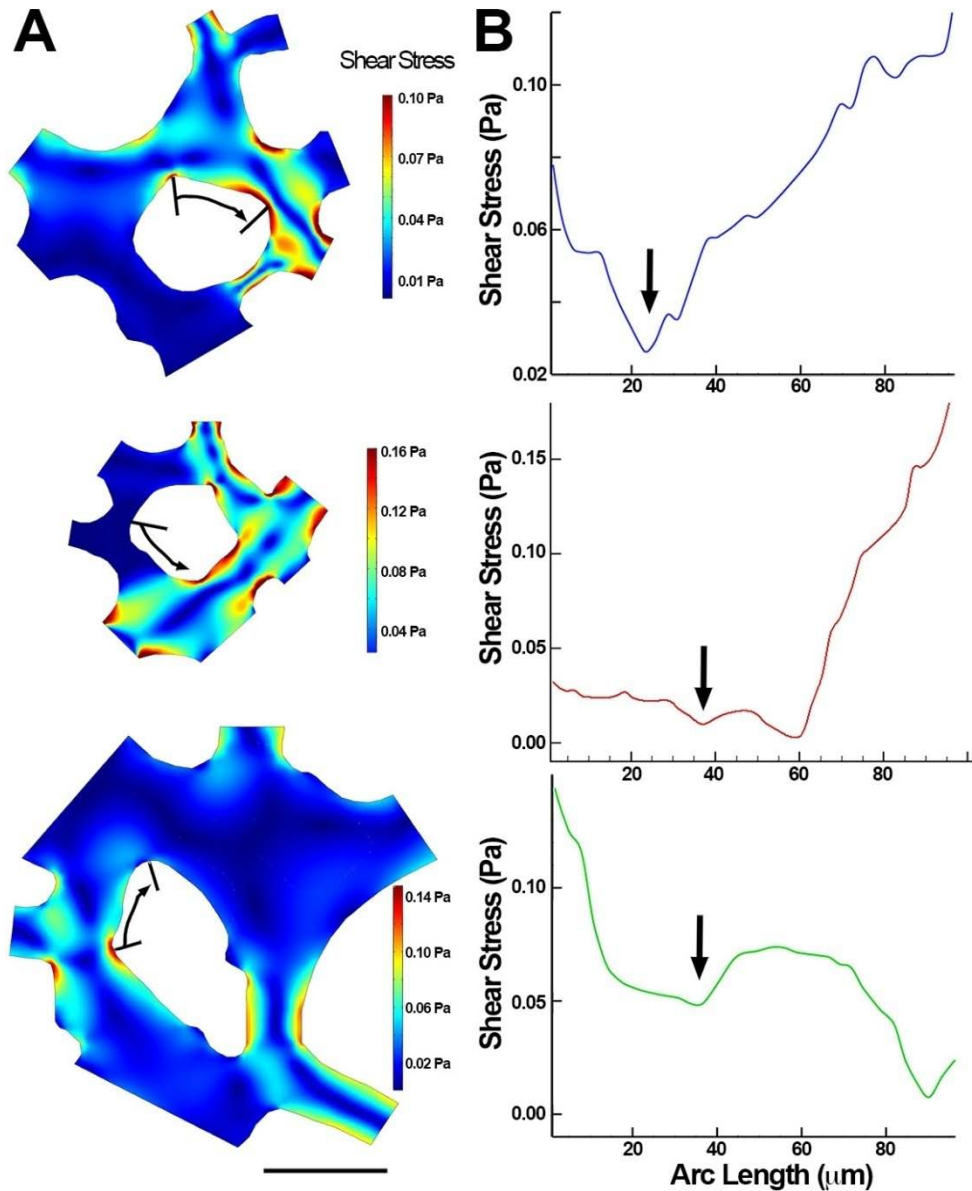


Figure 5.3– Sprouts form in a local minimum of shear stress. Contour plots show shear stress levels for a subsection of the lower pressure region in the arterial vascular network of three embryos, 30 minutes prior to the sprout being visible (A). Black lines and arrows indicate the starting location and the direction for the arc length that is plotted as the x-axis in panel B. Data for the entire arclength is presented in Supplemental Fig. 5.1. Sprout location is indicated by a black arrow in the plot of shear stress versus arc length (B, 24 μm for embryo 1, 36 μm for embryo 2, 36 μm for embryo 3). Sprouting location represents a local minimum in shear stress for all three embryos. Scale bar: 100 μm .

Though sprouts in the arterial plexus formed at a local minimum in shear stress, this was not always the absolute minimum. We investigated flow patterns at all shear stress minimum (Fig. 5.4A, blue arrow represents sprouting location, orange arrow represents the second shear stress minimum in Embryo 1). We observed that non-sprouting shear stress minima occurred in regions where two streams of blood flow merged (Fig. 5.4A, n=3 of 3 embryos). Vorticity is the angular velocity of a fluid. Convergence or divergence of streams results in a sign change in the vorticity. Regions where streams converge can clearly be identified in the contour plots of the vorticity because the vorticity changes from a positive to a negative value (Fig. 4B, orange arrow indicating region with a change from red to blue). Though there is significant vorticity in this region, this occurs because of the angular velocity of the fluid that results from the streams converging and not because of the presence of recirculation. We plotted shear stress (Fig. 5.4C, E, G) and vorticity (Fig. 5.4D, F, H) for the entire region at lower pressure. If points where the vorticity passes through zero are excluded from the analysis, then the lowest minimum in shear stress defines the location of sprouting (n=3 of 3 embryos, p=0.010).

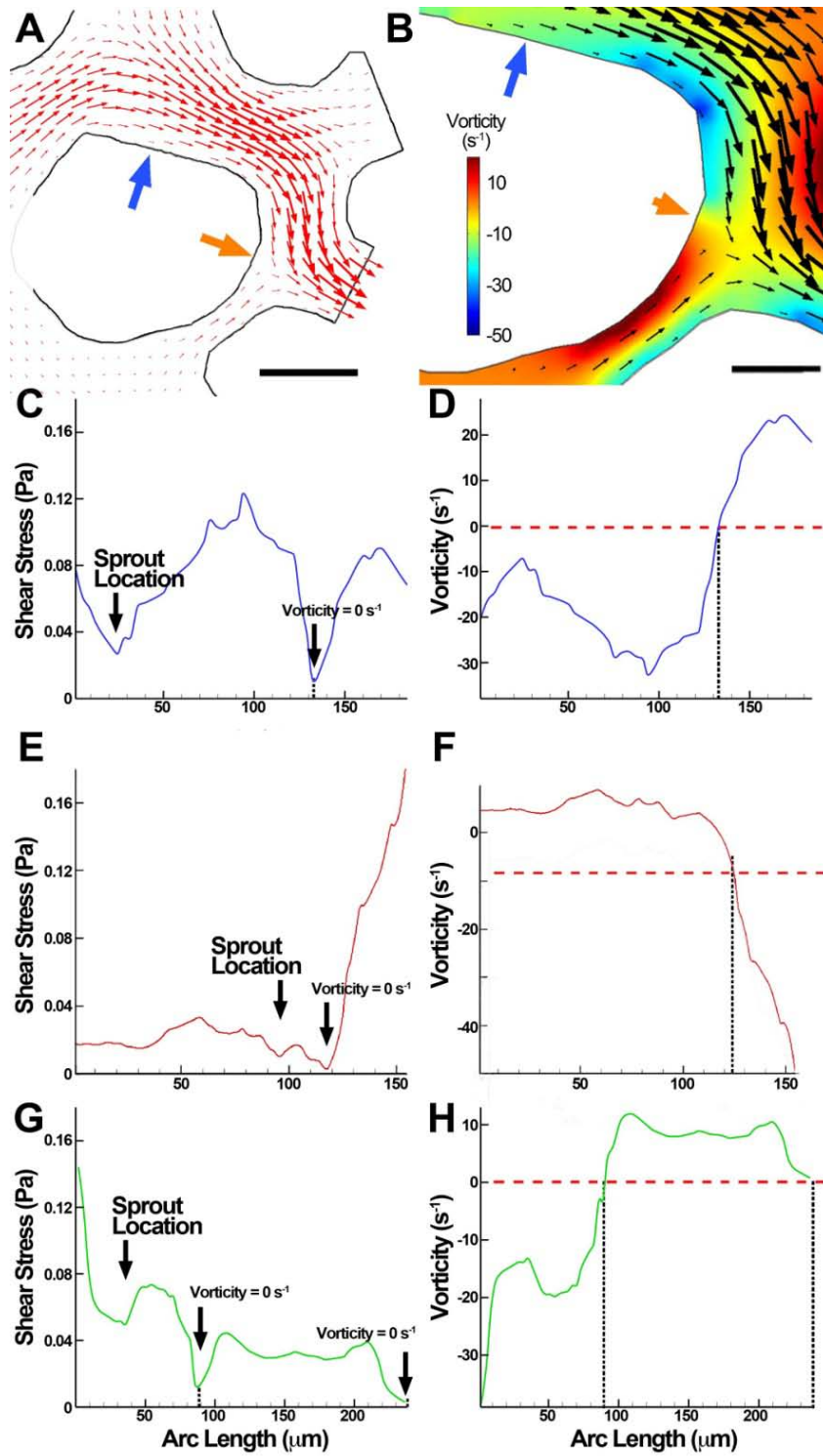


Figure 5.4– Sprouting never occurred at locations where two blood flow streams merge. Velocity plots show locations of low shear stress points (blue and orange arrows) with respect to the flow patterns present (A). The blue arrow indicates sprouting location and the orange arrow indicates a non-sprouting

shear stress minimum. The non-sprouting minimum occurs at a point where streams merge and a change in sign of the vorticity is present (B, blue to red transition in contour plot). In the first embryo, two shear stress minima are present at 22 μm and 132 μm (C, plots show half the total arc length representing the lower 50% of pressure values). The sprout forms at the first shear stress minimum (22 μm , or blue arrow in A, B). The latter shear stress minimum (132 μm , black arrow in A, B) represents a point where streams merge and a change in sign in vorticity is present (D). The exclusion of sprouting from locations where vorticity is zero was consistently observed in all three embryos (E-F for Embryo 2, and G-H for Embryo 3). Dotted black lines indicate locations where vorticity is equal to zero. Scale bar: 100 μm .

We next tested whether we could use these observations to predict sprouting location. We analysed flow dynamics prior to sprouting in the arterial region of 4 new embryos (Fig. 5.5). The region and time point that were analysed were chosen by one author but analysed by a different author, making the analysis blind to sprouting location. Sprouting location was restricted to the bottom 50% of pressure values (Fig. 5.5A). Within the lower pressure region, we identified all shear stress minima and all locations where vorticity equalled zero (Fig. 5.5B). Excluding locations with zero vorticity, the lowest minimum was chosen as the predicted sprout location (Fig. 5.5B). The actual sprout location was then assessed (Fig. 5.5C), blind to predicted sprout location, based on the green images of vascular morphology and the location of $x = 0$ from the pressure contour plots. In all embryos ($n = 4$ of 4 embryos, $p = 0.001$), we were able to correctly predict sprout location.

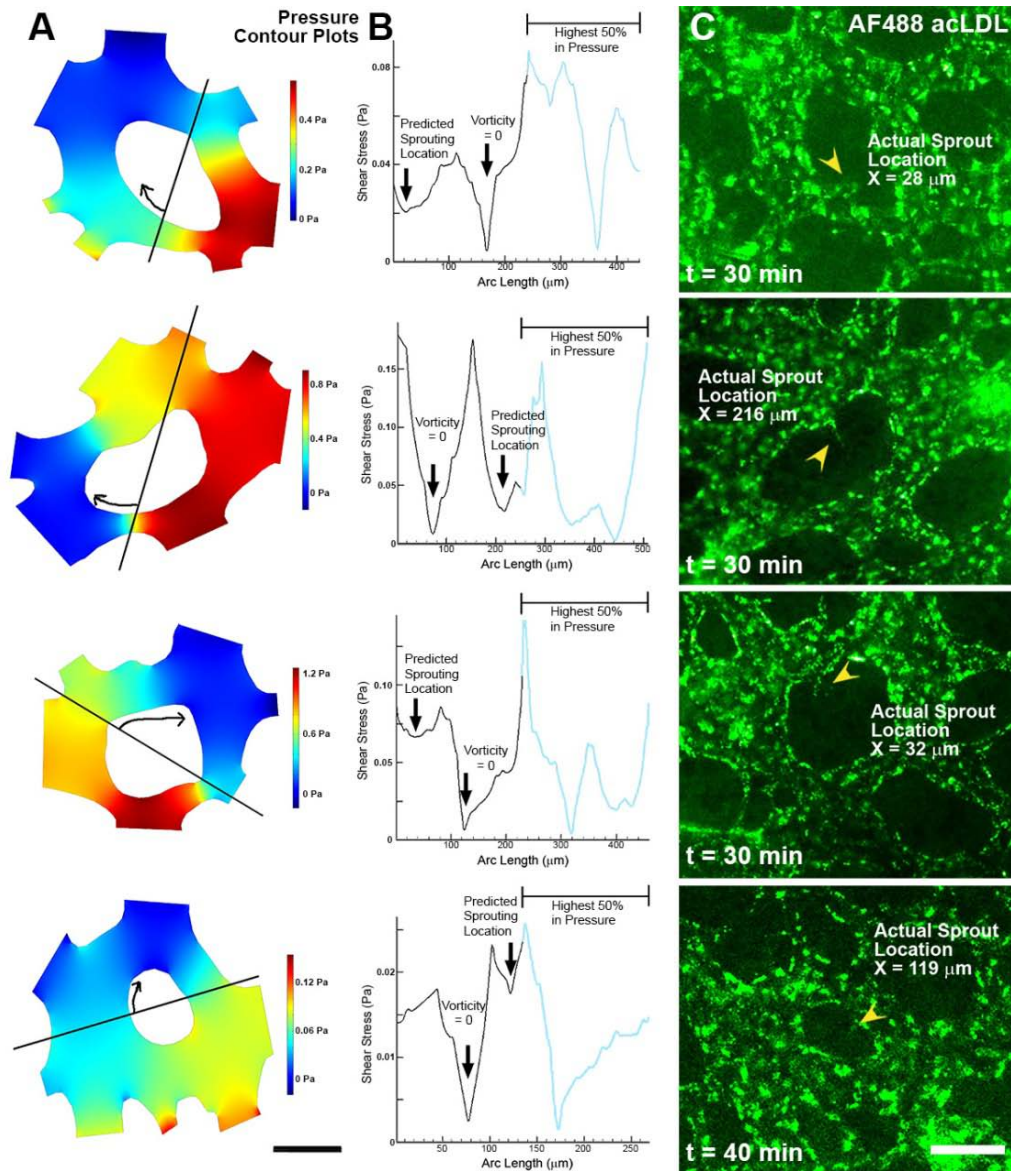


Figure 5.5– Application of these three hemodynamic parameters can predict sprouting location in perfused networks. The hemodynamic parameters for sprouting in 4 embryos were analysed blind to sprout location. Only the lowest 50% of relative pressure in each embryo were considered as possible sprouting locations (A). The base of each arrow in panel A indicates the start of the X-axis in panel B. Locations where the vorticity is equal to zero were identified and excluded from the analysis of shear stress minima (B). The lowest remaining shear stress minimum was chosen as the predicted sprouting location. When compared with the actual sprouting location (C), in all four cases the sprouting location was successfully identified ($n = 4$ of 4 embryos). Scale bar: 100 μm .

5.4.2 Sprout Elongation Rate is Proportional to the Pressure Difference Between the Two Vessels

We frequently observed that sprouts would extend and retract before finally connecting to form a lumenized vessels (Fig. 5.6A, yellow arrows indicate direction of sprout movement), as has been observed in other model systems (Murakami et al., 2006). We plotted the elongation rate of the sprouts (Fig. 5.6B), measured by the displacement of the tip of the sprout between two frames, and compared this to changes in the three analysed hemodynamic parameters in our system. We observed that regression of the sprout occurred when the difference in pressure between the vessels became negative (Fig. 5.6C, n=3 of 3 embryos). We therefore plotted the elongation rate with respect to the pressure difference between the two vessels (Fig. 5.6D). Negative elongation rates represent sprout regression. We found a logarithmic relationship between the elongation rate and the pressure difference between the vessels (Fig. 5.6E). The non-linear regression gave an r^2 value of 0.82 (Fig. 5.6D), whereas the linear regression on the semi-ln plot gave an r^2 value of 0.87 (Fig. 5.6E, $p < 0.05$). Thus, these results show that there is a significant association between the rate of elongation and the pressure difference between two vessels.

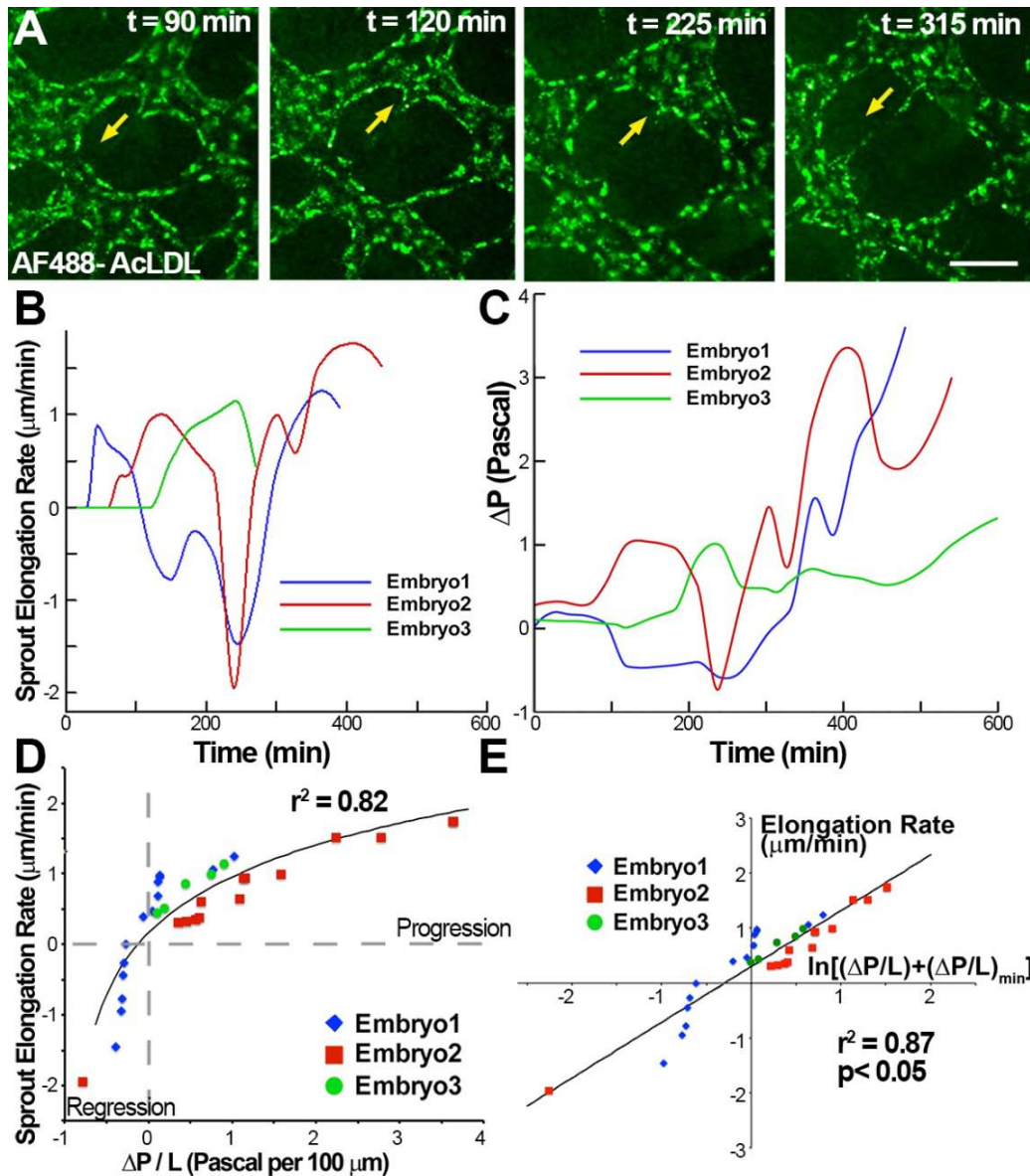


Figure 5.6- The rate of elongation is proportional to the magnitude of the pressure differential. Sprouts were often observed to extend and regress (A, yellow arrows indicate direction of sprout motion). When the pressure differential was plotted with respect to time, periods of sprout regression (B) were found to occur when negative pressure differentials were present (C) in all three arterial plexuses. The rate of elongation also strongly correlated with pressure differential between the vessels (D). Plotting the data on a semi-ln plot demonstrated a logarithmic relationship between these quantities (E). Pressure differentials were normalized by L , the distance between the two vessels. Scale bars: $100\ \mu\text{m}$.

In some time-lapse experiments, we observed the direction of elongation changing dynamically in relation to pressure differences between two vessels. This occurred in 2 of the 3 arterial time-lapse recordings. In one example, taken from Embryo 2 of the arterial time-lapse recordings (Fig. 5.7), the sprout was extending at time point 210 minutes (Fig. 5.7A). The middle panels show the contour maps for relative pressure in this region with the extending sprout labelled in black (Fig. 5.7B). At 210 minutes, the pressure difference between the vessels in the sprouting direction was positive (Fig. 5.7C). The flow pattern changed, resulting in a negative pressure difference in the direction of sprouting by 240 minutes. The sprout retracted slightly and then changed direction towards a point that resulted in a positive pressure difference (t=270 minutes, Fig. 5.7C). Sprouts did not necessarily extend along the maximum pressure difference. They would continue in the same direction as long as the pressure difference was positive but changed direction or regressed when the pressure difference was negative. As such, the pressure difference was permissive rather than instructive.

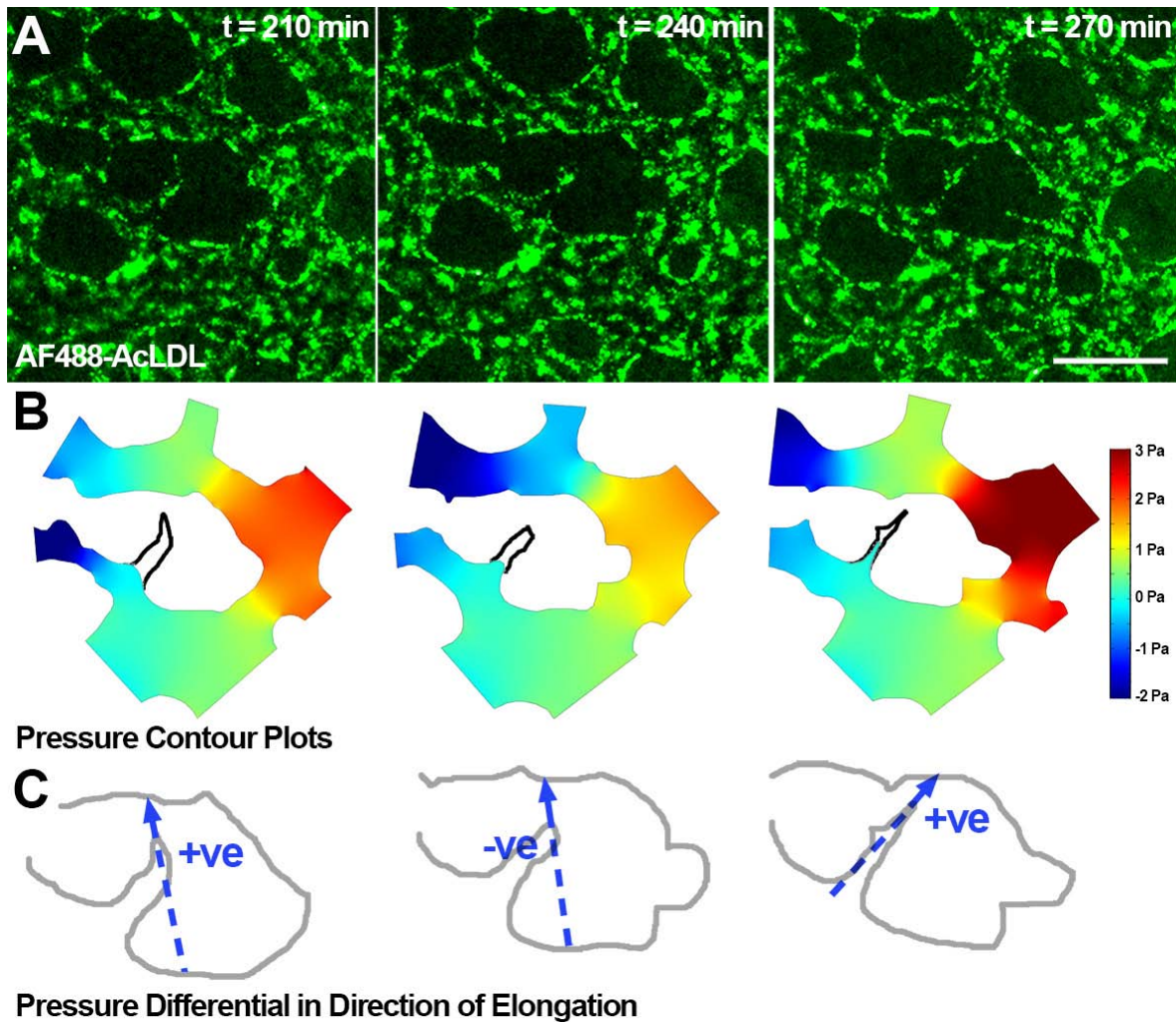


Figure 5.7– Sprouts will change direction to follow a positive pressure differential. A sprout can be observed extending and then changing direction over a period of one hour (A). Contour plots indicate changing pressure within the vessels during this time period (B, unlumenized sprout drawn in black). The sprout is initially extending in a direction of positive pressure differential. As the pressure differential becomes negative, the sprout regresses slightly (240 minutes) before beginning to extend in a new direction where the pressure differential is positive (C). Changes in sprouting direction were observed in 2 of 3 embryos analysed. Scale bar: $100 \mu\text{m}$ (A, B, C).

5.5 Discussion

We show that the flow dynamics have a significant effect on the sprouting location, the direction of sprouting and the rate of elongation. We found that sprouts only form from a vessel at low pressure towards a vessel at higher pressure, such that there is a positive pressure difference at the sprouting location. Within the lower pressure region, sprouts formed at the lowest minimum in shear stress once locations where streams merge were excluded.

Our results do not, however, show that fluid dynamics control when a sprout will form, but rather where they are likely to form. Previous *in vitro* work on sprouting and shear stress had shown that shear stress could inhibit VEGF-induced sprouting (Song and Munn, 2011). It is important to note that in that system, without the VEGF, no sprouting was observed. Similarly, in our system, fluid dynamics did not predict which avascular regions would sprout, but instead the flow predicted where along the vessel wall sprouting occurred. We did find that the sprouting avascular regions were larger on average than non-sprouting avascular regions (n=10 for each, p= 0.012, Supplementary Fig. 2A). Given the observed spread within the data (Supplementary Fig. 2B), the size of the avascular region alone cannot predict which regions will sprout. Our results suggest that the formation of a sprout within an avascular region is initiated by non-hemodynamic parameters, but that the fluid dynamic parameters define the position of that sprout.

Our results support that shear stress is inhibitory to sprouting, as we and others have found (Chouinard-Pelletier et al., 2013; Song and Munn, 2011; Tressel et al., 2007). More recently, another group published that that shear stress induced rather than inhibited sprouting (Galie et al., 2014). It is possible that both extremes are permissive to sprouting. Both low (< 10

dyn/cm²) and pathologically high shear stress (> 50 dyn/cm²) result in increased cell turnover by stimulating both apoptosis (Davies et al., 1986; Dolan et al., 2011) and proliferation (Davies et al., 1986; Metaxa et al., 2008; Sho et al., 2003). Physiological levels of shear stress, on the other hand, induce endothelial cell quiescence. Our analysis indicates that the physiological relevant signal during development is the presence of lower shear stress levels. Under pathologically high shear stress, we cannot exclude that shear stress could be pro-angiogenic.

Our previous results had indicated that shear stress only inhibited sprouting in veins but not in arteries (Chouinard-Pelletier et al., 2013). Similarly, others had found that steady shear stress inhibited sprouting in venous or capillary endothelial cell types (i.e. HUVECs and HMECs) but not in arterial endothelial cell types (BAECs) (Tressel et al., 2007). Our current results, however, indicate the opposite. Our previous results were based on an embryonic model in which we altered shear stress levels by altering the viscosity of the blood (Chouinard-Pelletier et al., 2013). Increased viscosity not only changes shear stress but would also create a more drastic pressure drop within the vascular network, such that pressure differences between vessels in the veins may be smaller. The alternative is that increasing the shear stress levels throughout the embryo resulted in an arterialization of the venous network. Though we cannot differentiate between these possibilities, it remains clear that the arterial and venous identity of the bed affects the relationship between shear stress and sprouting dynamics.

Our results also indicated that though locations where two flows merge creates points of low shear stress and large pressure differences, sprouts do not initiate from these points. We investigated the flow during the cardiac cycle to identify whether flow reversals or oscillations were present at these locations, but found that the flow remained unidirectional throughout the cardiac cycle. Whether vorticity affects endothelial cells has never been studied, but it seems

unlikely since vorticity is not a force but rather a measure of the rate of rotation of the fluid elements. The endothelium is a continuous layer connected by gap junctions and endothelial cells can sense gradients in shear stress (Dolan et al., 2011; Rouleau et al., 2010). Points where there is a change in sign in the vorticity are surrounded by shear stress vectors on either side that are in opposite directions. As such, these points do not have a zero gradient in shear stress (i.e. where the magnitude and sign of shear stress is the same on both sides of the sprouting location) and do not represent true minima in shear stress.

We find the pressure difference between vessels, and not the absolute value of the relative pressure, is proportional to elongation rate. It is unlikely that the hydrostatic pressure itself is biologically active in our model. The pressure differences that we observed in these vessels are several orders of magnitude smaller than the levels of hydrostatic pressure that have been shown to be biological active (Sato and Ohashi, 2005). The pressure difference between the vessels does, however, control the rate at which fluids exit a vessel and therefore regulates the interstitial flow patterns. Interstitial flow alone, without a VEGF gradient, can promote sprouting in an *in vitro* system (Song and Munn, 2011). Interstitial flow will modify the distribution of growth factors and metabolites in the interstitial tissue, and it was previously shown that a gradient of VEGF in the presence of interstitial flow was more effective at promoting sprouting than either alone (Song and Munn, 2011). As such, rather than sprout elongation being controlled by pressure directly, current *in vitro* evidence would indicate that the interstitial flow is the instructive parameter. We are currently developing computational models to study the distribution of angiogenic cues and the range of interstitial flow to further investigate this phenomenon.

5.6 Materials and Methods

5.6.1 Simultaneous Imaging of Vascular Remodelling and Blood Flow Dynamics

A detailed description of the methods was previously described (Ghaffari et al., 2015b). Fertilized quail eggs (*Coturnix japonica*) were incubated at 37°C and approximately 60% humidity until they reached a developmental stage of 12-14 somites or Hamburger Hamilton 11 (HH11). The embryos were injected intravascular with labelling dyes using a picospritzer III micro-injector (General Valve Corp.). AlexaFluor 488 acetylated low-density lipoprotein (AF488-AcLDL, Invitrogen) was used to label endothelial cells and PEGylated polystyrene microspheres (0.5 µm diameter red, Invitrogen, Amino-PEG, Laysan Bio) were injected to image the flow dynamics. Embryo culture for time-lapse microscopy was done as previously described (Al-Roubaie et al., 2012). Embryos were imaged on an upright fluorescence microscope equipped with an AxioCam MRC for images of the vascular morphology (AF488-AcLDL) and a high-speed camera (Photron FASTCAM Ultima APX-RS) for images of the microsphere motion. Endothelial cells were imaged with a 5x objective lens every 15 minutes. Blood flow dynamics were imaged with a 10x objective lens at 250 fps for 2 full cardiac cycles (equivalent to 2 seconds of imaging time), once every 2 hours.

5.6.2 Image Processing and Micro-Particle Image Velocimetry Analysis

The green image of the vasculature and the 500 red images of the microsphere motion were flattened into a single image to identify the walls of perfused vessels. A median filter was applied to the flattened image and then the image was thresholded to obtain a binary image used as the “image mask” (for additional details, see (Ghaffari et al., 2015b)). The image mask was

applied to each individual frame of the microsphere motion. The centreline of each vessel was found by skeletonizing the image mask. A Canny algorithm for edge detection was applied to the image mask to identify vessel walls. The local vessel diameter was obtained based on the vessel centreline and the vessel walls. Flow inlets and outlets were chosen far from branch points. μ -PIV was used to calculate velocity waveforms based on the microsphere motion during the cardiac cycle at these inlets and outlets. Since the Reynolds number for the flow is very close to one and the Womersley number is less than one (Jones et al., 2004), entrance length effects are on the order of microns and a fully developed velocity profile was assumed for the μ -PIV analysis.

5.6.3 Computational Fluid Dynamics

The vascular geometry obtained by image processing and the inlet/outlet velocities acquired by μ -PIV were imported into a computational fluid dynamic (CFD) solver. The governing equations inside the vessels (i.e. continuity and momentum equations for laminar, non-Newtonian, incompressible flow) were solved using a finite elements method (FEM) in COMSOL Multiphysics 4.4. The unsteady form of the momentum equations was used for flow inside the vessels to take into account the effects of blood flow pulsatility. The viscosity of blood was adjusted for embryonic stage, vessel diameter and shear rate as previously described (Ghaffari et al., 2015b). From N inlets and outlets, the flow rates at $N-1$ points were set as boundary conditions. For the last outlet, the fully developed boundary condition was applied at the extended outlet of the domain (depends on Reynolds number), i.e. $\frac{\partial}{\partial x} = 0$. Mesh generation and solution was performed by COMSOL. The domain was meshed with extremely fine free

triangular meshes. Two convergence criteria were used: first, a mass flux residual of less than 10^{-8} for each control volume; second, $(|\varphi_{i+1} - \varphi_i|)/|\varphi_{i+1}| \leq 10^{-10}$ for all time steps where φ represents v_x or v_y and i is the number of iteration.

5.6.4 Statistical Analysis

For formation of sprouts on the lower pressure side, a chi-squared test was used to compare the probability of sprouts always forming on one side ($n=6$) with the probability of sprouts forming randomly ($n=3$ and $n=3$, for low and high pressure side respectively). For sprout location at shear stress minima, the arc length was divided into 6 possible sprouting locations and a chi-squared test was used to evaluate the probably that sprouts would form in one location rather than randomly in all 6 locations. The value of 6 was chosen as a conservative value since it would equate approximately to $30 \mu\text{m}$ of arc length. Sprouts form within microns of predicted shear stress minima. For the relationship between pressure difference and elongation rate, we tested for co-integration using a Dickey-Fuller test and established that the relationship between the variables was stationary ($p < 0.05$).

5.7 Sources of Funding

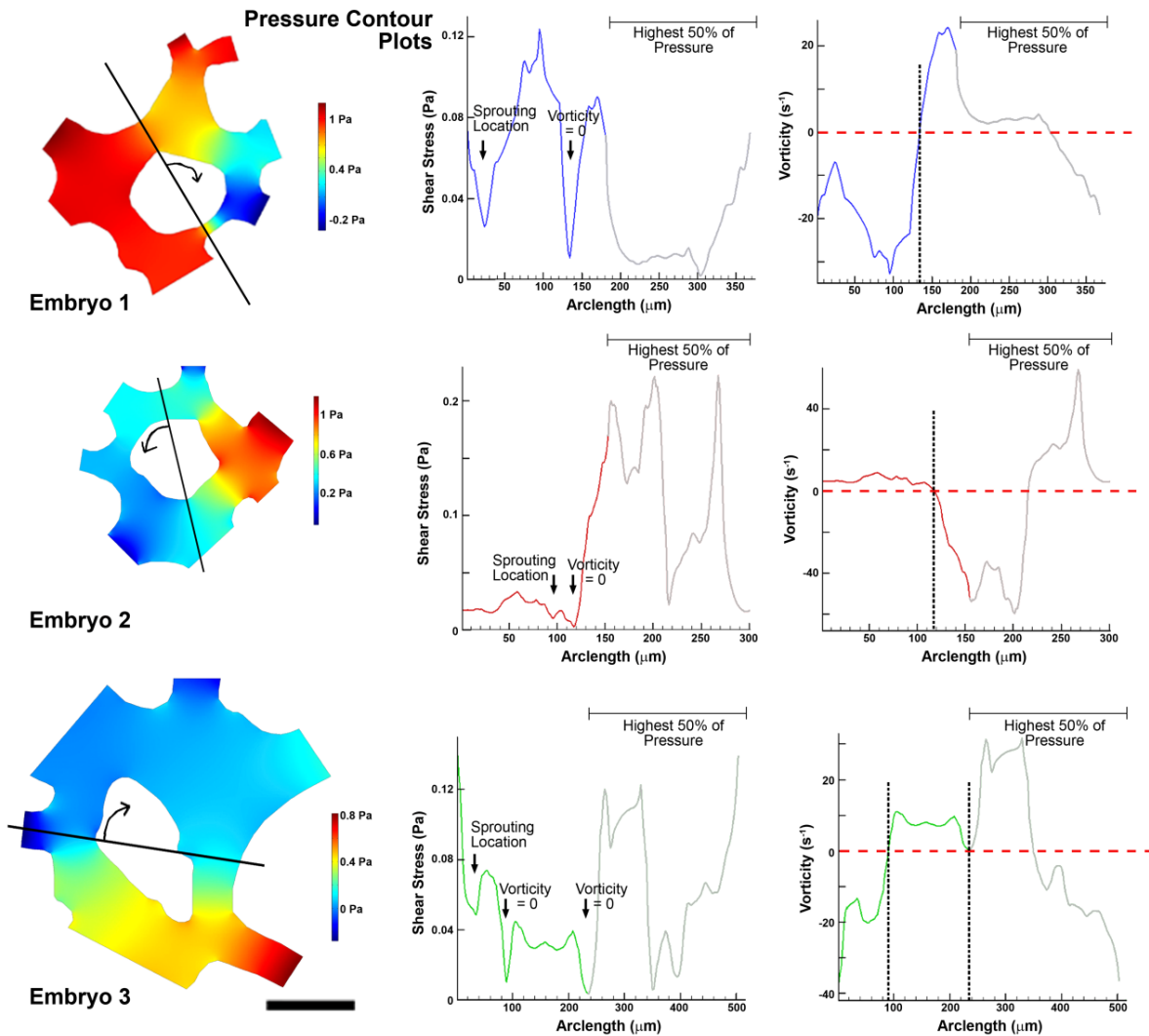
EAVJ was supported by grants from the Sick Kids Foundation of Canada (NI12-029) and a grant from Life Science Research Partners. RLL was supported a grant from the Canadian Institute of Health Research (MOP-119292). SG was supported by a McGill Engineering Doctoral Awards.

5.8 Supplementary Information

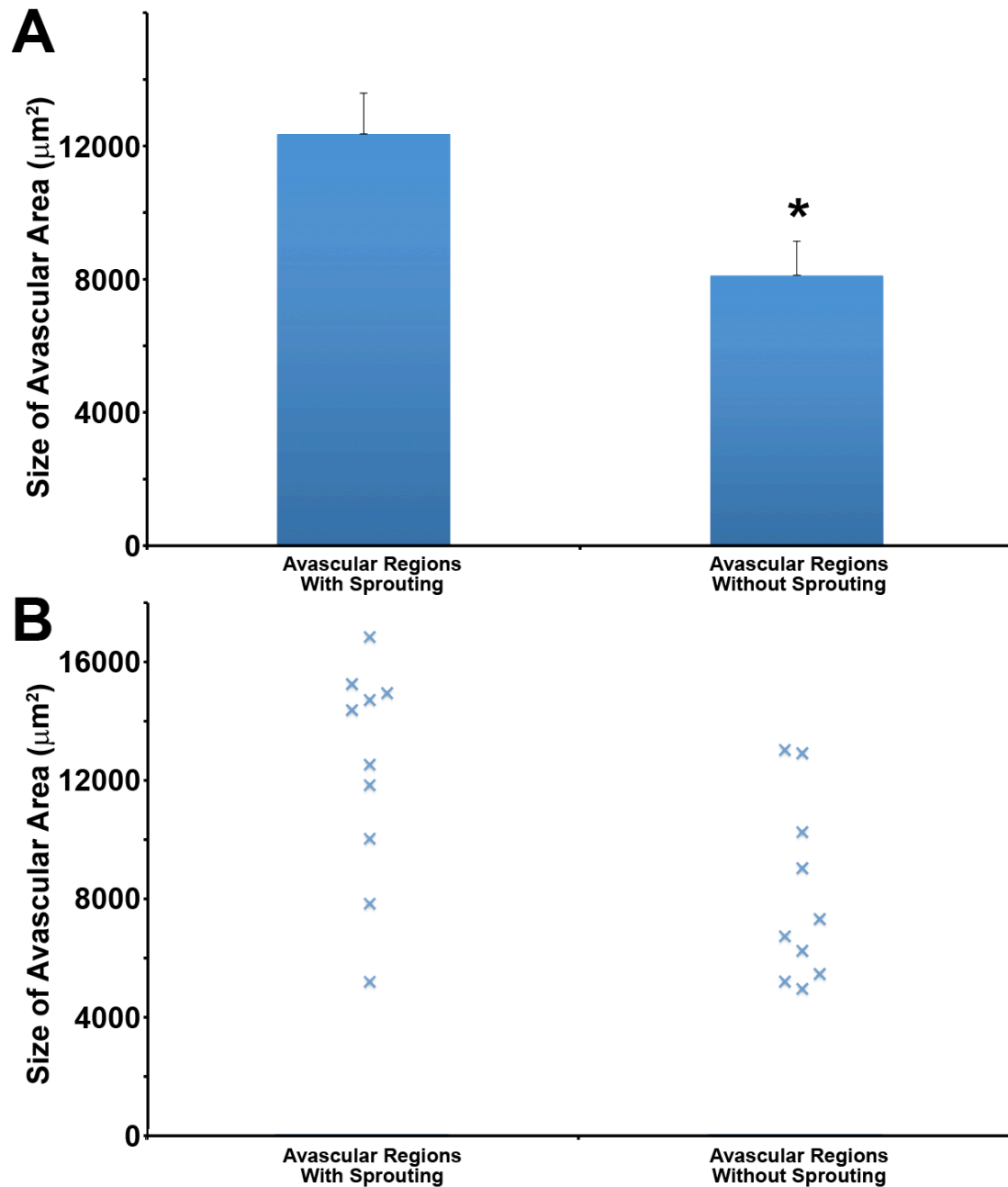
Supplementary information available online at

<http://dev.biologists.org/lookup/suppl/doi:10.1242/dev.128058/-/DC1>

Supplementary Figures



Supplemental Figure 1 – Hemodynamic data for entire arclength at the time point 30 minutes before sprout is visible. Pressure contours for each embryo are presented. Shear stress and vorticity values for the entire contour are shown, with the region at higher pressure indicated by a grey line rather than a coloured line.



Supplemental Figure 2 – Area of avascular region is larger in sprouting than non-sprouting location.

The area of avascular regions at the time of sprouting was calculated, and compared to the area of avascular regions, at the same time point, that never sprouted during the entire time-lapse recording (A).

Though sprouting avascular regions were larger than non-sprouting region ($p < 0.05$), size of the region alone cannot predict which avascular regions sprout due to the large spread of the data.

Supplementary Movie Legends

Supplemental Movie 1 – Blood velocity analysis around sprouting angiogenesis. Results of the analysis of blood velocity changes during sprouting are presented. The left panel shows the endothelial cell behaviour during the time period of analysis. The centre panel shows the velocity vectors for the blood flow during peak systole in the network. Velocity vectors are sized based on the maximum velocity at that specific time point (i.e. scale is relative). The right panel shows the absolute velocity magnitude during peak systole in these vessels during angiogenic sprouting. All scale bars represent 100 μm .

Supplemental Movie 2 – Pressure changes during sprouting angiogenesis. Results of the pressure calculations during sprouting are presented. The left panel shows the endothelial cell behaviour during the time period of analysis. The centre panel shows the relative pressure, where red represents the highest pressure at that specific time point. The right panel shows the same data, but the colour scale remains constant throughout all time points. All presented values are for peak systole however blood flow dynamics were analysed for the entire cardiac cycle at each time point. All scale bars represent 100 μm .

Supplemental Movie 3 – Shear stress and vorticity analysis around sprouting angiogenesis. Results of the shear stress and vorticity calculations at peak systole during sprouting are presented. The left panel shows the endothelial cell behaviour during the period of analysis. The centre panel shows the results for the shear stress calculations, with a constant colour scale for all time points. The right panel shows the results for the vorticity calculations, with a constant colour scale for all time points. All scale bars represent 100 μm .

6 Hemodynamics Modulate Angiogenesis in Part by Inducing Interstitial Flow that Redistributes Growth Factors

6.1 Preface

The following manuscript will be submitted to the journal *eLife*, in June 2016. In the last chapter, we studied the effect of hemodynamics in vascular remodelling, while vessel walls were assumed impermeable. The intraluminal shear stress and pressure were discussed. However, as explained in the section 3.5 interstitial flow might play a role in vascular morphogenesis. To aid this, we extended our previously developed methodology (chapter 4), to enable us to model interstitial flow through the porous matrix of the mesenchymal tissue. In this manuscript, we also modelled the transport VEGF and oxygen within the tissue to obtain VEGF distribution. This allowed us to test whether interstitial flow changed the VEGF distribution and thereby regulates angiogenesis or whether interstitial flow mediates angiogenesis using mechanical force such as transmural shear stress in cell-cell junctions.

We showed the importance of interstitial flow in the sprouting location, the direction and the rate of elongation. We found that, sprouts formed at the regions associated with higher VEGF concentration and normal gradients. The sprouting location was at the region over endothelium in which interstitial flow exits the avascular region. We also observed that sprouts elongated against the direction of interstitial flow. Moreover, a strong relationship existed between the elongation rate and interstitial flow velocity.

Hemodynamics Modulate Angiogenesis in Part by Inducing Interstitial Flow that Redistributes Growth Factors

Siavash Ghaffari^{1,2}, Richard L. Leask², Elizabeth A.V. Jones^{1,2,3*}

¹ *Lady Davis Institute for Medical Research, McGill University, 3755 Ch. Côte-Ste-Catherine, Montréal, QC, H3T 1E2, Canada.*

² *Department of Chemical Engineering, McGill University, 3610 University St., Montréal, QC, H3A 0C5, Canada*

³ *Department of Cardiovascular Science, KU Leuven, UZ Herestraat 49 - box 911, 3000 Leuven, Belgium*

To whom correspondences should be addressed: Elizabeth A.V. Jones, Centre for Molecular and Vascular Biology, KU Leuven, UZ Herestraat 49 - box 911, 3000 Leuven, Belgium, Tel. +32 16 34 75 58; Fax. +32 16 34 60 01; Email: liz.jones@med.kuleuven.be

6.2 Abstract

Blood flow is essential for vascular development in embryos. When blood flow initiates, the developing vasculature is exposed to a complete new set of stimuli, including changes in hemodynamics and biochemical signals. An important aspect of vascular development is angiogenesis. Though growth factors promote angiogenic sprouting, some additional signals are likely essential to regulate the complex process of vascular sprouting. Hemodynamics forces can stimulate the endothelium directly and have been shown to be important for regulating angiogenesis. Hemodynamics, however, also drives interstitial flow and this has been proposed to affect the sprouting process. What remains unclear is whether interstitial flow affects the distribution of growth factors or whether mechanical forces created by interstitial flow mediate angiogenesis. We recently developed a technique to analyse flow dynamics and the vascular remodelling process simultaneously in avian embryos. In this study, we extended our technique to model interstitial flow through the porous matrix of the mesenchymal tissue, and investigate both the mechanical forces that arise from these flow and how these flow affect the distribution of growth factors. We highlighted the role of interstitial flow in the sprouting location, the direction and the rate of elongation. We found that, sprouts always formed at the regions with higher VEGF concentration and normal gradients and that this was regulated by the interstitial flow. We also demonstrated that sprouts elongated in opposite direction to interstitial flow. Furthermore, a strong relationship existed between the elongation rate and interstitial flow velocity.

Keywords: Angiogenesis, Hemodynamics, Interstitial Flow, VEGF gradient

6.3 Introduction

Angiogenesis is the formation of new blood vessels from pre-existing ones in response to angiogenic stimuli. The key steps in angiogenesis include endothelial cell proliferation and migration. Angiogenesis is necessary in many physiological and pathological conditions, such as embryonic development, wound healing, tissue regeneration, and tumor growth. A fundamental insight into angiogenesis and the physiological cues that control the process is necessary to improve the treatment of stroke, ischemia, AMD and cancer. During embryonic development, blood flow is crucial for vascular remodelling and induces both mechanical signals, such as shear stress, and chemical signals, such as oxygen and nutrient delivery, which are essential for normal vascular development (Jones, 2011a).

Vascular endothelial growth factor (VEGF) helps regulate endothelial cell function. It is a strong angiogenic mediator that controls several of the key steps of angiogenesis including endothelial cell proliferation and migration (Dvorak et al., 1995; Ferrara et al., 2003; Olsson et al., 2006). Endothelial cell migration is directionally regulated by chemical stimulus (Lamallice et al., 2007). VEGF controls angiogenic sprouting by causing the formation of filopodia from tip cells that sense growth factors. VEGF gradients guide these filopodia, triggering migration of the tip cell toward the concentration gradient (Gerhardt et al., 2003; Ruhrberg et al., 2002). Moreover, stalk cells respond to the local concentration of VEGF by proliferation (Gerhardt et al., 2003). VEGF₁₂₁ and VEGF₁₆₅ are the most frequent and active isoforms (Ng et al., 2001). However, only VEGF₁₆₅ binds to the heparan sulfate proteoglycans (HSPG) present in the extracellular matrix (Ferrara, 2004). The VEGF distribution can be mediated by proteases such as the matrix metalloproteinases (MMPs), which can cleave VEGF from HSPG (Lee et al., 2005). Tissue growth creates regions of hypoxia which is one of the strongest stimulus for

angiogenesis. It stimulates VEGF upregulation, as a result of change in the level of hypoxia inducible factor (HIF-1 α) (Tang et al., 2004).

Blood flow exerts a tangential force on the luminal surface of endothelium which is called shear stress. Luminal shear stress is a biomechanical signal that is sensed by endothelial cells, and has been shown to induce changes in gene expression (Lucitti et al., 2007). Fluid shear stress modulates endothelial cell migration (Lamallice et al., 2007), and controls endothelial cells proliferation (Lin et al., 2000). Moreover, interstitial flow exiting or entering the vessel walls creates physical forces across the endothelium. Interstitial flow transverse to the endothelial monolayer (transmural flow) induces endothelial cell sprouting (Hernández Vera et al., 2008). The mechanism of mechanotransduction involved in the process is unclear, however transmural flow has been shown to activate a response that leads to increased strength of cell-cell junctions in the endothelial monolayer (Tarbell et al., 1999). As such, the role of interstitial flow is more than just cell nourishment. It can potentiate the effects of VEGF and induce blood vessel morphogenesis in cells scattered in a 3D matrix by activating membrane bound sensors in endothelial cells (Helm et al., 2005). The number of filopodia created during sprout increases when sprouts elongate against interstitial flow, and the presence or absence of VEGF gradient did not change the number of filopodia (Song and Munn, 2011). The authors suggested that tip cells extend filopodia to probe the interstitial flow environment, in addition to responding to VEGF gradients. These results highlight the importance of signals from interstitial flow.

The difficulty in quantifying shear stress levels *in vivo* and in real time have limited our ability to understand the role of hemodynamics signals. We recently developed a method to measure flow dynamics and the remodelling vasculature simultaneously (Ghaffari et al., 2015b) and applied this technique to investigate how hemodynamic signals control sprout initiation and

elongation in avian embryos (Ghaffari et al., 2015a). Our previous work looked only at fluid dynamic parameters on the luminal side of endothelial cells and did not investigate the interaction of luminal and transmural shear stress, interstitial flow, and VEGF distribution in the process of angiogenesis. To this end, we extended our previous technique and assumed permeable vessel walls. This allowed us to model interstitial flow through the porous matrix of the mesenchymal tissue, and analyse how these flow affect VEGF and oxygen transport in the tissue. Our results emphasize the importance of interstitial flow in angiogenic sprouting, and show how hemodynamic signals and VEGF distribution combine to control sprout initiation and direct elongation. One group recently developed microfluidic device that enabled them to adjust shear stress and interstitial flow *in vitro* as endothelial cells sprout (Song and Munn, 2011). Our results support their results that showed that interstitial flow enhances angiogenesis, and luminal shear stress inhibits sprouting. However, a better understanding of the hemodynamic environment present *in vivo* during angiogenesis is required to understand the causal stimuli.

6.4 Results

To investigate the interplay of luminal shear stress, transmural shear stress, interstitial flow, and VEGF distribution in the process of angiogenesis, we used our previously developed technique (Ghaffari et al., 2015b) to simultaneously capture vessel morphology and flow dynamics by time-lapse microscopy and expanded the method to predict interstitial flow patterns. We included computational simulations of VEGF production and investigated how these interstitial flow patterns affects VEGF transport. Images of morphology (Fig. 6.1A), obtained by injection of Alexa Fluor 488-labelled acetylated low-density lipoprotein (AF488-

AcLDL) were processed to determine the geometry and vessel walls. The vessel walls were assumed rigid and permeable. As a result, mesenchymal tissue and endothelial monolayer were assumed to be porous matrices. Electronic microscopic images were used to obtain permeability and porosity of these two layers of tissue (see extended online methods). The motion of the injected red fluorescent microspheres (Fig. 6.1A) was analysed using micro-particle image velocimetry (μ PIV) to calculate the velocity of the blood flow at the inlet and outlet vessels of the region of interest. These measurements were then input into a computational fluid dynamics solver to solve coupled Navier-Stokes and Brinkman-Darcy equations for the entire domain (Fig. 6.1B). This allowed us to solve for interstitial flow velocities. Blood flow inside the vessels and interstitial flow thorough the mesenchyme, were obtained once every 30 minutes. Furthermore, we also solved for transmural shear stress based on the interstitial flow rates and cell junction geometry, assuming fully developed laminar flow in these junctions. VEGF secretion rate is dependent on oxygen partial pressure (P_{O_2}) of tissue. Therefore, P_{O_2} distribution in the tissue area was obtained by modelling the oxygen transport and its consumption rate by the mesenchymal cells (Fig. 6.1C, see extended online methods). The oxygen tension level at vessel/tissue boundary was assumed to be 40 mmHg. VEGF secretion was made proportional to P_{O_2} distribution. To find VEGF distribution in the avascular area, we modelled different VEGF isoforms and including transport of the VEGF both by diffusion and advection (i.e. transport with the bulk interstitial fluid motion). The kinetics of binding of VEGF₁₆₅ to HSPGs in ECM and cleave by MMP into VEGF₁₁₄, were included in the model (Fig. 1D). Furthermore, we modelled binding of VEGF to receptors at the endothelial cell surface.

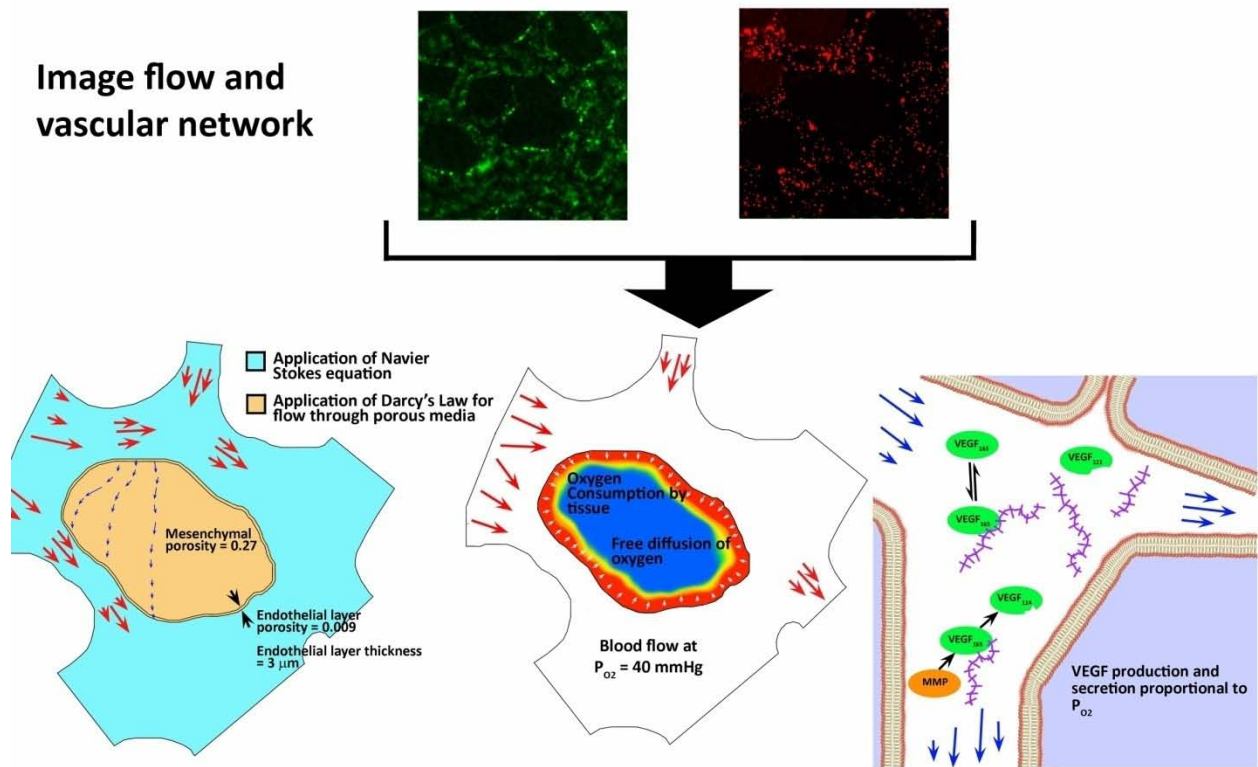


Figure 6.1– Description of data acquisition and computer modelling. Images of the vascular network were acquired every 15 minutes, and high-speed images of microsphere motion were acquired every 2 hours. The vascular morphology and inlet/outlet blood velocities were input into COMSOL. Avascular regions were assumed to be porous, and flow in the region were calculated based on Darcy’s Law. Porosities for the endothelial cell layer and the mesenchymal region were calculated based on TEM and SEM images, respectively (see online supplemental methods). Oxygen distribution was modelled assuming free diffusion of oxygen into the tissue, with blood plasma having a constant oxygen partial pressure of 40 mmHg, and oxygen consumption based on previous data for avian embryos at this stage of development (Burggren et al., 2000). Production of VEGF₁₆₅ and VEGF₁₂₁ was proportional to hypoxia, and modelling of VEGF distribution included both advection (i.e. movement with the bulk fluid motion) and diffusion. Matrix-binding and release by MMP of VEGF₁₆₅ was included in the analysis.

To validate the calculated velocity field, we compared the computed results to the measured values from the μ PIV. For a vascular network with N inlets and outlets, $N-1$ were used to define the flow for the computational analysis. The calculated velocity at the last outlet was then compared with the experimental μ -PIV result. We performed the error analysis for the total number of 7 embryos based on the percentage of difference between calculated and μ -PIV result. The error increased significantly as the time-lapse experiment proceeded, due to reduction in the number of microspheres in circulation (Ghaffari et al., 2015b). For all embryos and all time points, errors were less than 10%. We compared the percentage error when the vessel walls were assumed impermeable to results when the avascular area was assumed to be a porous media. In the porous media assumption, we compared the calculated permeability of mesenchymal tissue ($5.2 \times 10^{-14} \text{m}^2$) with values of one order of magnitude lower and higher (Supplemental Fig. 1). Considering the avascular area as porous media reduced the error by 0.5% at the beginning of experiments and by 2% after 600 minutes. The error was lowest with our calculated value for permeability. Though our porous network properties gave the lowest error, the reduction in error due to the porous assumption is modest because most of the error arises from the μ -PIV measurements themselves. To validate the interstitial flow rates, we investigated whether the model could predict observed interstitial transport *in vivo*. We previously injected quail embryos at different stages with FITC-40K neutral dextran (Henderson-Toth et al., 2012). At 16 somites, the time required for the dextran to leach out from vessels was approximately 6 h. Based on our calculated values for interstitial flow, the required time for a particle to travel the distance of avascular diameter (based on average diameter at that stage), would be approximately 5.5 h. Thus, the calculated interstitial velocities are in good agreement with our previous works (Henderson-Toth et al., 2012).

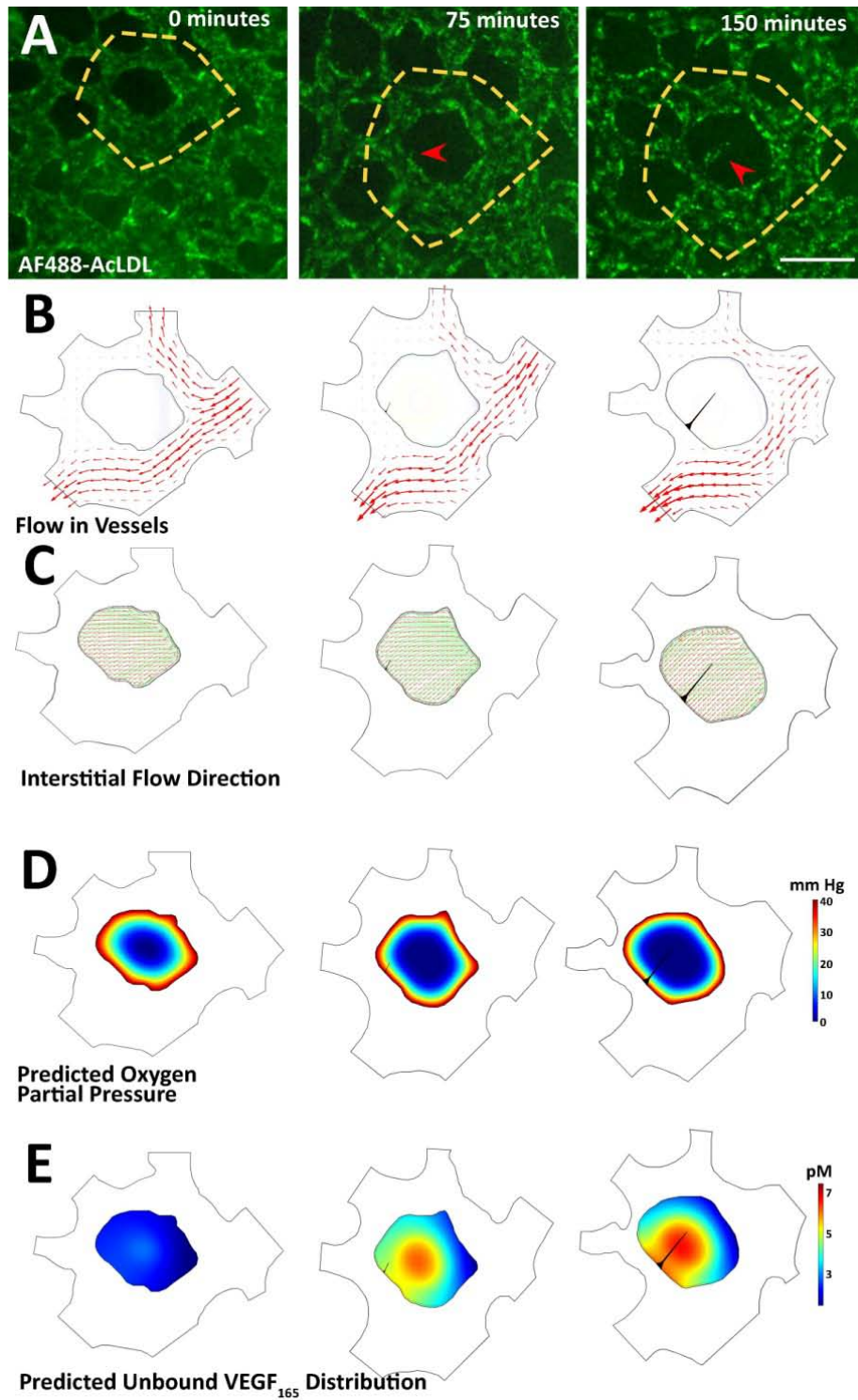


Figure 6.2– Time-lapse analysis of fluid dynamic parameters in the presence of interstitial flow. All time-lapse movies started with embryos at 12-14 somites (or Hamburger Hamilton Stage 11). The arterial region of the vasculature was imaged for a total of 12-16 hours (A, Supplemental Movie 1). The flow

dynamics over the entire time-lapse period were analysed for a total of 3 embryos, with an additional 6 embryos analysed at the time of sprouting. Blood flow velocity and pattern was determined for the entire cardiac cycle however only values for peak systole are presented (B). By assuming a porous matrix within avascular regions, the interstitial flow patterns were analysed (C). Oxygen diffusion and consumption models were used to predict oxygen partial pressure in the tissue (D). VEGF production was proportional to the level of hypoxia, and the redistribution of unbound VEGF₁₆₅ due to interstitial flow was analysed (E). Scale bar; 100 μ m. All images are at the same scale.

Having validated our interstitial flow patterns, we next analysed the effect of the flow on the expected VEGF distribution during sprouting in the arterial plexus of 7 quail embryos. We analysed interstitial flow patterns and VEGF distribution starting 60-90 min before the sprout became visible (Fig. 6.2A, red arrowheads) and continued until the vessel lumenization. The full time-lapse movie is available as Supplemental Movie 1. In the region of interest, the computational solver calculates blood velocity in the vessels (Fig. 6.2B) and interstitial velocity through the porous matrix in the tissue (Fig. 6.2C). The VEGF distribution was then calculated based on the velocity field in the tissue and oxygen partial pressure distribution using the computational solver (Fig. 6.2D-E). The velocity field, oxygen partial pressure, and VEGF distribution were obtained every 30 minutes (Supplemental Movie 1). The left panel of the supplemental movie shows changes in the vessel morphology which were measured every 15 minutes.

To investigate the effect of interstitial flow on the distribution of growth factors, we compared the VEGF distribution in the presence of convective and diffusive transport (i.e. with

interstitial flow), with the distribution that is expected when only diffusive transport is present (i.e. no interstitial flow). The free VEGF₁₆₅ concentration with or without interstitial flow (Fig. 6.3A-B) and VEGF₁₆₅ spatial normal gradient are shown (Fig. 6.3C). The results for three different embryos are available in Supplemental Figure 2. Interstitial flow causes significant changes in VEGF and its normal gradient distribution. Without interstitial flow, the VEGF concentration is fairly uniform on the endothelial cells, whereas interstitial flow divides the distribution over endothelium arc length into regions of higher and lower VEGF concentrations (Fig. 6.3B). Furthermore, interstitial flow increases the normal VEGF gradient significantly, making it steeper (Fig. 6.3C).

The cleavage of VEGF₁₆₅ by MMP into VEGF₁₁₄, was also considered in our model. The free VEGF₁₆₅ concentration (Fig. 6.3A, B) and VEGF₁₆₅ spatial normal gradient are shown (Fig. 6.3A, C), with or without MMP modelling. The cleavage modelling did not significantly change the VEGF distribution nor the gradient of VEGF normal to the endothelial cell surface significantly. It resulted in a difference of less than 5% change in VEGF concentrations for all embryos at the time of sprouting initiation, but did not vary the pattern of the VEGF distribution, just the absolute value.

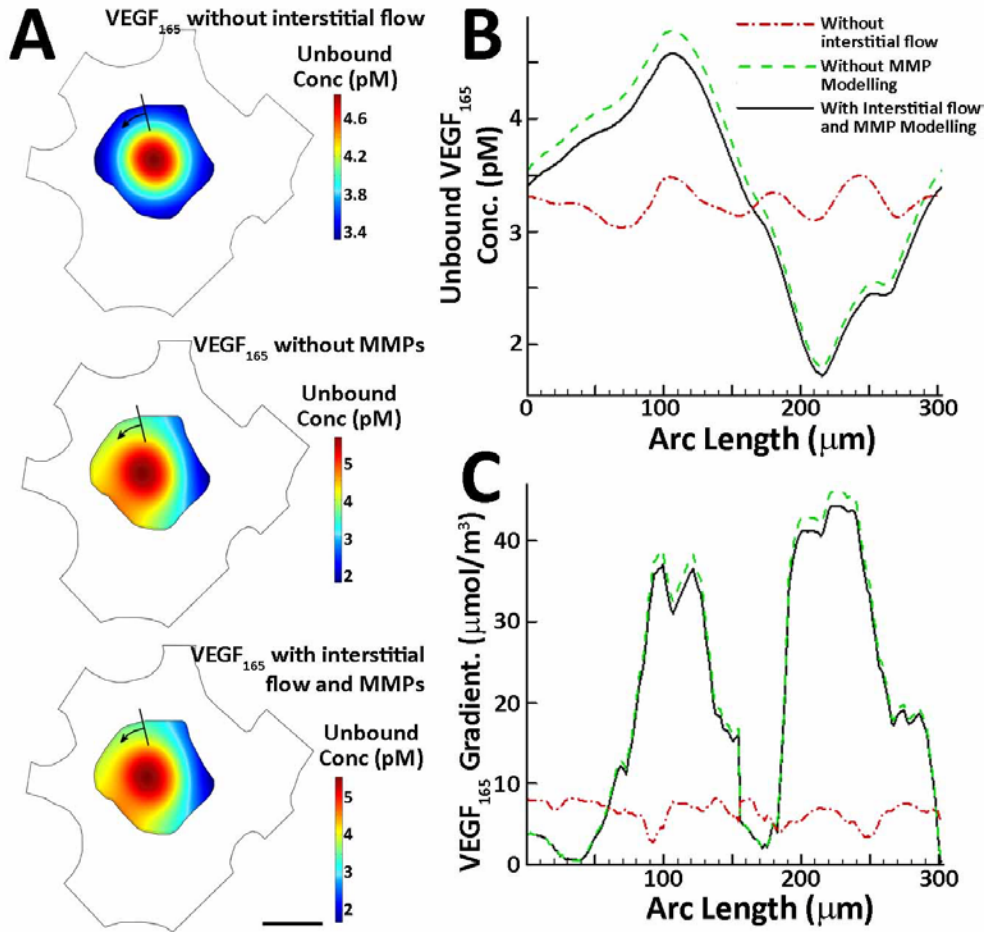


Figure 6.3– The presence of interstitial flow significantly affects the VEGF distribution. Analysis of unbound VEGF in the mesenchymal region when interstitial flow and MMP-mediated release from the matrix are absent, when only interstitial flow is considered, when both interstitial flow and MMP-mediated release from the matrix are considered (A). The concentration along the endothelial circumference show that both unbound $VEGF_{165}$ concentration (B) and gradient (C) are significantly altered when interstitial flow is considered. In the absence of interstitial flow (red dotted line), the concentration and gradient along the endothelium are relatively constant. The presence of interstitial flow (green dotted line) induces a significant shift such that regions of high and low VEGF are present. The addition of matrix release by MMPs only slightly alters the distribution of these parameters (black solid line). Data for one embryo is shown. The data for three embryos, with and without interstitial flow, is presented in Supplemental Figure 2. Scale bar; 50 μm (A).

The different isoforms of VEGF are believed to have differential distribution patterns because of differences in diffusion and in matrix binding. In the presence of advection, however, the role of diffusion is diminished. We therefore investigated the VEGF concentration on the endothelium when sprouting initiated (i.e. 30 min prior to sprout appearance, Fig. 6.4) for each of the isoforms of VEGF that were included in our model. The contour plot of total VEGF isoforms concentration (the sum of bound and unbound VEGF₁₆₅, VEGF₁₂₁, and VEGF₁₁₄) just prior to sprouting is shown in Fig. 6.4A, whereas Fig. 6.4B shows the VEGF concentration bound to receptors with respect to distance along the endothelium. The black lines and arrows in Fig. 6.4A indicate the arc length represented in the x-axis of Fig. 6.4B-C (x=0 at the bottom of the arrow). Fig. 6.4C shows the free VEGF₁₆₅, VEGF₁₆₅ bound to HSPG, VEGF₁₂₁, and VEGF₁₁₄ concentrations along the arc length of endothelial monolayer. The surface concentrations of the various isoforms bound to receptors follow a similar pattern, but differ in magnitude. The concentration of VEGF₁₆₅ bound to VEGFR2 is significantly higher than other VEGF isoforms bound to receptors (Fig. 6.4B). With respect to free VEGF isoforms in the tissue and HSPG-bound VEGF, a similar results was found. The patterns of distributions are similar, however they are different in magnitude. Of the total VEGF in the tissue (with the exception of VEGF bound to receptors on the endothelial cell surface), we find that 4 times more is bound to HSPG and than exists as free VEGF (84% versus 18%). Of the unbound VEGF, 81% is VEGF₁₆₅, 13% is VEGF₁₁₄, and the other 6% is VEGF₁₂₁. The patterns of VEGF concentrations are the same along the endothelium, and the relative magnitudes rather than the absolute values are of importance to our study. Therefore, we limited our analysis to the distribution of unbound VEGF₁₆₅ concentration, and refer to it as VEGF concentration.

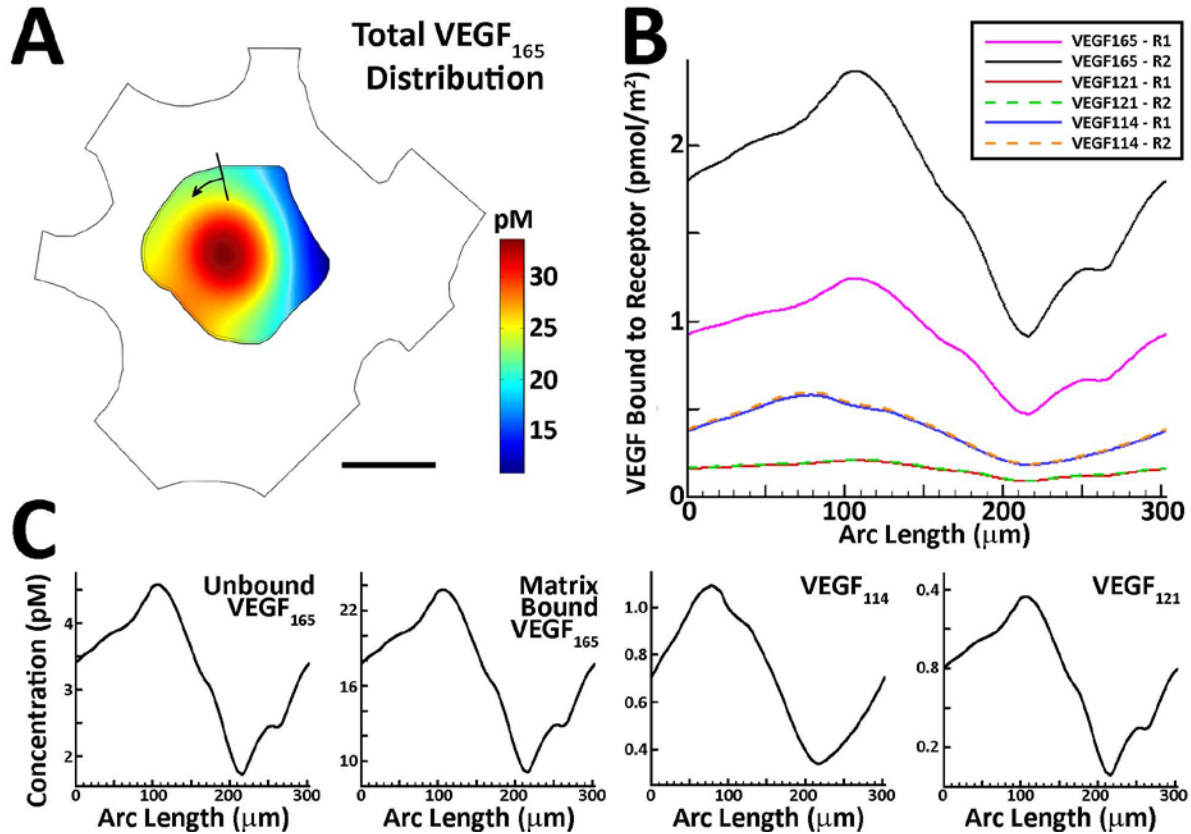


Figure 6.4– In the presence of interstitial flow, all isoforms of VEGF redistribute with the same pattern. Total VEGF₁₆₅, including matrix-bound and unbound, for the avascular regions is shown (A). The black line and arrow indicate the starting point for the axis in all other panels. The endothelium was assumed to express both VEGFR1 and VEGFR2, though at different concentrations. The analysis of binding of each isoform of VEGF to the different receptors show that the majority of VEGF signalling occurs through binding of VEGF₁₆₅ to VEGFR2 (B). The pattern of binding, however, does not differ much between the isoforms, with the peak and minimums located at with 30 μm of each other, for all combinations. Analysis of each unbound isoform of VEGF at the endothelial cell layer (C), further confirms that the relative patterns are similar, but only the actual values of the concentrations differ for each isoform, when interstitial flow is present. Data for one embryo is shown, however similar results were obtained for all embryos analysed. Scale bar; 50 μm (A).

We previously showed that sprout location can be predicted based on flow dynamics (Ghaffari et al., 2015a). In this study, our objective was to investigate the interplay of flow dynamics signals and VEGF distribution on angiogenesis. We analysed unbound VEGF₁₆₅ distribution prior to sprouting in 7 embryos (Fig. 6.5). VEGF concentrations (Fig. 6.5A-C) and VEGF normal spatial gradient concentrations (Fig. 6.5D-F) along the endothelium are shown for 3 embryos. In this figure, the dark blue dashed line shows shear stress minima where sprouting occurs, whereas the light blue lines depict local minima of luminal shear with zero vorticity, and pink lines depict local minima without sprouting. Vorticity is the angular velocity of a fluid, and we previously showed that the sprouting avoids a point where vorticity is zero and flow merges (Ghaffari et al., 2015a). The full hemodynamic analysis of each of these three embryos at the time of sprouting is shown in Supplemental Figure 3. We found that for all time-lapse experiments, the location of sprouting was accompanied by high values of VEGF concentration and high gradient of VEGF normal to the endothelium. Though levels and gradients were high, sprouting did not occur necessarily at absolute maxima of VEGF concentration nor of its gradient. Our previous results had indicated that sprouts in the arterial plexus formed at a local minimum in shear stress (Ghaffari et al., 2015a). If points with zero vorticity are excluded from all shear stress minima, then sprouts formed at the shear stress minimum with the highest concentration of VEGF and the largest normal gradient of VEGF. As an example, in one of the analysed embryos (Embryo 1), four local minima of luminal shear stress were present (Supplemental Fig. 3). Two of them ($x=118\ \mu\text{m}$ and $x=217\ \mu\text{m}$) were points where flow merges (vorticity at those point was zero). Among two remained minima ($x=95.6\ \mu\text{m}$ and $x=170\ \mu\text{m}$), the sprout forms at the point ($x=95.6\ \mu\text{m}$) which had the higher VEGF concentration and gradient.

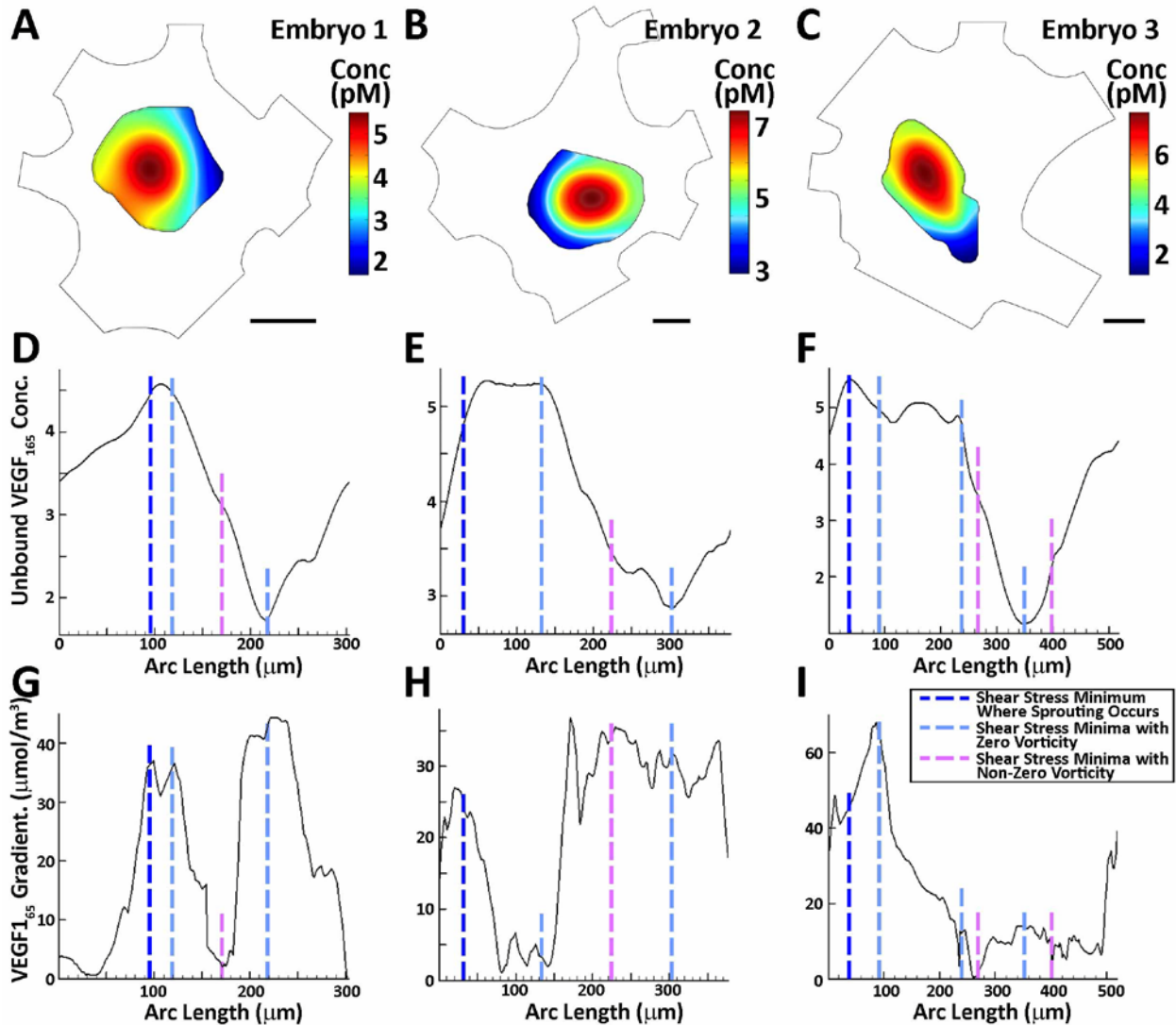


Figure 6.5– Sprouts form at the shear stress minimum with the highest VEGF concentration. Analysis of unbound VEGF₁₆₅ for three embryos, in the presence of interstitial flow is presented (A-C). For each embryo, the black line and arrow indicates the start of the arc length measurements presented in the lower panels. Our previous results showed that sprouting location could be predicted based on three fluid dynamic criteria; low pressure half of the avascular region, shear stress minimum, but excluding locations where streams merge. When considering VEGF redistribution in the presence of interstitial flow, sprouts did not form at the maximum VEGF₁₆₅ concentration (D-F) or maximum VEGF₁₆₅ gradient (G-I), but rather formed at the shear stress minimum with the highest VEGF concentration, once location

where streams merge (and therefore vorticity is zero) are excluded. Sprouting locations are indicated by dark blue lines. Shear stress minimums with zero vorticity are indicated with light blue lines. All other shear stress minimums are indicated with pink lines. Full hemodynamic analysis for these embryos is available in Supplemental Figure 3. Scale bar; 50 μm (A-C).

In addition to luminal shear stress over the endothelium, transmural shear stress through the endothelium has been suggested to induce sprouting of endothelial cells (Galie et al., 2014). We therefore calculated transmural shear stress along the arc length of endothelial monolayer for 3 analysed embryos (Fig. 6.6). We find that the level of transmural shear stress is an order of magnitude lower than the level of luminal shear stress. We defined the transmural shear stress as positive when flow exits into the avascular region from vessels, and as negative when it enters the tissue. Although the sprout formed at a local minimum of transmural shear stress in one embryo (Fig. 6.6, Embryo 2), in the others, no specific pattern in transmural shear stress was present (Fig. 6.6, Embryo 1-3). Thus, no general conclusion can be made. However, sprouts always formed where transmural shear stress is positive, i.e. flow exits the avascular region into vessels.

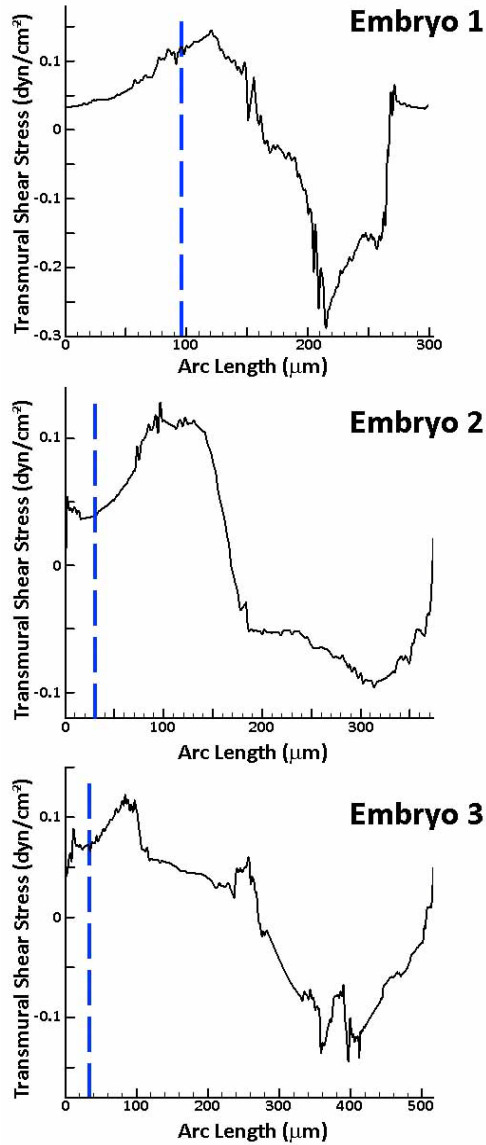


Figure 6.6– Sprouts form in regions with positive transmural shear stress, but not necessarily at maximums or minimums. The transmural shear stress was calculated based on the flow rate through the endothelium and the void fraction of the surface that represents intercellular junctions. Sprouting locations are indicated with dark blue lines. The starting point of the arc length measurements is the same as for Figure 6.5. Though transmural shear stress was always positive at sprouting location, indicating that the direction of transmural flow goes from the avascular region towards the vessel lumen, sprouting was not specifically associated with maximums or minimums in transmural shear stress levels.

Our previous work had also shown that elongation was proportional to the pressure drop across the avascular region. In that work, we had suggested that this was due to the interstitial flow rather than the pressure itself. We therefore investigated the effects of the flow dynamics on the VEGF distribution in the time-lapse experiments (Fig. 6.7, Supplemental Figure 4). We calculated the average VEGF concentration over the length of the sprout, the concentration at the base of the sprout, and at tip, starting 60-90 minutes before sprout initiation until final lumenization (Fig. 6.7A). A threshold in VEGF concentration was present for sprout initiation for all embryos. At the time of sprout initiation, the unbound VEGF₁₆₅ concentration was between 4.5 pM and 5.4 pM for all embryos (n=7, average=5 pM , SD=0.4), indicating a possible threshold for VEGF in sprout initiation. Once sprouts had formed, however, VEGF concentrations did not necessarily remain at this level, and either increased or decreased. VEGF gradient along the sprout elongation (the difference in VEGF concentration between the tip and the base) and VEGF gradient normal to the sprout tip were studied during elongation (Fig. 6.7B). The gradients increased at early time points, however, as soon as the sprout passed the maximum VEGF at the center of avascular area, the gradient at the tip became negative and the gradient along the sprout either decreased or remained constant. Interstitial flow through the porous matrix of ECM exerted shear stress over the endothelial cells of sprout elongation. Shear stress on tip cells of the sprout elongation was calculated over time (Fig. 6.7C). We defined shear stress as positive when the sprout elongates in the direction opposite to interstitial flow. The interstitial shear stress levels were approximately 1000 fold lower than luminal shear stress levels, and 100 fold lower than transmural shear stress levels. We next calculated the elongation rate of the sprouts based on displacement of the tip of the sprout between two frames (Supplemental Fig. 4) and compared this to changes in abovementioned parameters. We plotted the elongation rate with

respect to VEGF concentration (Fig. 6.7D), VEGF gradient (Fig. 6.7E) and shear stress over the sprout elongation (Fig. 6.7F) for all 3 embryos. Negative elongation rates correspond to sprout regression. Among all three plots, elongation rate correlated well with both VEGF gradient and shear stress, however the relationship between the gradient and elongation was the opposite of experimental observations, such that increasing the VEGF gradient would actually reduce the elongation rate. We found a logarithmic relationship between the elongation rate and shear stress over the sprout elongation (Fig. 6.7F, $r^2=0.7$). The level of shear stress over the sprout elongation is directly proportional to interstitial flow velocity at the tip cell of sprout elongation. Therefore, a significant association between the rate of elongation and interstitial flow is present.

To test which signals affect the direction of sprout elongation, we studied sprout angle variations in time-lapse experiments (Fig. 6.8). We calculated angle between the base of the sprout and the maximum VEGF concentration in the tissue and the angle between the direction of sprout elongation and the direction of flow (Fig. 6.8A). We plotted these angles over time for all three embryos (Fig. 6.8B). Except at early time points, it was observed that the angle between flow and the sprout elongation was closer to zero than the angle between elongation and maximum VEGF location. Thus, the sprout elongated against the direction of interstitial flow. Due to heterogeneity in extracellular matrix structure and tortuosity of porous matrix, real sprout direction deviated to a small extent from the direction of interstitial flow.

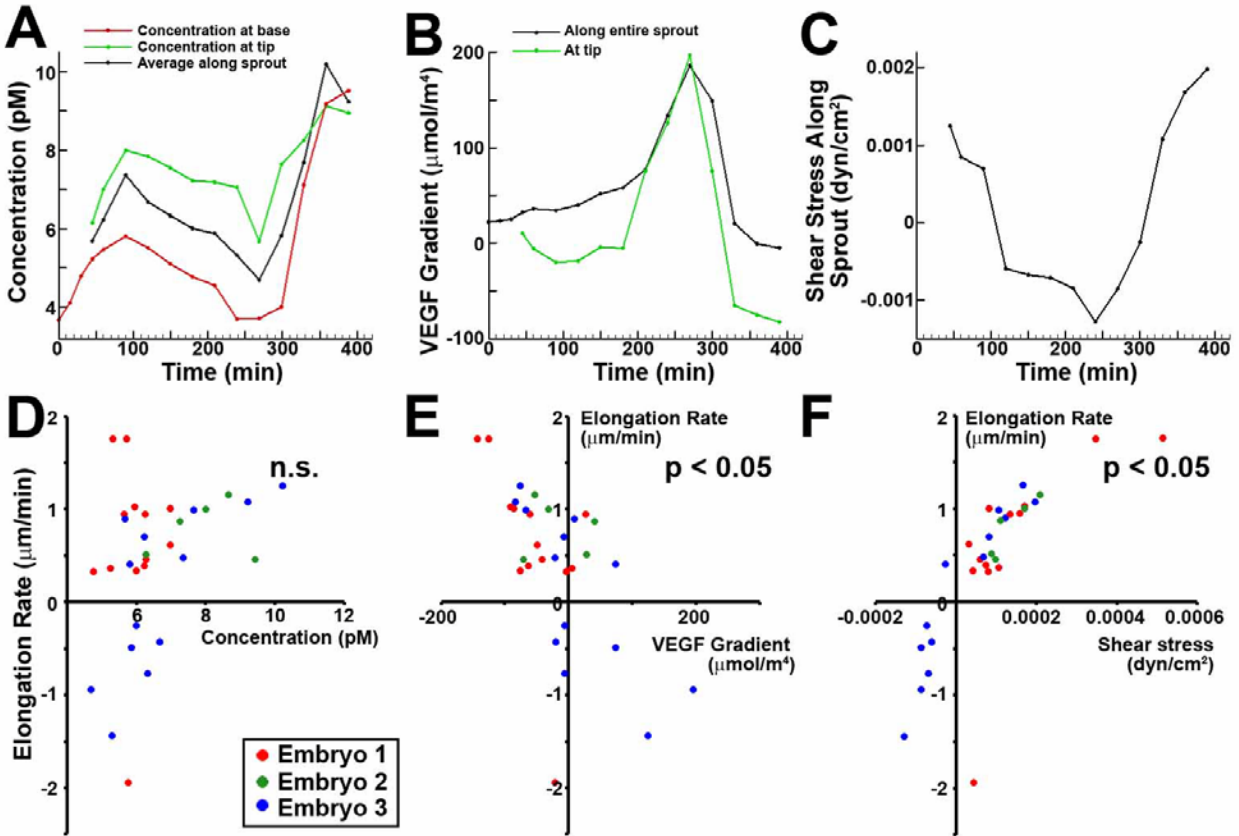


Figure 6.7– Elongation rates do not correlate with VEGF concentration or gradient, but rather flow dynamics along the sprout. The concentration of VEGF along the tip, at the tip and at the base of the sprout were followed during sprout elongation (A). The gradient of VEGF at the tip, or along the sprout was also analysed (B). Furthermore, flow dynamics, and specifically shear stress, were following as sprouts elongated (C). Of these parameters, none of the concentrations that were analysed correlated with elongation (D, average concentration on entire sprout shown). Elongation rate did correlate with VEGFR gradient at the tip, however the correlation is opposite to expected from the biological behaviour, such that increased gradients would reduce elongation rates (E). Shear stress along the sprout, on the other hand, correlated very strongly with elongation rate (F). Calculated shear stress levels are below known threshold for biological activity. The interstitial velocity correlated as well as shear stress, indicating the possibility that dissolved components carried by the flow either from the endothelium or from the lumen could control elongation rates.

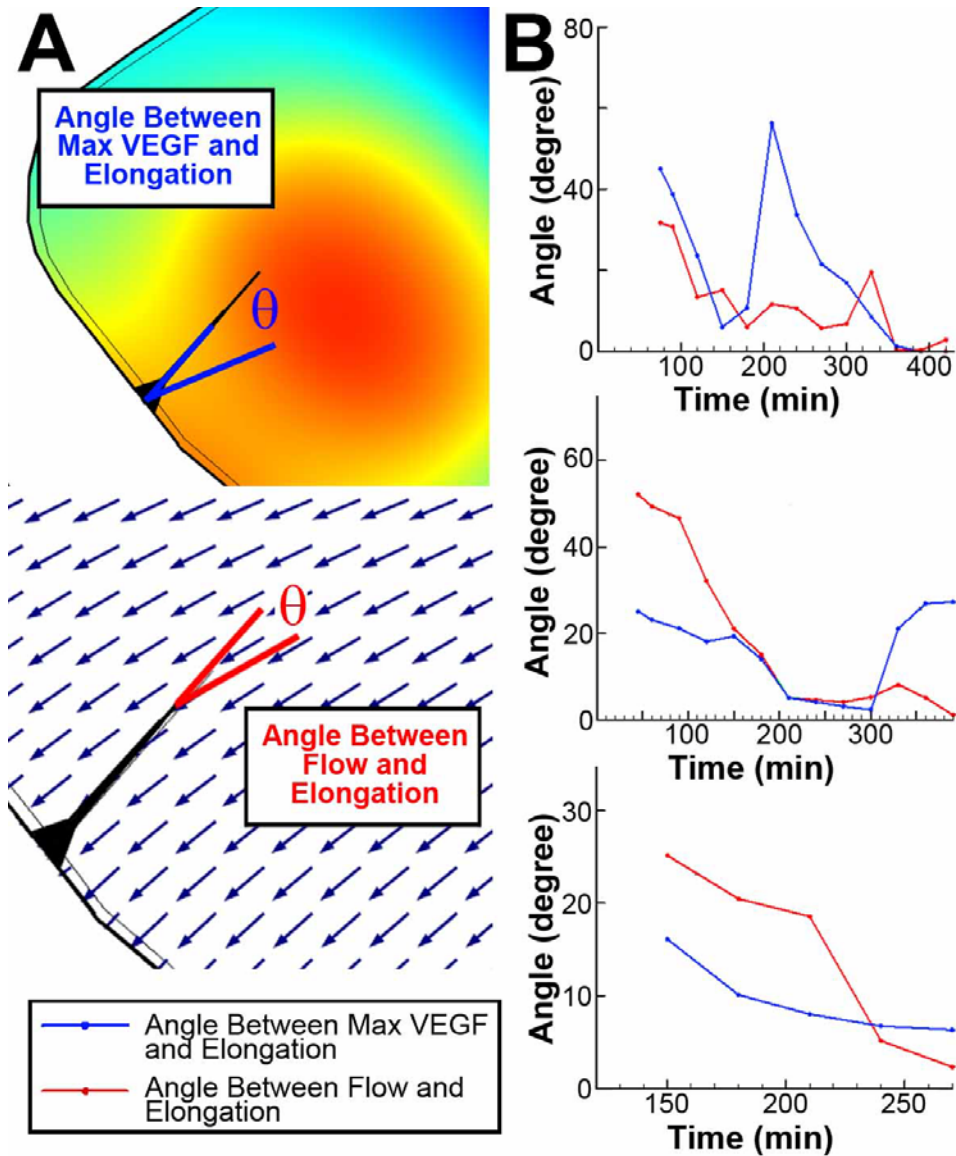


Figure 6.8– The direction of elongation follows the direction of flow after the VEGF maximum has been passed. The two angles of elongation analysed, the one between the direction of elongation and the location of maximum VEGF as well as the angle between elongation and the direction of interstitial flow, are shown (A). At early time point, the direction of elongation is neither towards maximum VEGF nor the the direction of flow, though the angle with respect to maximum VEGF concentration is often smaller than that with respect to flow direction. At later time point, sprouts follow the flow directions and the difference in the elongation direction and the flow direction is small (B). Panels in B represent 3 different embryos.

6.5 Discussion

The role of blood flow during development is not only to deliver oxygen and nourishment to the growing tissues, but also to induce mechanical and chemical signals required for proper development. Though fluid motion can signal the endothelium directly, it also drives interstitial flow that has been proposed to affect the sprouting process (Song and Munn, 2011). Moreover, interstitial flow can affect the distribution of growth factors, such as VEGF, which are chemical signals that control angiogenic sprouting (Gerhardt et al., 2003). Therefore, we expanded our technique and modelled interstitial flow dynamics and VEGF transport to study simultaneously the interplay of luminal shear stress, transmural shear stress, interstitial flow, and VEGF distribution in vascular development.

We found that fluid dynamic signals and VEGF gradients interact to control sprout initiation and elongation. When points where blood streams merge are excluded from all luminal shear stress minima, sprout occurred at the shear minima with the highest value of VEGF concentration and normal gradient. However, sprouts did not form necessarily at the point that had the highest VEGF concentration or normal spatial gradient. In other words, if we divide the endothelium arc length into high and low VEGF concentration, the sprout site locates in the higher VEGF region but within that region locates to shear stress minima. Thus, high VEGF concentrations and gradients are necessary for sprout initiation, but were not sufficient to locate the site of sprouting. Furthermore, flow dynamics alone were not sufficient to determine sprout initiation; however sprout occurred at points in which our identified flow dynamics conditions were fully satisfactory. We observed that there was a very narrow range of VEGF concentration or gradient present when sprouts initiated. A VEGF concentration threshold required for angiogenesis has previously been proposed by others (Secomb et al., 2013; von Degenfeld et al.,

2006). In regions with VEGF above threshold, sprouts were proposed to form in probability-dependent manner based on local VEGF concentration. Therefore, fluid dynamics and VEGF distribution do not control when a sprout will form, but rather where they are likely to form. Calculating the exact amount of the threshold is difficult, however, we observed no sprout initiation below an unbound $VEGF_{165}$ concentration of 4.5 pM in all 7 embryos investigated.

We demonstrated that interstitial flow plays a significant role in defining the sprouting location, the direction of sprouting and the rate of elongation in arterial vascular networks. Interstitial flow facilitates the transport of VEGF through the porous matrix of tissue, and changes the distribution of VEGF concentration and normal gradient significantly. It creates a higher VEGF micro-environment on the endothelium that exceed the VEGF concentrations predicted solely based on hypoxia. The higher VEGF region always corresponded to region of positive transmural shear stress through the endothelium (flow exits the avascular region into vessels). Thus, sprouts formed in regions with both high VEGF concentration and positive transmural shear stress. We speculated that they were both effective in sprout initiation. Unlike the luminal shear, we observed no relations between the location of sprouts and level of transmural shear stress. This is in complete agreement with one study (Hernández Vera et al., 2008) that demonstrated that the number of sprout formed remained constant with different interstitial velocities tested. However, the results are in contrast to another study that reported the existence of a transmural shear stress threshold above which sprouting was induced (Galie et al., 2014).

We also find that sprouts elongated in the opposite direction to interstitial flow. During the sprout morphogenesis from initiation to anastomosis, we split the process into two different steps. In the first step, the sprout formed and elongated towards VEGF maximum. Therefore,

VEGF gradient guides sprouts towards the VEGF maximum (i.e. hypoxic regions). Previous studies found that tip cells respond to VEGF gradient by extending filopodia and migrates towards VEGF source (Ferrara et al., 2003; Gerhardt et al., 2003; Ruhrberg et al., 2002). In the second step, the sprout passed the maximum of VEGF and moves towards other vessels. Since the sprout has passed the maximum, the VEGF gradient became negative. Our results showed that within this stage, the direction of sprout is closer to the interstitial flow stream, and as a result, interstitial flow guides the sprout to opposite side. This finding was corroborated by a previous study which found that filopodia produced by tip cells followed the local interstitial flow environment (Song and Munn, 2011). Another phenomenon that might contribute in the continuing of sprout migration after passing gradient is that stalk cells respond to the local concentration of VEGF by proliferation (Gerhardt et al., 2003). In this model, the sprout elongates because of proliferation at the base. Our results, however, show that elongation is not proportional to VEGF concentration, even when considering only the VEGF concentration at the base of the sprout.

Once sprouting was initiated, it required continuous interstitial flow to continue progression and avoid retraction. We found a strong relationship between the elongation rate and shear stress over the sprout leading edge. Shear stress over the sprout elongation is proportional to interstitial flow velocity of that location. Therefore, the rate of elongation strongly was as strongly correlated to the level of shear stress as to the velocity of the flow. The magnitude of the shear stress on the sprout is extremely low, and unlikely to be biologically active. Factors that are carried in with the interstitial flow either from the blood plasma or from the contralateral endothelial cells, would scale with the velocity of the interstitial flow and therefore represent an alternate interpretation of our results.

We previously showed that the sprouts always formed on the lower pressure side of an avascular region, and that elongation rate is proportional to the pressure differences across an avascular area (Ghaffari et al., 2015a). In this work, we show that this occurs because pressure differences between the vessels regulate the interstitial flow patterns. These pressure differences therefore control VEGF gradient and distribution. Though much of the work on blood flow investigates direct activation of the endothelium by the endothelium, our current work highlights that flow also has secondary effects on chemical signals within tissues, and highlight the important consequences of these secondary effects on vascular morphogenesis.

6.6 Materials and Methods

6.6.1 Flow Field in Free and Porous Media

The technique to image flow dynamics and vascular morphology has previously been described in extensive detail (Ghaffari et al., 2015b). The vessel geometry obtained by image processing, inlet and outlet flow velocities to the region of interest obtained by μ PIV were input into the computational fluid dynamic (CFD) solver. The vessel walls were assumed rigid and permeable. Therefore, inside the vessels, blood flows as a free flow, whereas in mesenchyme, interstitial flow created by pressure difference across the vessel walls, filtrates through an isotropic porous matrix (Supplemental Fig. 5). The hydraulic conductivity of the endothelial monolayer can be taken into account to obtain the flow field of the entire domain. However, we assume the endothelial monolayer as a quasi-porous medium layer with an assumed artificial permeability to mimic the hydraulic conductivity of the monolayer. The blood flow in capillaries is described by the Navier-Stokes equation, whereas interstitial flow is described by a Forchheimer-corrected version of the Brinkman-Darcy equations in the porous regions. For a

network with N inlet and outlets, the velocities of N - 1 segments were obtained from μ PIV as boundary conditions. For the last vessel segment, the pressure at the outlet was set to zero. The domain was meshed with extremely fine free triangular meshes. The CFD solver (COMSOL Multiphysics) was set to solve the coupled Navier-Stokes and Brinkman-Darcy equations for laminar, time-dependent, incompressible flow. At the lumen/endothelial and endothelial/mesenchyme interfaces, continuity of normal velocities and normal stresses were used as boundary conditions.

6.6.2 Calculation of Permeability and Tortuosity in the Mesenchyme

Using Scanning Electron Microscopic (SEM) images of the primitive vascular network in chick embryos at 10 somites (Hirakow and Hiruma, 1981), we calculated porosity and permeability of the mesenchymal tissues. The SEM images were thresholded to acquire the average of pore size and the volume fraction of pore space (porosity) from binary images. The pore size and porosity were found to be 4.3 μm and 0.27, respectively. Assuming all pores randomly orientated and have equal circular diameter of the calculated average, the permeability was obtained using the relationship between typical pore diameter and porosity (Bear, 2013)

$$k = \frac{\varepsilon \delta^2}{96} \quad (6.1)$$

Where ε is the porosity and δ is the calculated average pore size. The tortuosity of fluid flow in porous media was calculated from the following equation (Koponen et al., 1996)

$$\tau = 0.8(1 - \varepsilon) + 1 \quad (6.2)$$

The permeability and tortuosity were calculated $5.2 \times 10^{-14}m^2$ and 1.58 from equations (6.1) and (6.2) respectively.

To calculate the hydraulic conductivity of the endothelial monolayer, we also assumed a porous medium, however with different permeability and tortuosity. We calculated these based on the dimension of the endothelial cells and of the junctions between endothelial cells (Supplemental Fig. 6A).

To assess average endothelial cell size, mice embryo at equivalent stage were labeled with VE-Cadherin and imaged (Supplemental Fig. 6B). The average length of endothelial cells was $30\mu m$ and average width was $7\mu m$. The average of endothelial cell size in the capillary plexus of 11-somites stage quail embryo was reported to be $142.62 \mu m^2$ (LaRue et al., 2003). Keeping the shape factor of the cells the same as for mice embryos, the average of cell length and width were set to $24.67\mu m$ and $5.76\mu m$, respectively.

Transmission Electron Microscopy (TEM) was used to assess junction dimension. Quail embryos at the desired stage were injected with an Alcian Blue fixative solution and left in the egg for 30 minutes. The embryos were dissected and the body and yolk sac of the embryos were cut into small ($1mm^2$) pieces. Tissue sections were then fixed for 60 other minutes in the presence of Alcian Blue, post-fixed for 60 minutes in 1% osmium tetroxide, then 90 minutes in 1% uranyl acetate. Samples were dehydrated to acetone over the course of 90 minutes, embedded in epoxy and allowed to harden in a $59^\circ C$ oven. The samples were then placed on grids for TEM and imaged on a FEI Tecnai 12 120kV equipped with an AMT XR80C CCD Camera (Fig. 6C supplemental). At several points along the cell membranes of different embryos, the widths and lengths of the cell–cell junctions are measured. The averages for width and length of junctions

are 70nm and 3 μ m respectively. As a result, the endothelium thickness (which is the same as length of junctions) assumed constant value of 3 μ m at the interface of the flowing blood and the mesenchyme in our simulations.

From these measurements, the porosity of monolayer in our model was calculated to be 0.015 (area of cleft/total area or A_{cleft}/A).

6.6.3 Calculation of Permeability of Endothelial Cell Layer

The resistance to fluid flow (ratio of pressure drop to volumetric flow rate) in the monolayer can be obtained assuming that interstitial liquids flow through the junctions between endothelial cells, and using the equations for laminar and fully developed flow between parallel plates from:

$$R_{\text{monolayer}} = \frac{3\mu L_{\text{junc}}}{2p(d_{\text{junc}}/2)^3} \quad (6.3)$$

where L_{junc} is the length of the junctions, and p is the total perimeter of cells forming the monolayer. The perimeter was calculated based on the perimeter of each cell and an estimation of number of cell in a typical monolayer.

For flow through a porous medium, the resistance to fluid flow is calculated from the equation:

$$R_{\text{porous}} = \frac{\mu L_{\text{junc}}}{kA} \quad (6.4)$$

where k is the permeability, and A is the total cross-sectional area of the monolayer. To assume the monolayer as a porous medium, the resistance to fluid from equations (6.3) and (6.4) must be equal. Therefore, we calculated the permeability of $1 \times 10^{-17} \text{ m}^2$ for the monolayer.

6.6.4 Validation of Laminar Flow Assumption in Junctions and Transmural Shear Stress

The geometry of junctions can be assumed as continuous parallel plates. The velocity of flow through the junction can be obtained from the calculated superficial velocity of flow across the monolayer, but limiting it the flow to only the junctions using:

$$V_{junc} = A/A_{cleft} \times V_{superficial} \quad (6.5)$$

The Reynolds number (Re) of flow within the junction was calculated from the cell junction geometry and velocity of the flow:

$$Re = \frac{\rho V_{junc} d_{junc}}{\mu} \ll 1 \quad (6.6)$$

where ρ and μ are density and viscosity of interstitial fluid, and d_{junc} is the junction width. The highest Reynolds number in all the embryos and time points (obtained from the highest velocity), was estimated in the order of magnitude of $1e^{-6}$. The entrance length of the flow can be estimated as $0.315d_{junc}$ using the entrance length relationship for parallel plates (Shah and London, 2014), while $Re \ll 1$ within the cell junctions. Therefore, the entrance length was calculated 22.05 nm, which is 0.7% of the junction length. Thus, even for the longest entrance length (occurred for the highest junctional velocity), the junction is fully developed for more than 99% of its length. Thus, we assumed the flow in the junction is laminar and fully developed

for the entire junction. Shear stress on the wall of junction (transmural shear stress) was calculated from

$$\tau = \frac{6V_{junc}\mu}{d_{junc}} \quad (6.7)$$

6.6.5 Oxygen Transport in Blood Vessels and Tissue

Blood flow facilitates transport of oxygen from the vascular area to tissue, although only very little oxygen transport is carried by hemoglobin by the third day of incubation (Ciotto and Arangi, 1989). The dissolved oxygen terms are present at this stage, and can be significant if hematocrit is very slight (Secomb et al., 2004). Furthermore, oxygen transport in hemoglobin and myoglobin solutions, and also in suspensions of erythrocytes, is quicker than in water (Schmidt-Nielsen, 1997). Embryos used in the current work started at 40 h of incubation (15 somites or HH12) and were imaged over a 10 h time period. Therefore, we assume them all to be at the second day of incubation. Furthermore, we limited our analysis to time-lapse experiments in the arterial plexus of the yolk sac (vitteline arteries). The mean oxygen partial pressure (P_{O_2}) in the vitteline arteries for the 2 days old embryo when the eggshell and shell membranes were removed, was reported to be 40 mmHg (Baumann and Meuer, 1992; Lomholt, 1984). Thus, the partial pressure of oxygen was assumed 40 mmHg at all inlets to the domain of interest and the fully developed boundary condition was applied at the extended outlet of the domain (a straight section of vessel was added to allow the mass transfer to reach fully developed conditions). The steady-state oxygen transport inside the tissue is governed by the reaction-diffusion equation:

$$D_{O_2} \alpha \nabla^2 P_{O_2} = M(P_{O_2}) \quad (6.8)$$

where D_{O_2} and α are diffusivity and solubility in tissue. $M(P_{O_2})$ is the rate of oxygen consumption and assumed using Michaelis-Menten kinetics:

$$M(P_{O_2}) = M_0 \frac{P_{O_2}}{P_{O_2} + P_m} \quad (6.9)$$

where P_m is the value of P_{O_2} at half-maximal consumption, and M_0 is the oxygen demand. The oxygen demand can be obtained from oxygen consumption rate of early chicken embryo (Burggren et al., 2000). At the blood-tissue interface, the continuity of oxygen tension and oxygen flux should be satisfied. After the solution, it was observed that the maximum difference between the highest and the lowest oxygen tension is always less than 0.01% which is highly negligible. Therefore, we modelled the diffusion in the tissue, equation (6.8), with the oxygen partial pressure at the interface was set to 40 mmHg.

6.6.6 VEGF Transport in the Tissue

VEGF concentration within the tissue is governed by the mass balance reaction-diffusion equation:

$$\begin{aligned} \frac{\partial C_{V165}}{\partial t} + \vec{V} \cdot \nabla C_{V165} = & D_{V165} \nabla^2 C_{V165} + S_{V165}(P_{O_2}) - \frac{k_{on}}{K_{ECM}} C_{V165} C_H + k_{off} C_{V165H} - \\ & \frac{k_p}{K_{ECM}} C_{V165} C_P - k_{deg} C_{V165} \end{aligned} \quad (6.10)$$

where C_{V165} , C_H , C_{V165H} , C_P are bulk concentrations of the soluble fraction of VEGF₁₆₅, HSPG, VEGF₁₆₅ bound to HSPG, protease respectively, \vec{V} is Darcy velocity vector in mesenchyme, D_{V165} is the effective diffusivity of VEGF₁₆₅, k_{on} and k_{off} are rates of binding and dissociation to

HSPG, K_{ECM} is the available volume fraction of ECM, k_p is the effective bimolecular rate constant of proteolysis between VEGF₁₆₅ and protease, k_{deg} is the degradation rate of soluble VEGF. All rate constants were assumed spatially uniform. S_{V165} is the secretion rate of VEGF₁₆₅, and is dependent on the average oxygen tension. The dependence of release rate on P_{O_2} for both VEGF₁₆₅ and VEGF₁₂₁ is (Mac Gabhann et al., 2007):

$$S_V(P_{O_2}) = \begin{cases} 6S_0; & P_{O_2} \leq 1mmHg \\ S_0 \left[1 + 5 \times \left(\frac{20-P_{O_2}}{19} \right)^3 \right]; & 1mmHg < P_{O_2} < 20mmHg \\ S_0; & P_{O_2} \geq 20mmHg \end{cases} \quad (6.11)$$

where S_0 is the basal secretion level. Unbound VEGF concentrations under resting conditions were set to 1.5 pM taken from *in vivo* measurements of free interstitial VEGF in human skeletal muscle (Höffner et al., 2003). We solved model for the resting conditions to obtain the average VEGF concentration of 1.5 pM in the domain. The different secreted VEGF isoforms at the basal rate then can be calculated using relative mRNA abundances for different VEGF isoforms in mouse skeletal muscle (Ng et al., 2001). The basal secretion rate were calculated $1.9 \times 10^{-12} \frac{mol}{m^3.s}$ ($1.784 \times 10^{-12} \frac{mol}{m^3.s}$ for VEGF₁₆₅ and $0.152 \times 10^{-12} \frac{mol}{m^3.s}$ for VEGF₁₂₁). Similarly the VEGF distribution can be obtained for VEGF₁₂₁ :

$$\frac{\partial C_{V121}}{\partial t} + \vec{V} \cdot \nabla C_{V121} = D_{V121} \nabla^2 C_{V121} + S_{V121}(P_{O_2}) - k_{deg} C_{V165} \quad (6.12)$$

Cleaved VEGF (VEGF₁₁₄) is generated from cleavage of either free or matrix-bound VEGF₁₆₅:

$$\frac{\partial C_{V114}}{\partial t} + \vec{V} \cdot \nabla C_{V114} = D_{V114} \nabla^2 C_{V114} + \frac{k_p}{K_{ECM}} C_{V165} C_P + \frac{k_p}{K_{ECM}} C_{V165H} C_P - k_{deg} C_{V114} \quad (6.13)$$

The matrix components, i.e. HSPG and VEGF₁₆₅ bound to HSPG do not diffuse, however the reaction with VEGF and protease is described as

$$\frac{\partial C_H}{\partial t} = -\frac{k_{on}}{K_{ECM}} C_{V165} C_H + k_{off} C_{V165H} + \frac{k_p}{K_{ECM}} C_{V165} C_P \quad (6.14)$$

$$\frac{\partial C_{V165H}}{\partial t} = \frac{k_{on}}{K_{ECM}} C_{V165} C_H - k_{off} C_{V165H} - \frac{k_p}{K_{ECM}} C_{V165} C_P \quad (6.15)$$

Assuming uniform distribution of protease instead of protease secretion at the new sprouting points does not affect the VEGF distribution. For simplicity, we assumed protease is secreted simultaneously by numerous cells, and its concentration is uniform. The level of MMP was determined previously to be less than 20 nM (Vempati et al., 2010). We assumed constant MMP level of 10nM, while varying the value in the range does not change the VEGF distribution significantly.

VEGF diffusion and reaction happen faster than morphological changes in vessels. Therefore, steady-state solution can be justified. We first modelled the VEGF distribution in the absence of VEGF-cleaving proteases. Then, VEGF proteolysis added to model, and the steady-state solution was obtained by solving the transient solution from the initial condition. The boundary condition is equality of the flux of normal VEGF concentration normal to the endothelial cell surface, with the rate of reaction at this surface.

Using the relation of the total HSPG sites and available ones $C_H = (C_H)_{total} - C_{V165H}$, and equation (6.14), matrix-bound VEGF can be calculated:

$$C_{V165H} = \frac{\frac{k_{on}}{K_{ECM}} C_{V165} (C_H)_{total}}{k_{off} + \frac{k_p}{K_{ECM}} C_P + \frac{k_{on}}{K_{ECM}} C_{V165}} \quad (6.16)$$

Therefore, the equation (6.10) can be rewrite for the steady-state as:

$$\vec{V} \cdot \nabla C_{V165} = D_{V165} \nabla^2 C_{V165} + S_{V165} (P_{O_2}) - k_{deg} C_{V165} - \frac{k_p}{K_{ECM}} C_p C_{V165} \left(1 + \frac{\frac{k_{on}}{K_{ECM}} C_{V165} (C_H)_{total}}{k_{off} + \frac{k_p}{K_{ECM}} C_p + \frac{k_{on}}{K_{ECM}} C_{V165}} \right) \quad (6.17)$$

At the endothelial cell surface, VEGF can be bound to the receptors. Receptor and ligand-receptor complex distributions were assumed to be homogenous and do not diffuse along the cell surface. With a constant flux of cell-surface expression (insertion) and internalization, a system of equations describing the VEGF receptors are (Mac Gabhann et al., 2007):

$$\frac{\partial C_{R1}}{\partial t} = k_{off,V114R1} C_{V114R1} + k_{off,V121R1} C_{V121R1} + k_{off,V165R1} C_{V165R1} - (k_{on,V114R1} C_{114} + k_{on,V121R1} C_{121} + k_{on,V165R1} C_{165} + k_{int,R1}) C_{R1} + S_{R1} \quad (6.18)$$

$$\frac{\partial C_{V114R1}}{\partial t} = k_{on,V114R1} C_{114} C_{R1} - (k_{off,V114R1} + k_{int,V114R1}) C_{V114R1} \quad (6.19)$$

$$\frac{\partial C_{V121R1}}{\partial t} = k_{on,V121R1} C_{121} C_{R1} - (k_{off,V121R1} + k_{int,V121R1}) C_{V121R1} \quad (6.20)$$

$$\frac{\partial C_{V165R1}}{\partial t} = k_{on,V165R1} C_{165} C_{R1} - (k_{off,V165R1} + k_{int,V165R1}) C_{V165R1} \quad (6.21)$$

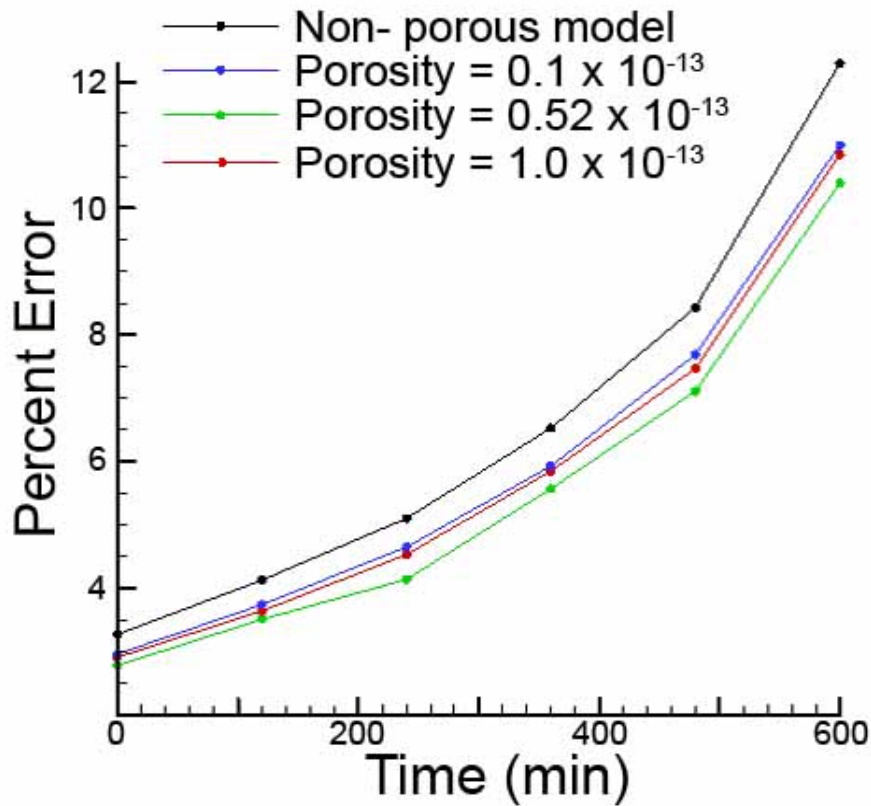
where C_{R1} , C_{V114R1} , C_{V121R1} , C_{V165R1} are concentrations of VEGFR1 free of ligand and VEGFR1 bound to different isoforms of VEGF, k_{on} and k_{off} are rates of binding and dissociation to receptors, k_{int} is internalization rate of surface receptors and complexes, and S_{R1} is the insertion rate of surface receptors to the endothelial cell membrane. Equations of VEGFR2 can be obtained by substitution of R2 for R1 in the above equations. All model parameter values are given in table (6.1).

Table 6.1- All Model Parameter values

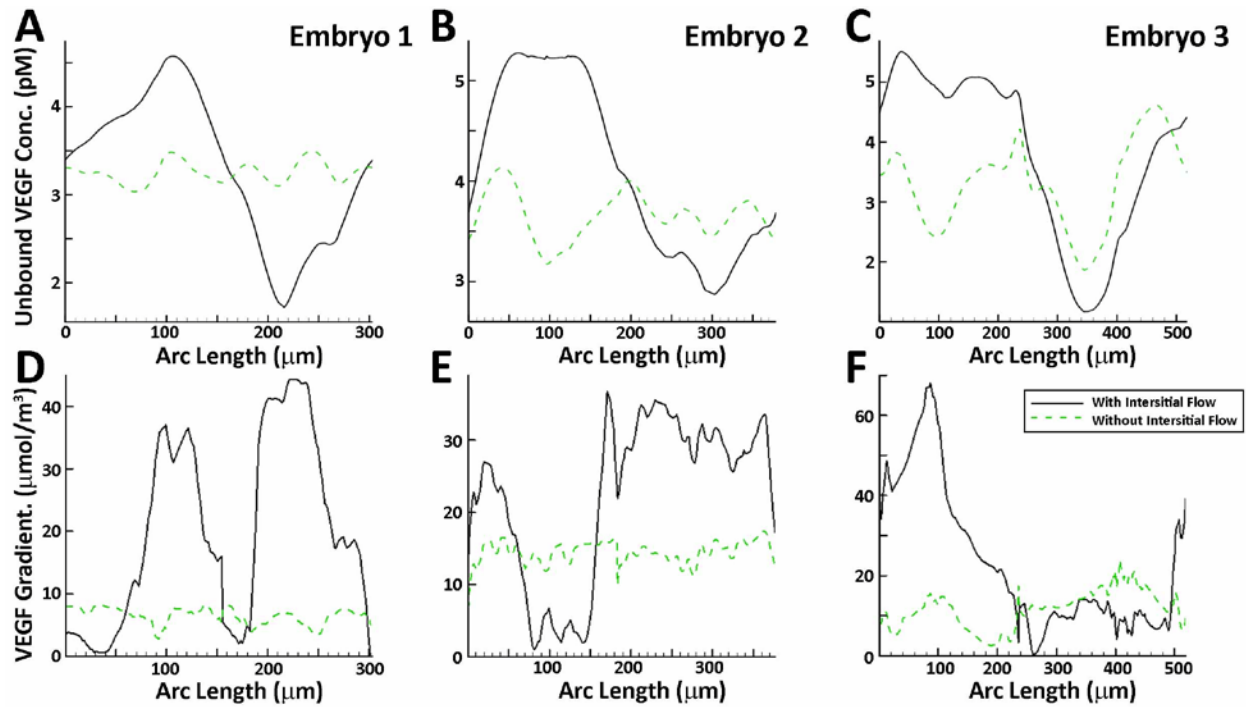
<i>Parameter</i>	<i>Value</i>	<i>Reference</i>
Mesenchymal Cells		
Porosity (ϵ)	0.27	measured
Permeability (k)	$5.2 \times 10^{-14} \text{m}^2$	calculated
Tortuosity (τ)	1.58	calculated
Monolayer		
Porosity (ϵ)	0.015	calculated
Permeability (k)	$1 \times 10^{-17} \text{m}^2$	calculated
Cell-Junction		
Junction length (L_{junc})	3 μm	measured
Junction width (d_{junc})	70 nm	measured
Oxygen Parameter		
Krogh diffusion constant ($D_{O_2} \alpha$)	$6 \times 10^{-8} \frac{\text{cm}^3 O_2}{\text{m.s.mmHg}}$	(Secomb et al., 2004)
Consumption demand (M_0)	$5.6 \times 10^3 \frac{\text{cm}^3 O_2}{\text{m}^3.\text{s}}$	(Burggren et al., 2000)
P_{O_2} at half-maximal consumption (P_m)	1 mmHg	(Secomb et al., 2013)
VEGF Parameter		
VEGF Diffusivity (D_V)	$6.88 \times 10^{-11} \text{m}^2/\text{s}$	(Vempati et al., 2010)
VEGF ₁₂₁ basal secretion rate (S_0)	$0.152 \times 10^{-12} \frac{\text{mol}}{\text{m}^3.\text{s}}$	calculated
VEGF ₁₆₅ basal secretion rate (S_0)	$1.784 \times 10^{-12} \frac{\text{mol}}{\text{m}^3.\text{s}}$	calculated
Binding rate to HSPG (k_{on})	$60.58 \frac{\text{m}^3}{\text{mol.s}}$	(Vempati et al., 2011)

Dissociation rate to HSPG (k_{off})	$0.01 \frac{1}{\text{s}}$	(Vempati et al., 2011)
Total concentration of HSPG ($(C_H)_{\text{total}}$)	$164.27 \times 10^{-6} \frac{\text{mol}}{\text{m}^3}$	(Mac Gabhann et al., 2007)
Cleavage rate of VEGF by protease (k_p)	$0.631 \frac{\text{m}^3}{\text{mol} \cdot \text{s}}$	(Vempati et al., 2010)
Degradation rate (k_{deg})	$0.001 \frac{1}{\text{s}}$	(Vempati et al., 2011)
Available volume fraction of ECM (K_{ECM})	0.85	(Yuan et al., 2001)
Binding rate to VEGFR1 ($k_{\text{on,VR1}}$)	$3 \times 10^4 \frac{\text{m}^3}{\text{mol} \cdot \text{s}}$	(Mac Gabhann et al., 2007)
Binding rate to VEGFR2 ($k_{\text{on,VR2}}$)	$1 \times 10^4 \frac{\text{m}^3}{\text{mol} \cdot \text{s}}$	(Mac Gabhann et al., 2007)
Dissociation rate to VEGFR1 ($k_{\text{off,VR1}}$)	$0.001 \frac{1}{\text{s}}$	(Mac Gabhann et al., 2007)
Dissociation rate to VEGFR2 ($k_{\text{off,VR2}}$)	$0.001 \frac{1}{\text{s}}$	(Mac Gabhann et al., 2007)
Internalization rate of receptors (k_{int})	$2.8 \times 10^{-4} \frac{1}{\text{s}}$	(Mac Gabhann et al., 2007)
Insertion rate of surface receptors (S_{R1})	$9.2 \times 10^{-16} \frac{\text{mol}}{\text{m}^2 \cdot \text{s}}$	(Mac Gabhann et al., 2007)
Insertion rate of surface receptors (S_{R2})	$3.8 \times 10^{-15} \frac{\text{mol}}{\text{m}^2 \cdot \text{s}}$	(Mac Gabhann et al., 2007)

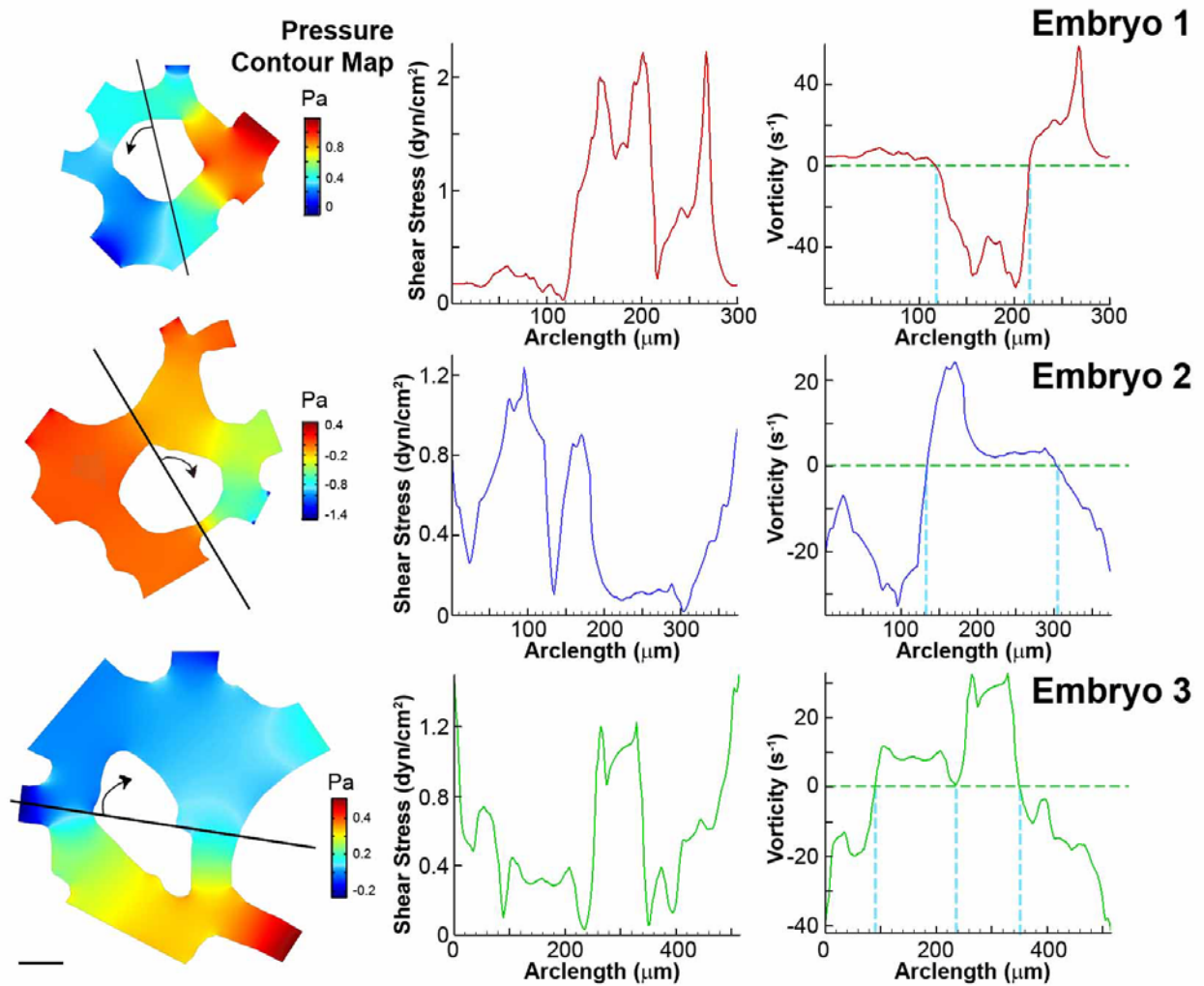
6.7 Supplementary information



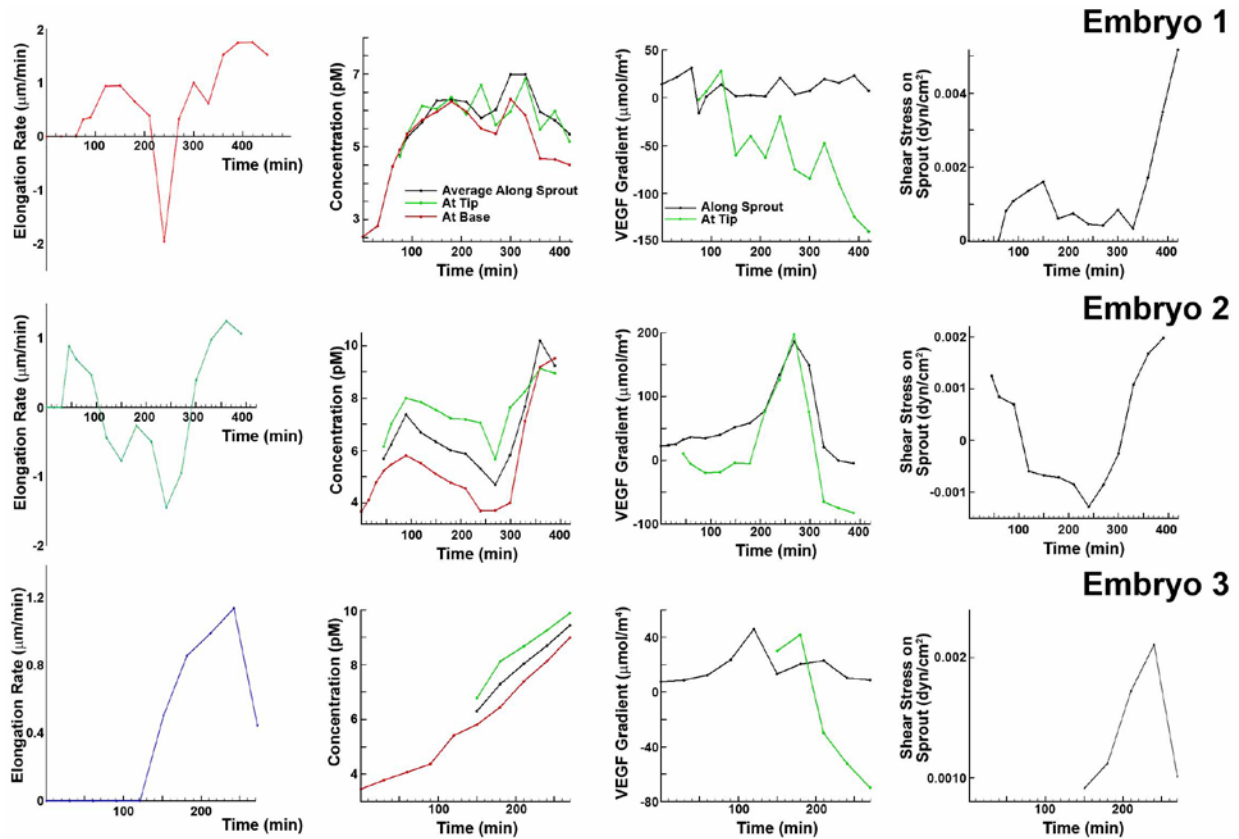
Supplemental Figure 1 – Error analysis in the flow measurements for different porosities of the permeabilities of the avascular tissue. Flow measurements were made using μ PIV at all inlet and outlet vessels to the region of interest, however one measurement was not used in the computational fluid dynamics computation. The value at the last location was therefore compared to the predicted value for velocity in order to calculate a percent error in the velocity calculations. We found that assuming porous avascular tissues reduced the error in the velocity measurement (black line indicates non-porous model). Furthermore, we tested several values of permeability for the avascular tissue. The calculated permeability of 5.2×10^{-14} resulted in the lowest percent error in the velocity measurement.



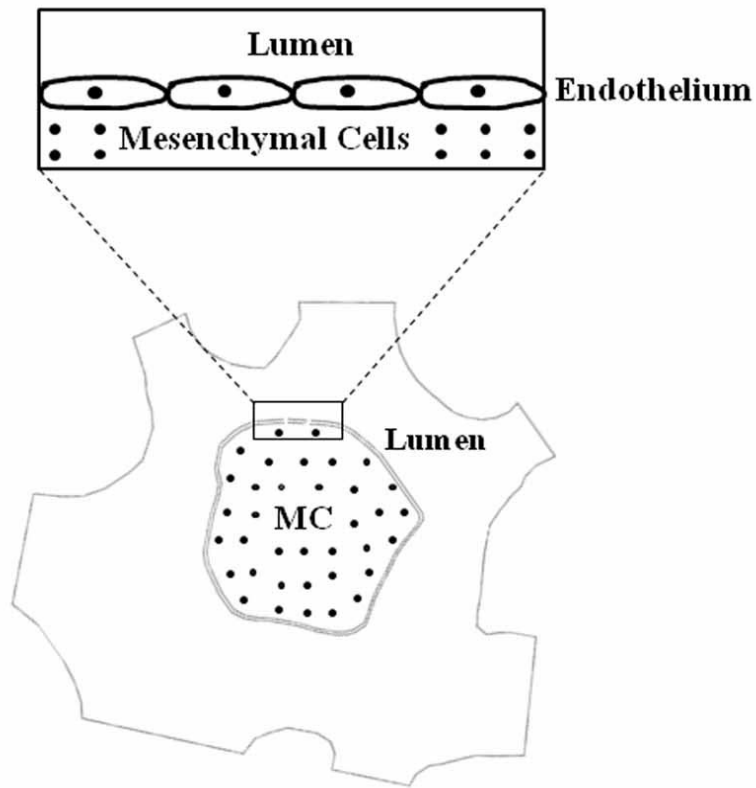
Supplemental Figure 2 – Effect of interstitial flow on the VEGF concentration and gradient along the endothelium. The VEGF concentration (A-C) and gradient (D-F) along the endothelium were calculated in the presence or absence of interstitial flow for three different embryos. In the absence of interstitial flow (green dotted line), both parameters vary very little along the length of endothelium. In the presence of interstitial flow, however, strong changes in both concentration and gradient arise (black solid line). The location of $x = 0$ for the arc length is depicted in Figure 5.



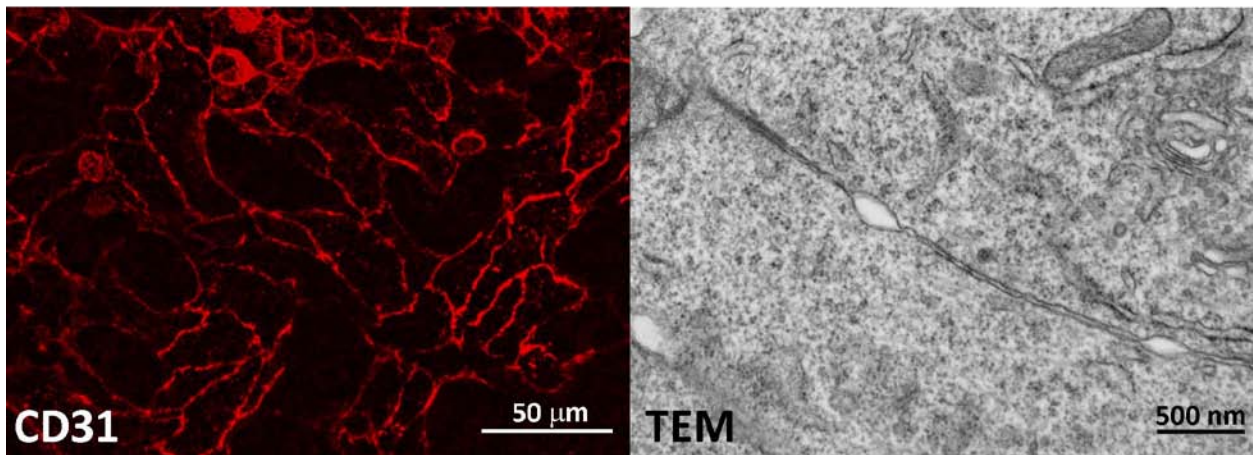
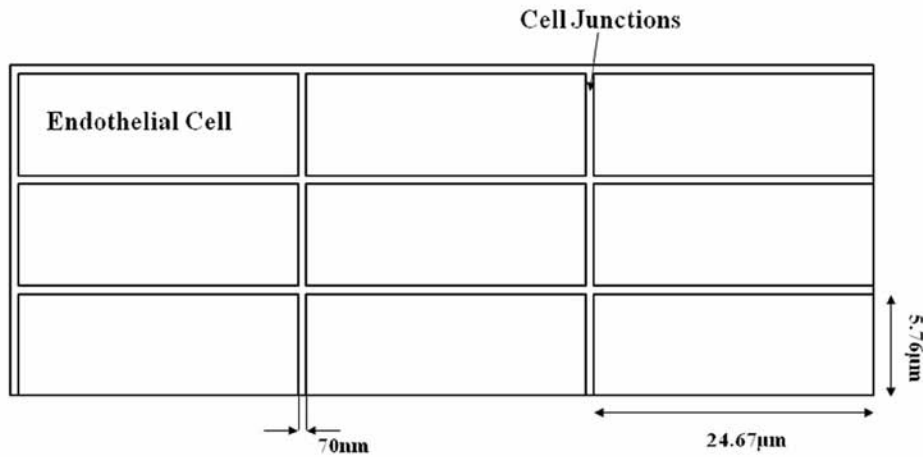
Supplemental Figure 3 – Hemodynamic data for entire arc length at the time point 30 minutes before sprout is visible. Pressure contours for each embryo are presented. Shear stress and vorticity values for the entire contour are shown. Light blue dotted lines indicate locations along the arc length where vorticity is equal to zero.



Supplemental Figure 4 – Analysis of growth factor and hemodynamic signals during elongation. Elongation rates with respect to time during sprout elongation are presented. The average unbound VEGF₁₆₅ concentration along the sprout, the concentration at the base, and the concentration at the tip, with respect to time, are shown for all three embryos. The gradient of VEGF₁₆₅, both at the tip and along the sprout, are shown for all three embryos. The shear stress along the sprout with respect to time was also calculated for all three embryos.



Supplemental Figure 5 – Schematic of tissue porosity in the endothelium and the mesenchymal region. The endothelium was assumed to consist of a monolayer of cells with thin junctions between cells. The mesenchyme was assumed to consist of extracellular matrix with individual cells distributed throughout. Interstitial was assumed to only occur in junctions between cells and in the extracellular matrix.



Supplemental Figure 6 – Calculation of porosity for the endothelial cell layer. Porosity was calculated based on the average size of endothelial cells at this stage and the dimension of the gap between endothelial cells (A). A membrane specific endothelial cell label is required to calculate average endothelial cell size. Such an antibody is not available for the avian embryo, therefore the length and width of endothelial cells in mouse embryos at an equivalent size were assessed using CD31 staining (B), and then adjusted for avian embryos based on difference in the size of endothelial cells at this stage between mouse and avian embryos. The dimensions of the gap junctions were assessed using transmission electron microscopy (TEM) of embryos at the same stage of development.

Supplemental Movie 1 – Analysis of blood flow and interstitial flow, and the effects on VEGF distribution during sprouting angiogenesis. The top left panel shows the endothelial cell behaviour during the time period of analysis. Endothelial cells were labelled by intravascular injection of fluorescent acetylated low-density lipoprotein. The top right panel shows calculated flow around and within avascular tissue during sprout elongation based on μ PIV results for inlets and outlets vessels to the region of interest. The bottom left panel shows calculated oxygen partial pressure based on oxygen diffusion and consumption within the tissue. Oxygen partial pressure were used to predict VEGF production. The final distribution of VEGF was then calculating allowing for both advection (i.e. movement with the bulk fluid motion) and diffusion of the VEGF. Concentration of all isoforms were included, as well as allowing VEGF₁₆₅ to bind the matrix and be released by MMP cleavage. Only data for unbound VEGF₁₆₅ is presented in the panel. All scale bars represent 100 μ m.

7 Original Contributions to Knowledge

Most significantly, this research has highlighted the significance of hemodynamics in vascular development. To aid this, we presented the first technique to follow changes in flow dynamics during vascular remodelling. To achieve this, we overcome several complexities such as adhesion of the tracer particles. The methodology which constitutes a combination of μ PIV and CFD, to estimate blood flow forces within the network throughout its development, could represent a widely used technique to characterize flow function during angiogenesis and vessel remodelling. That being said, through the work presented in this thesis using this technique, important significant advances in fundamental understanding of angiogenesis have been made. In particular, the novel contributions presented in this research are:

1. A novel set of dynamic observations in a live warm-blooded embryo was executed to investigate the role of flow dynamics stimuli during angiogenesis.
2. The studies are innovative and add important understanding regarding how biomechanical forces regulate the behavior of endothelial cells in remodelling vascular beds. The significance of the role physical force exerted by blood flow was highlighted in angiogenic sprouting initiation and direct elongation using calculation of hemodynamics parameters and finding a relationship between these parameter and change in morphology.
3. Luminal shear stress was confirmed as an inhibitor of angiogenesis *in vivo*.
4. The sprout, which was directed according to the pressure difference between two vessels and against the direction of interstitial flow, followed the VEGF gradient.

5. The sprout elongation rate was proportional to the pressure difference across interstitium and interstitial flow.
6. The sites where sprouts initiated were predicted based on flow dynamics parameters.
7. The interstitial flow was demonstrated to alter distribution of growth factors within a tissue.
8. The flow dynamics signals and chemical signal were indicated to cooperate in triggering the angiogenesis from sprout initiation to vascularization real time *in vivo*

8 Conclusion and Future Work

8.1 Conclusion

Angiogenesis is fundamental to several normal and pathological processes such as wound healing and tumor growth and it is therefore an important therapeutic target. The mechanisms that regulate sprout initiation and elongation are poorly understood. The complication of quantifying shear stress levels in real time has hindered the analysis of the role of hemodynamics in vascular development, and more specifically in angiogenesis. To aid in this, we developed a technique to concurrently capture blood flow dynamics and vascular morphogenesis. In this method, a combination of time-lapse imaging, flow visualisation and computational fluid dynamics (CFD) were used. We checked whether the method accurately predicted the pattern of blood flow to validate the calculated velocity field. The main aim of this research was to understand the effects of biomechanical signals on vascular remodelling *in vivo*. In addition, one of the strengths of this technique was that it enabled us to study the interaction of chemical signals and biomechanical signals.

This technique was applied to investigate the relationship between shear stress and chronic changes in vessel diameter during embryonic development, both in normal development and after TGF- β stimulation. The results presented in this work, demonstrates that vessels enlarge and regress proportional to the natural logarithm of the shear stress which agrees with physiological observations. Injection of TGF- β increased the rate of vessel enlargement in response to similar level of shear stress. These results underline the fact that chemical and biomechanical signals interact in a way that chemical signals regulate the response of endothelial cells to blood flow, and vice versa.

In the second manuscript, we applied our technique to investigate the effect of flow dynamics on sprout initiation and elongation in vascular development. We showed that flow patterns play a significant role in sprouting angiogenesis. We found that sprouts only initiate from a vessel at lower pressure towards a vessel at higher pressure. Within the lower pressure region, sprouts localised to points where the shear stress was at a minimum, once points where streams merge had been excluded. In other words, the sprout forms at the point with zero gradient of shear stress, i.e. the magnitude and sign of shear stress are the same at both sides of the sprouting location. The branching pattern in the capillary network significantly affects the hemodynamic efficiencies and the peripheral resistance to flow. Thus, it makes sense that flow dynamics have an important role in determining sprouting location. Our results indicated that the pressure difference between two vessels is proportional to elongation rate. Taken together, our results show that hemodynamics have a significant effect on the sprouting location, the direction of sprouting and the rate of elongation in the arterial vascular network. Flow dynamics are predictive of the location of sprout initiation in perfused vascular networks and pressure differences across the interstitium directs sprout elongation. This supports our hypothesis that initiation and elongation of new sprouts require the presence of specific hemodynamic conditions.

In the third manuscript, we broadened our technique to include modelling of interstitial flow through the porous matrix of the mesenchymal tissue. We then modelled VEGF transport within the tissue, in the presence of interstitial flow, to investigate how hemodynamics and chemical signals cooperate to modulate sprouting. VEGF alone is not sufficient to regulate angiogenesis, and it is believed additional signals are necessary to trigger the process. We had shown the significance of hemodynamics in angiogenesis in the previous chapter. As a result,

hemodynamic parameters, which control interstitial flow, are likely candidates. We modified our finding concerning determining sprouting location. If points with zero vorticity are excluded from the analysis of shear stress minima, then the shear stress minimum with the highest VEGF concentration identifies the location of sprouting. The regions with higher VEGF concentrations always corresponded to the lower pressure region, as discussed before. Moreover, these regions were always regions in which flow exits the avascular region into the vessels (positive transmural shear stress). We observed that level of VEGF concentration or gradient were always above a threshold value once sprout initiated. On the other hand, we demonstrated that interstitial flow influences the VEGF distribution significantly. We also showed that the sprout elongated against the direction of interstitial flow and towards the VEGF source. Furthermore, we found a strong relationship between the elongation rate and interstitial flow rate. We had shown in the previous manuscript that pressure difference across the interstitium directs sprout elongation is proportional to elongation rate. These pressure differences between the vessels control the interstitial flow patterns, and affect VEGF gradient and distribution as well. Taken together, in this manuscript we showed that in addition to signals from chemical signals such as VEGF, flow dynamics mediated angiogenic sprout initiation, elongation direction and the rate of sprout elongation. This support our hypothesis that angiogenesis occurs both directly through mechanical forces and indirectly, due to changes in the distribution of growth factors.

In conclusion, this work underlined the importance of several stimuli of vascular homeostasis and morphogenesis and provided insights into the role flow dynamics play as a key mediator for initiation of angiogenesis and the regulation of sprout structure. **It provides strong evidence to corroborate our overall hypothesis that specific hemodynamic conditions are present during sprouting and that these affect both the location and elongation of the**

sprout. This study opened the door to further studies of the biomechanical control of vascular remodelling.

8.2 Future Directions

8.2.1 Predicting When Sprouting Forms

Our results based purely on blood flow dynamics, without analysis of the VEGF redistribution by interstitial flow. We could predict where a sprout would form around an avascular region, but not which avascular regions would sprout. We did test whether the size of avascular regions alone predicted which regions would gain a sprout. Though avascular regions with sprouts were on average larger than those without, the size of the avascular region alone could not predict where a sprout would form. Our current model which contains flow dynamics, interstitial flow, and VEGF production could overcome these previous limitations. Our current results are limited to relatively small regions of interest. Ideally, by applying this model to larger regions and using the model with interstitial flow and VEGF production, we may be able to predict not only where but when sprouts form.

8.2.2 Extending the Applicability of the Method

Though the avian model has several attributes, ultimately application of these techniques to pathologies such as tumour vessel growth would be ideal. Our current analysis, however, is limited to a maximum of approximately 10 hours and can only be used in two-dimensional vascular beds. The time limit is due to the fact that the circulating microspheres slowly adhere to

the endothelium, increasing the amount of error in the PIV measurements over time. The limitation of the type of vascular is two-fold. First, our set-up used a fluorescence microscope and a multi-photon confocal microscope would be required for a three-dimensional bed. This first hurdle is easily overcome. The second hurdle, however, is that the need for velocity measurements in this three dimensional vascular bed. Our images were obtained at 250 fps and no multi-photon microscope currently exists that can obtain an entire 3D region within 4 milliseconds.

8.2.3 Shear-Induced Activation of MMPs

Our current model of VEGF transport includes the ability of VEGF to bind the matrix and be released by MMP-mediated cleavage. The limitation of the current model, however, is that MMP activation is homogeneously distributed within the tissues. In reality, MMPs are produced as inactive precursors and then activated MMP occurs in a spatially-restricted manner. MMPs are activated by tip cells, however, modelling of tip-cell specific activation has shown that one single tip cell has little effect on the overall VEGF signalling (Mac Gabhann et al., 2007). For this reason, we did not include differential activation of MMPs at the tip. MMPs can also be activated by shear stress (Kang et al., 2015; Kang et al., 2011). The role of this activation on VEGF transport has not been studied. Though we had initially hoped to include this aspect of MMP function in our model, this would require quantitative knowledge of the rate of MMP activation with respect to the levels of shear stress and this information is not currently available.

8.2.4 Perturbation from Normal Vascular Development

Our current results were obtained in normal vascular development, however perturbations from normal conditions could provide valuable insight into the remodelling process. All time-lapse recordings were established in normal oxygen conditions. To study the role of oxygen in angiogenesis, the condition can be changed such that the vascular remodels in the presence of hypoxia or hyperoxia. Moreover, viscosity of the blood can be lowered using erythroblast immobilization in the blood islands, and increased by injection of hetastarch. Comparison of embryos in normal development and in lower and higher viscosity conditions may improve our understanding of the role of mechanical forces.

Bibliography

- Abe, J. and Berk, B. C.** (2014). Novel mechanisms of endothelial mechanotransduction. *Arterioscler Thromb Vasc Biol* **34**, 2378-2386.
- Adamo, L., Naveiras, O., Wenzel, P. L., McKinney-Freeman, S., Mack, P. J., Gracia-Sancho, J., Suchy-Dicey, A., Yoshimoto, M., Lensch, M. W. and Yoder, M. C.** (2009). Biomechanical forces promote embryonic haematopoiesis. *Nature* **459**, 1131-1135.
- Adrian, R. J.** (1991). Particle-Imaging Techniques for Experimental Fluid-Mechanics. *Annu Rev Fluid Mech* **23**, 261-304.
- Adrian, R. J. and Westerweel, J.** (2011). *Particle image velocimetry*: Cambridge University Press.
- Akhurst, R. J., Lehnert, S. A., Faissner, A. and Duffie, E.** (1990). TGF beta in murine morphogenetic processes: the early embryo and cardiogenesis. *Development* **108**, 645-656.
- Al-Roubaie, S., Hughes, J. H., Filla, M. B., Lansford, R., Lehoux, S. and Jones, E. A.** (2012). Time-lapse microscopy of macrophages during embryonic vascular development. *Dev Dyn* **241**, 1423-1431.
- Al-Roubaie, S., Jahnsen, E. D., Mohammed, M., Henderson-Toth, C. and Jones, E. A.** (2011). Rheology of embryonic avian blood. *Am J Physiol Heart Circ Physiol* **301**, H2473-2481.
- Bai, Y., Leng, Y., Yin, G., Pu, X., Huang, Z., Liao, X., Chen, X. and Yao, Y.** (2014). Effects of combinations of BMP-2 with FGF-2 and/or VEGF on HUVECs angiogenesis in vitro and CAM angiogenesis in vivo. *Cell Tissue Res* **356**, 109-121.
- Baumann, R.** (1992). Oxygen Transport in the Early Embryo. In *OXYGEN: Basis of the Regulation of Vital Functions in the Fetus*, pp. 188-193: Springer.
- Baumann, R. and Meuer, H.-J.** (1992). Blood oxygen transport in the early avian embryo. *Physiological reviews* **72**, 941-965.
- Bear, J.** (2013). *Dynamics of fluids in porous media*: Courier Corporation.
- Bergers, G., Brekken, R., McMahon, G., Vu, T. H., Itoh, T., Tamaki, K., Tanzawa, K., Thorpe, P., Itohara, S. and Werb, Z.** (2000). Matrix metalloproteinase-9 triggers the angiogenic switch during carcinogenesis. *Nature cell biology* **2**, 737-744.
- Bharadwaj, K. N., Spitz, C., Shekhar, A., Yalcin, H. C. and Butcher, J. T.** (2012). Computational fluid dynamics of developing avian outflow tract heart valves. *Annals of biomedical engineering* **40**, 2212-2227.
- Brinkmann, C. K., Wolf, S. and Wolf-Schnurrbusch, U. E. K.** (2008). Multimodal imaging in macular diagnostics: combined OCT-SLO improves therapeutical monitoring. *Graef Arch Clin Exp* **246**, 9-16.
- Brown, M. S., Basu, S. K., Falck, J. R., Ho, Y. K. and Goldstein, J. L.** (1980). The scavenger cell pathway for lipoprotein degradation: specificity of the binding site that mediates the uptake of negatively-charged LDL by macrophages. *J Supramol Struct* **13**, 67-81.
- Bruns, G. A. and Ingram, V. M.** (1973). The erythroid cells and haemoglobins of the chick embryo. *Philosophical Transactions of the Royal Society of London B: Biological Sciences* **266**, 225-305.
- Bryan, M. T., Duckles, H., Feng, S., Hsiao, S. T., Kim, H. R., Serbanovic-Canic, J. and Evans, P. C.** (2014). Mechanoresponsive networks controlling vascular inflammation. *Arterioscler Thromb Vasc Biol* **34**, 2199-2205.

- Burggren, W. W.** (2004). What is the purpose of the embryonic heart beat? Or how facts can ultimately prevail over physiological dogma. *Physiological and Biochemical Zoology* **77**, 333-345.
- Burggren, W. W., Warburton, S. J. and Slivkoff, M. D.** (2000). Interruption of cardiac output does not affect short-term growth and metabolic rate in day 3 and 4 chick embryos. *Journal of Experimental Biology* **203**, 3831-3838.
- Buschmann, I. and Schaper, W.** (1999). Arteriogenesis versus angiogenesis: two mechanisms of vessel growth. *Physiology* **14**, 121-125.
- Canny, J.** (1986). A Computational Approach to Edge-Detection. *IEEE T Pattern Anal* **8**, 679-698.
- Carmeliet, P., Ferreira, V., Pollefeyt, S. and Kieckens, L.** (1996). Abnormal blood vessel development and lethality in embryos lacking a single VEGF allele. *Nature* **380**, 435-439.
- Carmeliet, P. and Jain, R. K.** (2011). Molecular mechanisms and clinical applications of angiogenesis. *Nature* **473**, 298-307.
- Chapman, W.** (1918). The effect of the heart-beat upon the development of the vascular system in the chick. *American Journal of Anatomy* **23**, 175-203.
- Chouinard-Pelletier, G., Jahnsen, E. D. and Jones, E. A.** (2013). Increased shear stress inhibits angiogenesis in veins and not arteries during vascular development. *Angiogenesis* **16**, 71-83.
- Cirotto, C. and Arangi, I.** (1989). How do avian embryos breathe? Oxygen transport in the blood of early chick embryos. *Comparative Biochemistry and Physiology Part A: Physiology* **94**, 607-613.
- Cumano, A. and Godin, I.** (2007). Ontogeny of the hematopoietic system. *Annu. Rev. Immunol.* **25**, 745-785.
- Davies, P. F., Remuzzi, A., Gordon, E. J., Dewey, C. F., Jr. and Gimbrone, M. A., Jr.** (1986). Turbulent fluid shear stress induces vascular endothelial cell turnover in vitro. *Proc Natl Acad Sci U S A* **83**, 2114-2117.
- DeGroof, C., Thornburg, B., Pentecost, J., Thornburg, K., Gharib, M., Sahn, D. and Baptista, A.** (2003). Flow in the early embryonic human heart. *Pediatric cardiology* **24**, 375-380.
- Djonov, V., Schmid, M., Tschanz, S. and Burri, P.** (2000). Intussusceptive angiogenesis its role in embryonic vascular network formation. *Circulation research* **86**, 286-292.
- Dolan, J. M., Meng, H., Singh, S., Paluch, R. and Kolega, J.** (2011). High fluid shear stress and spatial shear stress gradients affect endothelial proliferation, survival, and alignment. *Ann Biomed Eng* **39**, 1620-1631.
- Dvorak, H. F., Brown, L. F., Detmar, M. and Dvorak, A. M.** (1995). Vascular permeability factor/vascular endothelial growth factor, microvascular hyperpermeability, and angiogenesis. *The American journal of pathology* **146**, 1029.
- Fahraeus, R.** (1929). The suspension stability of the blood. *Physiol Rev* **9**, 241-274.
- Ferrara, N.** (2004). Vascular endothelial growth factor: basic science and clinical progress. *Endocrine reviews* **25**, 581-611.
- Ferrara, N., Gerber, H.-P. and LeCouter, J.** (2003). The biology of VEGF and its receptors. *Nature medicine* **9**, 669-676.
- Flamme, I., Frölich, T. and Risau, W.** (1997). Molecular mechanisms of vasculogenesis and embryonic angiogenesis. *Journal of cellular physiology* **173**, 206-210.
- Fong, G.-H., Rossant, J., Gertsenstein, M. and Breitman, M. L.** (1995). Role of the Flt-1 receptor tyrosine kinase in regulating the assembly of vascular endothelium. *Nature* **376**, 66-70.

- Galie, P. A., Nguyen, D.-H. T., Choi, C. K., Cohen, D. M., Janmey, P. A. and Chen, C. S.** (2014). Fluid shear stress threshold regulates angiogenic sprouting. *Proceedings of the National Academy of Sciences* **111**, 7968-7973.
- Gerhardt, H., Golding, M., Fruttiger, M., Ruhrberg, C., Lundkvist, A., Abramsson, A., Jeltsch, M., Mitchell, C., Alitalo, K. and Shima, D.** (2003). VEGF guides angiogenic sprouting utilizing endothelial tip cell filopodia. *The Journal of cell biology* **161**, 1163-1177.
- Geudens, I. and Gerhardt, H.** (2011). Coordinating cell behaviour during blood vessel formation. *Development* **138**, 4569-4583.
- Ghaffari, S., Leask, R. L. and Jones, E. A.** (2015a). Flow dynamics control the location of sprouting and direct elongation during developmental angiogenesis. *Development* **142**, 4151-4157.
- Ghaffari, S., Leask, R. L. and Jones, E. A.** (2015b). Simultaneous imaging of blood flow dynamics and vascular remodelling during development. *Development* **142**, 4158-4167.
- Gijsen, F. J. H., Wentzel, J. J., Thury, A., Lamers, B., Schuurblers, J. C. H., Serruys, P. W. and Van der Steen, A. F.** (2007). A new imaging technique to study 3-D plaque and shear stress distribution in human coronar arter bifurcations in vivo. *J Biomech* **40**, 2349-2357.
- Goumans, M.-J., Liu, Z. and ten Dijke, P.** (2009). TGF- β signaling in vascular biology and dysfunction. *Cell research* **19**, 116-127.
- Goumans, M.-J. and Mummery, C.** (2002). Functional analysis of the TGFbeta receptor/Smad pathway through gene ablation in mice. *International Journal of Developmental Biology* **44**, 253-265.
- Goumans, M. J., Valdimarsdottir, G., Itoh, S., Rosendahl, A., Sideras, P. and ten Dijke, P.** (2002). Balancing the activation state of the endothelium via two distinct TGF- β type I receptors. *The EMBO journal* **21**, 1743-1753.
- Groenendijk, B. C., Hierck, B. P., Vrolijk, J., Baiker, M., Pourquie, M. J., Gittenberger-de Groot, A. C. and Poelmann, R. E.** (2005). Changes in shear stress-related gene expression after experimentally altered venous return in the chicken embryo. *Circulation research* **96**, 1291-1298.
- Hallmann, R., Feinberg, R. N., Latker, C. H., Sasse, J. and Risau, W.** (1987). Regression of blood vessels precedes cartilage differentiation during chick limb development. *Differentiation* **34**, 98-105.
- Hanahan, D. and Folkman, J.** (1996). Patterns and emerging mechanisms of the angiogenic switch during tumorigenesis. *Cell* **86**, 353-364.
- Helm, C.-L. E., Fleury, M. E., Zisch, A. H., Boschetti, F. and Swartz, M. A.** (2005). Synergy between interstitial flow and VEGF directs capillary morphogenesis in vitro through a gradient amplification mechanism. *Proceedings of the National Academy of Sciences of the United States of America* **102**, 15779-15784.
- Helm, C. L. E., Zisch, A. and Swartz, M. A.** (2007). Engineered blood and lymphatic capillaries in 3-D VEGF-fibrin-collagen matrices with interstitial flow. *Biotechnology and bioengineering* **96**, 167-176.
- Henderson-Toth, C. E., Jahnsen, E. D., Jamarani, R., Al-Roubaie, S. and Jones, E. A.** (2012). The glycocalyx is present as soon as blood flow is initiated and is required for normal vascular development. *Developmental biology* **369**, 330-339.
- Hernández Vera, R., Genové, E., Alvarez, L., Borrós, S., Kamm, R., Lauffenburger, D. and Semino, C. E.** (2008). Interstitial fluid flow intensity modulates endothelial sprouting in restricted Src-activated cell clusters during capillary morphogenesis. *Tissue Engineering Part A* **15**, 175-185.

- Hirakow, R. and Hiruma, T.** (1981). Scanning electron microscopic study on the development of primitive blood vessels in chick embryos at the early somite-stage. *Anatomy and embryology* **163**, 299-306.
- Hobson, B. and Denekamp, J.** (1984). Endothelial proliferation in tumours and normal tissues: continuous labelling studies. *Br J Cancer* **49**, 405-413.
- Höffner, L., Nielsen, J. J., Langberg, H. and Hellsten, Y.** (2003). Exercise but not prostanoids enhance levels of vascular endothelial growth factor and other proliferative agents in human skeletal muscle interstitium. *The Journal of physiology* **550**, 217-225.
- Hogers, B., DeRuiter, M., Gittenberger-de Groot, A. and Poelmann, R.** (1997). Unilateral vitelline vein ligation alters intracardiac blood flow patterns and morphogenesis in the chick embryo. *Circulation research* **80**, 473-481.
- Høiby, M., Aulie, A. and Reite, O. B.** (1983). Oxygen uptake in fowl eggs incubated in air and pure oxygen. *Comparative Biochemistry and Physiology Part A: Physiology* **74**, 315-318.
- Hoover, A. and Goldbaum, M.** (2003). Locating the optic nerve in a retinal image using the fuzzy convergence of the blood vessels. *IEEE Trans Med Imaging* **22**, 951-958.
- Hove, J. R., Köster, R. W., Forouhar, A. S., Acevedo-Bolton, G., Fraser, S. E. and Gharib, M.** (2003). Intracardiac fluid forces are an essential epigenetic factor for embryonic cardiogenesis. *Nature* **421**, 172-177.
- Immordino, M. L., Dosio, F. and Cattell, L.** (2006). Stealth liposomes: review of the basic science, rationale, and clinical applications, existing and potential. *Int J Nanomedicine* **1**, 297-315.
- Iomini, C., Tejada, K., Mo, W., Vaananen, H. and Piperno, G.** (2004). Primary cilia of human endothelial cells disassemble under laminar shear stress. *The Journal of cell biology* **164**, 811-817.
- Ji, R. P., Phoon, C. K., Aristizábal, O., McGrath, K. E., Palis, J. and Turnbull, D. H.** (2003). Onset of cardiac function during early mouse embryogenesis coincides with entry of primitive erythroblasts into the embryo proper. *Circulation research* **92**, 133-135.
- Jones, E., Baron, M., Fraser, S. and Dickinson, M.** (2004). Measuring hemodynamic changes during mammalian development. *American Journal of Physiology-Heart and Circulatory Physiology* **287**, H1561-H1569.
- Jones, E. A.** (2010). Mechanotransduction and blood fluid dynamics in developing blood vessels. *The Canadian Journal of Chemical Engineering* **88**, 136-143.
- Jones, E. A.** (2011a). The initiation of blood flow and flow induced events in early vascular development. In *Seminars in cell & developmental biology*, pp. 1028-1035: Elsevier.
- Jones, E. A.** (2011b). Mechanical factors in the development of the vascular bed. *Respiratory physiology & neurobiology* **178**, 59-65.
- Kang, H., Duran, C. L., Abbey, C. A., Kaunas, R. R. and Bayless, K. J.** (2015). Fluid shear stress promotes proprotein convertase-dependent activation of MT1-MMP. *Biochemical and biophysical research communications* **460**, 596-602.
- Kang, H., Kwak, H.-I., Kaunas, R. and Bayless, K. J.** (2011). Fluid shear stress and sphingosine 1-phosphate activate calpain to promote membrane type 1 matrix metalloproteinase (MT1-MMP) membrane translocation and endothelial invasion into three-dimensional collagen matrices. *Journal of Biological Chemistry* **286**, 42017-42026.

- Keyt, B. A., Berleau, L. T., Nguyen, H. V., Chen, H., Heinsohn, H., Vandlen, R. and Ferrara, N.** (1996). The carboxyl-terminal domain (111165) of vascular endothelial growth factor is critical for its mitogenic potency. *Journal of Biological Chemistry* **271**, 7788-7795.
- Koefoed, K., Veland, I. R., Pedersen, L. B., Larsen, L. A. and Christensen, S. T.** (2014). Cilia and coordination of signaling networks during heart development. *Organogenesis* **10**, 108-125.
- Koponen, A., Kataja, M. and Timonen, J.** (1996). Tortuous flow in porous media. *Physical Review E* **54**, 406.
- Lamallice, L., Le Boeuf, F. and Huot, J.** (2007). Endothelial cell migration during angiogenesis. *Circulation research* **100**, 782-794.
- Lampugnani, M. G. and Dejana, E.** (2007). Adherens junctions in endothelial cells regulate vessel maintenance and angiogenesis. *Thrombosis research* **120 Suppl 2**, S1-6.
- LaRue, A. C., Mironov, V. A., Argraves, W. S., Czirók, A., Fleming, P. A. and Drake, C. J.** (2003). Patterning of embryonic blood vessels. *Developmental dynamics* **228**, 21-29.
- le Noble, F., Moyon, D., Pardanaud, L., Yuan, L., Djonov, V., Matthijsen, R., Bréant, C., Fleury, V. and Eichmann, A.** (2004). Flow regulates arterial-venous differentiation in the chick embryo yolk sac. *Development* **131**, 361-375.
- Lee, J. Y., Ji, H. S. and Lee, S. J.** (2007). Micro-PIV measurements of blood flow in extraembryonic blood vessels of chicken embryos. *Physiological measurement* **28**, 1149.
- Lee, S., Jilani, S. M., Nikolova, G. V., Carpizo, D. and Iruela-Arispe, M. L.** (2005). Processing of VEGF-A by matrix metalloproteinases regulates bioavailability and vascular patterning in tumors. *The Journal of cell biology* **169**, 681-691.
- Lin, K., Hsu, P.-P., Chen, B. P., Yuan, S., Usami, S., Shyy, J. Y.-J., Li, Y.-S. and Chien, S.** (2000). Molecular mechanism of endothelial growth arrest by laminar shear stress. *Proceedings of the National Academy of Sciences* **97**, 9385-9389.
- Lindken, R., Rossi, M., Große, S. and Westerweel, J.** (2009). Micro-particle image velocimetry (μ PIV): recent developments, applications, and guidelines. *Lab on a Chip* **9**, 2551-2567.
- Liu, A., Nickerson, A., Troyer, A., Yin, X., Cary, R., Thornburg, K., Wang, R. and Rugonyi, S.** (2011). Quantifying blood flow and wall shear stresses in the outflow tract of chick embryonic hearts. *Computers & structures* **89**, 855-867.
- Liu, A., Rugonyi, S., Pentecost, J. O. and Thornburg, K. L.** (2007). Finite element modeling of blood flow-induced mechanical forces in the outflow tract of chick embryonic hearts. *Computers & structures* **85**, 727-738.
- Liu, A., Yin, X., Shi, L., Li, P., Thornburg, K. L., Wang, R. and Rugonyi, S.** (2012). Biomechanics of the chick embryonic heart outflow tract at HH18 using 4D optical coherence tomography imaging and computational modeling. *PLoS One* **7**, e40869.
- Lomholt, J.** (1984). A preliminary study of local oxygen tensions inside bird eggs and gas exchange during early stages of embryonic development. In *Respiration and metabolism of embryonic vertebrates*, pp. 289-298: Springer.
- Lucitti, J. L., Jones, E. A., Huang, C., Chen, J., Fraser, S. E. and Dickinson, M. E.** (2007). Vascular remodeling of the mouse yolk sac requires hemodynamic force. *Development* **134**, 3317-3326.
- Mac Gabhann, F., Ji, J. W. and Popel, A. S.** (2007). VEGF gradients, receptor activation, and sprout guidance in resting and exercising skeletal muscle. *Journal of applied physiology* **102**, 722-734.

- Manbachi, A., Hoi, Y., Wasserman, B. A., Lakatta, E. G. and Steinman, D. A.** (2011). On the shape of the common carotid artery with implications for blood velocity profiles. *Physiol Meas* **32**, 1885-1897.
- Mantha, A., Karmonik, C., Benndorf, G., Strother, C. and Metcalfe, R.** (2006). Hemodynamics in a cerebral artery before and after the formation of an aneurysm. *Am J Neuroradiol* **27**, 1113-1118.
- McCormick, S. M., Eskin, S. G., McIntire, L. V., Teng, C. L., Lu, C.-M., Russell, C. G. and Chittur, K. K.** (2001). DNA microarray reveals changes in gene expression of shear stressed human umbilical vein endothelial cells. *Proceedings of the National Academy of Sciences* **98**, 8955-8960.
- Meinhart, C. D., Wereley, S. T. and Gray, M. H. B.** (2000). Volume illumination for two-dimensional particle image velocimetry. *Meas Sci Technol* **11**, 809-814.
- Metaxa, E., Meng, H., Kaluvala, S. R., Szymanski, M. P., Paluch, R. A. and Kolega, J.** (2008). Nitric oxide-dependent stimulation of endothelial cell proliferation by sustained high flow. *Am J Physiol Heart Circ Physiol* **295**, H736-742.
- Meuer, H.-J. and Baumann, R.** (1988). Oxygen pressure in intra- and extraembryonic blood vessels of early chick embryo. *Respiration physiology* **71**, 331-341.
- Milkiewicz, M., Brown, M. D., Egginton, S. and Hudlicka, O.** (2001). Association between shear stress, angiogenesis, and VEGF in skeletal muscles in vivo. *Microcirculation* **8**, 229-241.
- Murakami, T., Suzuma, K., Takagi, H., Kita, M., Ohashi, H., Watanabe, D., Ojima, T., Kurimoto, M., Kimura, T., Sakamoto, A., et al.** (2006). Time-lapse imaging of vitreoretinal angiogenesis originating from both quiescent and mature vessels in a novel ex vivo system. *Invest Ophthalmol Vis Sci* **47**, 5529-5536.
- Murphy, S., Xu, J., Kochanek, K. and Bastian, B.** (2016). Deaths: Final Data for 2013. *National vital statistics reports: from the Centers for Disease Control and Prevention, National Center for Health Statistics, National Vital Statistics System* **64**, 1-119.
- Nauli, S. M., Kawanabe, Y., Kaminski, J. J., Pearce, W. J., Ingber, D. E. and Zhou, J.** (2008). Endothelial cilia are fluid shear sensors that regulate calcium signaling and nitric oxide production through polycystin-1. *Circulation* **117**, 1161-1171.
- Ng, C. P., Helm, C.-L. E. and Swartz, M. A.** (2004). Interstitial flow differentially stimulates blood and lymphatic endothelial cell morphogenesis in vitro. *Microvascular research* **68**, 258-264.
- Ng, Y. S., Rohan, R., Sunday, M., Demello, D. and D'amore, P.** (2001). Differential expression of VEGF isoforms in mouse during development and in the adult. *Developmental Dynamics* **220**, 112-121.
- Nonaka, S., Tanaka, Y., Okada, Y., Takeda, S., Harada, A., Kanai, Y., Kido, M. and Hirokawa, N.** (1998). Randomization of left-right asymmetry due to loss of nodal cilia generating leftward flow of extraembryonic fluid in mice lacking KIF3B motor protein. *Cell* **95**, 829-837.
- North, T. E., Goessling, W., Peeters, M., Li, P., Ceol, C., Lord, A. M., Weber, G. J., Harris, J., Cutting, C. C. and Huang, P.** (2009). Hematopoietic stem cell development is dependent on blood flow. *Cell* **137**, 736-748.
- Oh, S. P., Seki, T., Goss, K. A., Imamura, T., Yi, Y., Donahoe, P. K., Li, L., Miyazono, K., Ten Dijke, P. and Kim, S.** (2000). Activin receptor-like kinase 1 modulates transforming growth factor- β 1 signaling in the regulation of angiogenesis. *Proceedings of the National Academy of Sciences* **97**, 2626-2631.
- Olsson, A.-K., Dimberg, A., Kreuger, J. and Claesson-Welsh, L.** (2006). VEGF receptor signalling? In control of vascular function. *Nature reviews Molecular cell biology* **7**, 359-371.

- Patterson, C.** (2005). Even Flow Shear Cues Vascular Development. *Arteriosclerosis, thrombosis, and vascular biology* **25**, 1761-1762.
- Paulus, W. J. and Tschöpe, C.** (2013). A novel paradigm for heart failure with preserved ejection fraction: comorbidities drive myocardial dysfunction and remodeling through coronary microvascular endothelial inflammation. *Journal of the American College of Cardiology* **62**, 263-271.
- Penn, J. S.** (2008). *Retinal and choroidal angiogenesis*: Springer Science & Business Media.
- Piiper, J., Tazawa, H., Ar, A. and Rahn, H.** (1980). Analysis of chorioallantoic gas exchange in the chick embryo. *Respiration Physiology* **39**, 273-284.
- Pitts, K. L., Mehri, R., Mavriplis, C. and Fenech, M.** (2012). Micro-particle image velocimetry measurement of blood flow: validation and analysis of data pre-processing and processing methods. *Meas Sci Technol* **23**.
- Podoleanu, A. G., Dobre, G. M., Cucu, R. G. and Rosen, R. B.** (2004). Sequential. optical coherence tomography and confocal imaging. *Opt Lett* **29**, 364-366.
- Poelma, C., Vennemann, P., Lindken, R. and Westerweel, J.** (2008). In vivo blood flow and wall shear stress measurements in the vitelline network. *Experiments in fluids* **45**, 703-713.
- Popel, A. S.** (1988). Theory of oxygen transport to tissue. *Critical reviews in biomedical engineering* **17**, 257-321.
- Pries, A. R., Secomb, T. W., Gahtgens, P. and Gross, J. F.** (1990). Blood flow in microvascular networks. Experiments and simulation. *Circ Res* **67**, 826-834.
- Prior, B. M., Yang, H. and Terjung, R. L.** (2004). What makes vessels grow with exercise training? *Journal of Applied Physiology* **97**, 1119-1128.
- Risau, W. and Lemmon, V.** (1988). Changes in the vascular extracellular matrix during embryonic vasculogenesis and angiogenesis. *Developmental biology* **125**, 441-450.
- Robles, L. Y., Singh, S. and Fisichella, P. M.** (2015). Emerging enhanced imaging technologies of the esophagus: spectroscopy, confocal laser endomicroscopy, and optical coherence tomography. *J Surg Res* **195**, 502-514.
- Rodríguez-Manzanque, J. C., Lane, T. F., Ortega, M. A., Hynes, R. O., Lawler, J. and Iruela-Arispe, M. L.** (2001). Thrombospondin-1 suppresses spontaneous tumor growth and inhibits activation of matrix metalloproteinase-9 and mobilization of vascular endothelial growth factor. *Proceedings of the National Academy of Sciences* **98**, 12485-12490.
- Rouleau, L., Rossi, J. and Leask, R. L.** (2010). The Response of Human Aortic Endothelial Cells in a Stenotic Hemodynamic Environment: Effect of Duration, Magnitude, and Spatial Gradients in Wall Shear Stress. *J Biomech Eng* **132**.
- Ruhrberg, C., Gerhardt, H., Golding, M., Watson, R., Ioannidou, S., Fujisawa, H., Betsholtz, C. and Shima, D. T.** (2002). Spatially restricted patterning cues provided by heparin-binding VEGF-A control blood vessel branching morphogenesis. *Genes & development* **16**, 2684-2698.
- Rutkowski, J. M. and Swartz, M. A.** (2007). A driving force for change: interstitial flow as a morphoregulator. *Trends in cell biology* **17**, 44-50.
- Santiago, J. G., Wereley, S. T., Meinhart, C. D., Beebe, D. and Adrian, R. J.** (1998). A particle image velocimetry system for microfluidics. *Experiments in fluids* **25**, 316-319.
- Sato, M. and Ohashi, T.** (2005). Biorheological views of endothelial cell responses to mechanical stimuli. *Biorheology* **42**, 421-441.
- Schaper, W.** (2009). Collateral circulation. *Basic research in cardiology* **104**, 5-21.

- Schmidt-Nielsen, K.** (1997). *Animal physiology: adaptation and environment*: Cambridge University Press.
- Secomb, T. W., Alberding, J. P., Hsu, R., Dewhirst, M. W. and Pries, A. R.** (2013). Angiogenesis: an adaptive dynamic biological patterning problem. *PLoS Comput Biol* **9**, e1002983.
- Secomb, T. W., Hsu, R., Park, E. Y. and Dewhirst, M. W.** (2004). Green's function methods for analysis of oxygen delivery to tissue by microvascular networks. *Annals of biomedical engineering* **32**, 1519-1529.
- Shah, R. K. and London, A. L.** (2014). *Laminar flow forced convection in ducts: a source book for compact heat exchanger analytical data*: Academic press.
- Sho, E., Komatsu, M., Sho, M., Nanjo, H., Singh, T. M., Xu, C., Masuda, H. and Zarins, C. K.** (2003). High flow drives vascular endothelial cell proliferation during flow-induced arterial remodeling associated with the expression of vascular endothelial growth factor. *Exp Mol Pathol* **75**, 1-11.
- Siefert, S. A. and Sarkar, R.** (2012). Matrix metalloproteinases in vascular physiology and disease. *Vascular* **20**, 210-216.
- Skalak, T. C.** (2005). Angiogenesis and microvascular remodeling: a brief history and future roadmap. *Microcirculation* **12**, 47-58.
- Slough, J., Cooney, L. and Brueckner, M.** (2008). Monocilia in the embryonic mouse heart suggest a direct role for cilia in cardiac morphogenesis. *Developmental Dynamics* **237**, 2304-2314.
- Song, J. W. and Munn, L. L.** (2011). Fluid forces control endothelial sprouting. *Proceedings of the National Academy of Sciences* **108**, 15342-15347.
- Steinman, D. A., Milner, J. S., Norley, C. J., Lownie, S. P. and Holdsworth, D. W.** (2003). Image-based computational simulation of flow dynamics in a giant intracranial aneurysm. *Am J Neuroradiol* **24**, 559-566.
- Swartz, M. A. and Fleury, M. E.** (2007). Interstitial flow and its effects in soft tissues. *Annu. Rev. Biomed. Eng.* **9**, 229-256.
- Tada, S. and Tarbell, J. M.** (2000). Interstitial flow through the internal elastic lamina affects shear stress on arterial smooth muscle cells. *American Journal of Physiology-Heart and Circulatory Physiology* **278**, H1589-H1597.
- Tah, V., Orlans, H. O., Hyer, J., Casswell, E., Din, N., Sri Shanmuganathan, V., Ramskold, L. and Pasu, S.** (2015). Anti-VEGF Therapy and the Retina: An Update. *J Ophthalmol* **2015**, 627674.
- Tang, K., Breen, E. C., Wagner, H., Brutsaert, T. D., Gassmann, M. and Wagner, P. D.** (2004). HIF and VEGF relationships in response to hypoxia and sciatic nerve stimulation in rat gastrocnemius. *Respiratory physiology & neurobiology* **144**, 71-80.
- Tarbell, J. M., Demaio, L. and Zaw, M. M.** (1999). Effect of pressure on hydraulic conductivity of endothelial monolayers: role of endothelial cleft shear stress. *Journal of Applied Physiology* **87**, 261-268.
- Tarbell, J. M. and Pahakis, M.** (2006). Mechanotransduction and the glycocalyx. *Journal of internal medicine* **259**, 339-350.
- ten Dijke, P. and Arthur, H. M.** (2007). Extracellular control of TGF β signalling in vascular development and disease. *Nature reviews Molecular cell biology* **8**, 857-869.
- Thoma, R.** (1893). *Untersuchungen über die Histogenese und Histomechanik des Gefäßsystems*: Enke.

- Tressel, S. L., Huang, R.-P., Tomsen, N. and Jo, H.** (2007). Laminar shear inhibits tubule formation and migration of endothelial cells by an angiopoietin-2-dependent mechanism. *Arteriosclerosis, thrombosis, and vascular biology* **27**, 2150-2156.
- Van der Heiden, K., Groenendijk, B. C., Hierck, B. P., Hogers, B., Koerten, H. K., Mommaas, A. M., Gittenberger-de Groot, A. C. and Poelmann, R. E.** (2006). Monocilia on chicken embryonic endocardium in low shear stress areas. *Developmental dynamics* **235**, 19-28.
- Vempati, P., Mac Gabhann, F. and Popel, A. S.** (2010). Quantifying the proteolytic release of extracellular matrix-sequestered VEGF with a computational model. *PLoS One* **5**, e11860.
- Vempati, P., Popel, A. S. and Mac Gabhann, F.** (2011). Formation of VEGF isoform-specific spatial distributions governing angiogenesis: computational analysis. *BMC systems biology* **5**, 1.
- Vennemann, P., Kiger, K. T., Lindken, R., Groenendijk, B. C., Stekelenburg-de Vos, S., ten Hagen, T. L., Ursem, N. T., Poelmann, R. E., Westerweel, J. and Hierck, B. P.** (2006). In vivo micro particle image velocimetry measurements of blood-plasma in the embryonic avian heart. *Journal of biomechanics* **39**, 1191-1200.
- von Degenfeld, G., Banfi, A., Springer, M. L., Wagner, R. A., Jacobi, J., Ozawa, C. R., Merchant, M. J., Cooke, J. P. and Blau, H. M.** (2006). Microenvironmental VEGF distribution is critical for stable and functional vessel growth in ischemia. *The FASEB journal* **20**, 2657-2659.
- Wakimoto, K., Kobayashi, K., Kuro-o, M., Yao, A., Iwamoto, T., Yanaka, N., Kita, S., Nishida, A., Azuma, S. and Toyoda, Y.** (2000). Targeted disruption of Na⁺/Ca²⁺ exchanger gene leads to cardiomyocyte apoptosis and defects in heartbeat. *Journal of Biological Chemistry* **275**, 36991-36998.
- Wang, Y., Dur, O., Patrick, M. J., Tinney, J. P., Tobita, K., Keller, B. B. and Pekkan, K.** (2009). Aortic arch morphogenesis and flow modeling in the chick embryo. *Annals of biomedical engineering* **37**, 1069-1081.
- Wood, W. and Martin, P.** (2002). Structures in focus—filopodia. *The international journal of biochemistry & cell biology* **34**, 726-730.
- Wu, G., Markowitz, G. S., Li, L., D'Agati, V. D., Factor, S. M., Geng, L., Tibara, S., Tuchman, J., Cai, Y. and Park, J. H.** (2000). Cardiac defects and renal failure in mice with targeted mutations in Pkd2. *Nature genetics* **24**, 75-78.
- Yashiro, K., Shiratori, H. and Hamada, H.** (2007). Haemodynamics determined by a genetic programme govern asymmetric development of the aortic arch. *Nature* **450**, 285-288.
- Yuan, F., Krol, A. and Tong, S.** (2001). Available space and extracellular transport of macromolecules: effects of pore size and connectedness. *Annals of biomedical engineering* **29**, 1150-1158.
- Ziada, A., Hudlicka, O. and Tyler, K. R.** (1989). The Effect of Long-Term Administration of Alpha-1-Blocker Prazosin on Capillary Density in Cardiac and Skeletal-Muscle. *Pflug Arch Eur J Phy* **415**, 355-360.